# Distributed Fiber Ultrasonic Sensor and Pattern Recognition Analytics

by

**Zhaoqiang Peng**

B. E., Shenzhen University, 2011

M. S., University of Texas at Arlington, 2014

Submitted to the Graduate Faculty of

Swanson School of Engineering in partial fulfillment

of the requirements for the degree of

Doctor of Philosophy

University of Pittsburgh

2020

UNIVERSITY OF PITTSBURGH

SWANSON SCHOOL OF ENGINEERING

This dissertation was presented

by

**Zhaoqiang Peng**

It was defended on

July 22, 2020

and approved by

Kevin P. Chen, Ph.D., Professor, Department of Electrical and Computer Engineering

Zhi-Hong Mao, Ph.D., Professor, Department of Electrical and Computer Engineering

Guangyong Li, Ph.D., Associate Professor, Department of Electrical and Computer Engineering

Feng Xiong, Ph.D., Assistant Professor, Department of Electrical and Computer Engineering

Paul Ohodnicki, Ph.D., Associate Professor, Department of Mechanical Engineering & Materials Science

Dissertation Director: Kevin P. Chen, Ph.D., Professor, Department of Electrical and Computer Engineering

**Distributed Fiber Ultrasonic Sensor and Pattern Recognition Analytics**

Zhaoqiang Peng, Ph.D.

University of Pittsburgh, 2020

Ultrasound interrogation and structural health monitoring technologies have found a wide array of applications in the health care, aerospace, automobile, and energy sectors. To achieve high spatial resolution, large array electrical transducers have been used in these applications to harness sufficient data for both monitoring and diagnoses. Electronic-based sensors have been the standard technology for ultrasonic detection, which are often expensive and cumbersome for use in large scale deployments.

Fiber optical sensors have advantageous characteristics of smaller cross-sectional area, humidity-resistance, immunity to electromagnetic interference, as well as compatibility with telemetry and telecommunications applications, which make them attractive alternatives for use as ultrasonic sensors. A unique trait of fiber sensors is its ability to perform distributed acoustic measurements to achieve high spatial resolution detection using a single fiber. Using ultrafast laser direct-writing techniques, nano-reflectors can be induced inside fiber cores to drastically improve the signal-to-noise ratio of distributed fiber sensors. This dissertation explores the applications of laser-fabricated nano-reflectors in optical fiber cores for both multi-point intrinsic Fabry–Perot (FP) interferometer sensors and a distributed phase-sensitive optical time-domain reflectometry (φ-OTDR) to be used in ultrasound detection.

Multi-point intrinsic FP interferometer was based on swept-frequency interferometry with optoelectronic phase-locked loop that interrogated cascaded FP cavities to obtain ultrasound patterns. The ultrasound was demodulated through reassigned short time Fourier transform

incorporating with maximum-energy ridges tracking. With tens of centimeters cavity length, this approach achieved 20kHz ultrasound detection that was finesse-insensitive, noise-free, high-sensitivity and multiplex-scalability.

The use of φ-OTDR with enhanced Rayleigh backscattering compensated the deficiencies of low inherent signal-to-noise ratio (SNR). The dynamic strain between two adjacent nano-reflectors was extracted by using 3×3 coupler demodulation within Michelson interferometer. With an improvement of over 35 dB SNR, this was adequate for the recognition of the subtle differences in signals, such as footstep of human locomotion and abnormal acoustic echoes from pipeline corrosion. With the help of artificial intelligence in pattern recognition, high accuracy of events' identification can be achieved in perimeter security and structural health monitoring, with further potential that can be harnessed using unsurprised learning.

## Table of Contents

## List of Tables

## List of Figures

## Acknowledgment

The charm of optical and electrical system is the constant impetus for my painstaking efforts to undertake this PhD. It has truly been a life-changing experience and granted me maturity in my dialectical thinking. Without the support and guidance from many people, it would have been impossible to go through the long journey of pure research. I sincerely appreciate this five-year odyssey accompanied by invaluable help, insightful instruction and even contradictory opinions.

The most important person I would like to say a very big thank you is my advisor, Prof. Kevin P. Chen. His encouragement and generous support drove me to grow as a research scientist. As a tremendous mentor, he has extraordinary power to put himself in the students' shoes. Working under his guidance has been a truly comfortable and enriching experience.

I also would like to thank my committee member, Prof. Guangyong Li, Prof. Zhi-Hong Mao, Prof. Feng Xiong, and Prof. Paul Ohodnicki. Thank you for serving as my committee members even with the hardship of the Covid-19 pandemic. Although the surge of coronavirus cases during this special moment tortures everyone, your brilliant comments and suggestions made my defense be an enjoyable moment.

I have shared this fantastic journey with many colleagues and peers. We attended various meetings together, devoted to learning, discussed research plans and enjoyed the academic life. We gushed over the enthusiasm of our studies and we were genuinely excited to share ideas with each other. I am so glad to have had this precious opportunity to work with so many wonderful people in my life. Thank you for the altruistic support and dear friendships - Dr. Rongzhang Chen, Dr. Sheng Huang, Dr. Aidong Yan, Dr. Shuo Li, Dr. Ran Zou, Dr. Mohamed Bayoumy, Dr.

Rongtao Cao, Dr. Hangjun Ding, Dr. Guanquan Liang, Ms. Yawen Huang, Ms. Mohan Wang, Ms. Jingyu Wu, Ms. Xinruo Yi, Mr. Qirui Wang, Mr. Yuqi Li, Mr. Yang Yang, Mr. Kehao Zhao, Mr. Zekun Wu, Mr. Shenghan Gao and Ms. Jieru Zhao; visiting scholars of Prof. Hongqiao Wen, Prof. Hu Liu, Prof. Hui Lan, and Prof. Hao Zhang; collaboration consultants of Dr. Ping Lu and Dr. Mudabbir Badar; and many others. I hope you and your family are healthy and safe during these uncertain and unprecedented times.

Speechless gratitude is reserved for my family. The route to the end of this journey does not only belong to me. Holding hands with you to walk through it has brought perseverance and tenacity to our relationship. Following with two little angles fall from the sky, enormous happiness fills our family. With all my might, I would never let any harm come your way. A wonderful world is waiting nearby.

# 1.0 Introduction

In the last 60 years, the commercialization of ultrasound sensors has opened up a large market of physical, chemical and biochemical sensing. As a result, numerous technologies have been proposed to assess ultrasonic waves based on various acoustical effects. Till date, nothing can substitute for their versatility and wide-spread use in industrial and medical applications.

## 1.1 Background and Motivation

Acoustic waves arise from an initial pressure perturbation that impacts atoms in a state of equilibrium and forces them to movements of compression and rarefaction. The longitudinal movement of atoms as they pass kinetic energy outward from the source was described as a type of mechanical wave. In 1969, Feynman derived the sound equation for this mechanical wave from the velocity of particles and acoustic pressure over time [1]. This was the first time the properties of travelling acoustic waves were fully studied, which showed a detailed wave solution as intensity and phase. The time-dependent variation of intensity and phase are determined by initial releasing status of the acoustic source and characteristics of the propagation path. Lots of acoustic sensors were developed to measure the physical, chemical, or biological quantities that resulted in changes of the propagation path or location of initial release. Most of these sensors were laid in the ultrasonic region, for example, the flexural plate-wave sensor, thickness shear-mode sensor, medical ultrasound and surface acoustic-wave sensor [2].

The frequency of ultrasound that exceeds the upper limit of human hearing is over 20 kHz. Deploying high-frequency acoustic waves in an interrogation system has prime importance in three perspectives: diffraction, sensitivity, and scattering. Diffraction describes the divergent pattern of beam spread which corresponds to the configuration of source and acoustic wavelength. High-frequency acoustic wave as submillimeter wavelength generates parallel-sided beam resulting a sharp focus at focal plane. Small focal point reveals fine image detail in medical ultrasonic imaging [3]. Sensitivity is used to depicted the accuracy in characterization of thin-film materials, liquid properties or polymers in chemical and biochemical acoustic sensing. The intrinsic resonance frequency of a transducer determines the sensitivity and detection of the measurement. Superb sensitivity requires adequate resonance frequency which usually is in tantamount to high operational frequency of sensor [4]. Higher operational frequency such as ultrasound detection improves the sensitivity in certain interrogation systems. The last beneficial trait of ultrasound is enhanced intensity of scattering. Scattering of acoustic wave occurs only when the irregularities in the propagation path are much smaller than the acoustic wavelength. The omnidirectional scatterings from small scatters include backward portions known as acoustic echoes. An equation was derived to describe the strength of backscattering as a spherical wave without considering the boundaries of the medium [5].

$$A_{bs} = -A_i \frac{10\pi^2 f^2 a^2}{3c^2 R}, \tag{1-1}$$

$A_i$ is the amplitude of incident ultrasound pressure; $f$ is the central frequency of acoustic wave; $a$ is the diameter of scatter and $R$ is the distance between scatter and transducer. The amplitude of the backscattered echo is proportional to the acoustic frequency squared. High-frequency acoustic interrogation reinforces the strength of backscattering in echography.

Passive reception of the ultrasound attracts a lot of attention other than implementing ultrasound in the interrogation system. Light-induced thermoelastic expansion of biological tissues elicits the sudden release of large energy within a solid as acoustic emissions that generates an ultrasonic wave at broad frequency range. A reliable ultrasound receiver is desired to perform accurate detection of especially weak and subtle signals. As such, the high-sensitivity of ultrasound detection is crucial in the demand of converting the weak broadband ultrasound into analog signals.

There have not been significant strides made on ultrasonic receivers in the last decade. The generic structures of ultrasonic sensors are classified into two distinct families: bulk piezoelectrical transducer and diaphragm-based micro-machined transducer. Figure 1 illustrates the simplified schematic of a piezoelectric transducer and a capacitive micro-machined ultrasound transducer (CMUT) [6].

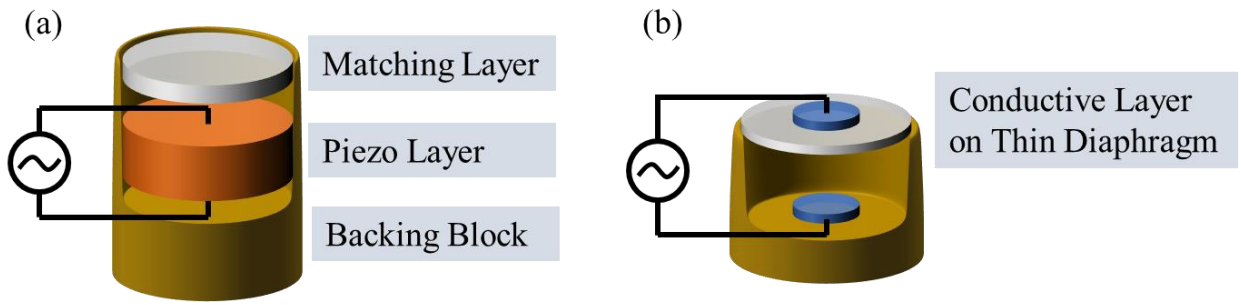


**Figure 1 The typical structures of ultrasonic sensors: (a) piezoelectric ultrasound transducer; (b) capacitive micro-machined ultrasound transducer.**

As an ultrasonic receiver, a piezoelectrical transducer converts mechanical force into electricity based on the destruction of the hexagonal symmetry in piezoelectric material crystals. The local deformation caused by mechanical pressure polarizes the molecules and aligns them into a dipolar state. Lead zirconate titanate (PZT) is the most common material used in single element

piezoelectrical transducers. Large efforts have been taken to improve the electromechanical coupling coefficients by optimizing the piezocomposite chemistry [7]. The recent progress of research studies on piezoelectric element shows low acoustic impedance and inherently wideband in high-frequency acoustic wave detection [8]. However, the tradeoff between operational frequency and signal-to-noise ratio (SNR) deteriorate the effectiveness of ultrasound detection. Adequate operational frequency in ultrasonic application requires high fundamental resonance frequency of transducer. An equation presenting the resonance frequency of PZT circular plate can be described as,

$$f_R = \frac{1}{2}\frac{t}{a^2}\sqrt{\frac{E_{PZT}}{\rho_{PZT}}}, \tag{1-2}$$

where $t$, $a$, $E_{PZT}$ and $\rho_{PZT}$ are thickness, radius, Young's modulus and material density of piezoelectrical layer respectively [9]. An increase in fundamental resonance frequency is followed by shrinking the diameter of active area in transducer. Usually, the dimension of PZT need to be comparable to the wavelength of ultrasound (~mm diameter for ~MHz ultrasound), whereas introducing the issue of low SNR. Less dipolar molecules in piezoelectric elements from small dimensions of the transducer degrades the signal strength at output. It is the most concerned drawback of piezoelectrical transducer in ultrasound detection.

CMUT is a relatively new concept that has also drawn lots of attention in recent research studies. It takes advantage of nanoscale lithography in nanofabrication and builds the transducer on microscale diaphragm [10]. The vibratory membrane affected by external mechanical forces induces capacitance change between electrodes. With high compatibility to nanofabrication in silicon wafer, CMUTs can be placed as large arrays that attach separated signal processing units

that construct large microscale electro-mechanical systems [11]. The performance of CMUT has been proven to be comparable to bulk piezoelectrical transducers in the manner of coupling coefficients and bandwidths [12]. However, the strict temperature control and complex fabrication of suspended membranes further curbs its potential in practical applications. Furthermore, high electrical impedance of capacitive structures corresponding to high operational voltages affect the reliability of devices [13].

As typical metal electrical sensors, both piezoelectrical transducer and CMUT suffer from the salient susceptibility to moisture penetration and wear-and-tear from weather [14]. The reliability of electrical component in harsh environment is persistently unreliable. Moreover, emerging research studies of photoacoustic tomography (PAT), nondestructive testing (NDT) and seismic physical surveys which examine the original releasing status of ultrasounds achieve large-scale field monitoring using ultrasound transducers as large array. Microscale CMUTs bear significant crosstalk in the transducer arrays as electromagnetic interference (EMI), while PZTs have burdensome and complex data acquisition [15]. The challenge of reliable ultrasound sensing with robustness on multiplex scalability remain to be solved.

## 1.2 Multiplex Ultrasound Fiber Sensor

In the 1960's, the latent demand of optical fiber for telecommunications heralded the invention of lasers. Researchers sought an ideal medium that had low attenuation and could be used for the transmission of data over long distances. Kao and Hockham first demonstrated a low loss optical fiber in 1965 making which made a far-reaching influence on fiber optics [16]. At about the same time as the advent of optical fiber-based data communications, the merits of optical

fiber sensors were discovered after the first Fotonic sensor [17]. Because of features such as immunity to electromagnetic interference, dielectric material, small cross-section, lightweight, multiplex scalability, telemetry and telecommunication compatibility, optical fiber sensors are an excellent candidate of the measurement of various environmental parameters. Up to now, it has been successfully used to detect temperature, strain, vibration, position, current, pressure and so on [18-23].

The incomparable merits of optical fibers have great appeal to the research of novel ultrasonic receivers, rather than conventional metal electrical sensors. The small cross-sectional area of optical fiber possesses the high sensitivity to the ultrasound detection. And dielectric properties of silica make optical fiber become suitable for the dynamic strain measurement in harsh environment. In addition to the advantageous dimension and material, the easy fabrication process conduces to the promise of mass production. Some of the ultrasound fiber sensors have shown the potential to address limitations of piezoelectric and capacitive technologies [24].

### 1.2.1 Single-point Ultrasound Sensors

Till date, most of available ultrasound fiber sensors could only perform single-point detection which made significant scalability of optical fiber less feasible. The very first loss-based dynamic strain fiber sensor was demonstrated in 1977, and was used to measure vibration-dependent bending loss [25]. The assessment of coupling loss were also observed in fused tapered fibers [26] and lateral misalignments [27]. Those sensors implement a simple structure for single-point detection that is dependent on loss-based interrogation, which simply detects optical intensity changes within optical fiber. But they suffered from the inherent noise including laser instability and environmental perturbation.

In the same year, 1977, the first interferometric acoustic sensor was proposed based on the Mach–Zehnder interferometer (MZI) [28]. After that, a succession of various interferometric methods were introduced for ultrasonic detection including Michelson, Sagnac and Fabry–Perot interferometer (FPI) [29-31]. The strain-induced change in the mean free path or the optical phase within the interferometer triggered the shift of interference pattern. The resulting frequency or intensity changes at interference pattern expose the information of dynamic strain. Another approach that implements a similar strategy made use of optical resonators such as fiber Bragg gratings (FBGs) [32]. Perturbations occurring at a resonator caused frequency or intensity changes in the reflectance curve. Figure 2 shows the schematics of various interferometers and resonators. A PZT piezoelectric transducer was hypothesized to be a vibration source that generates ultrasound.

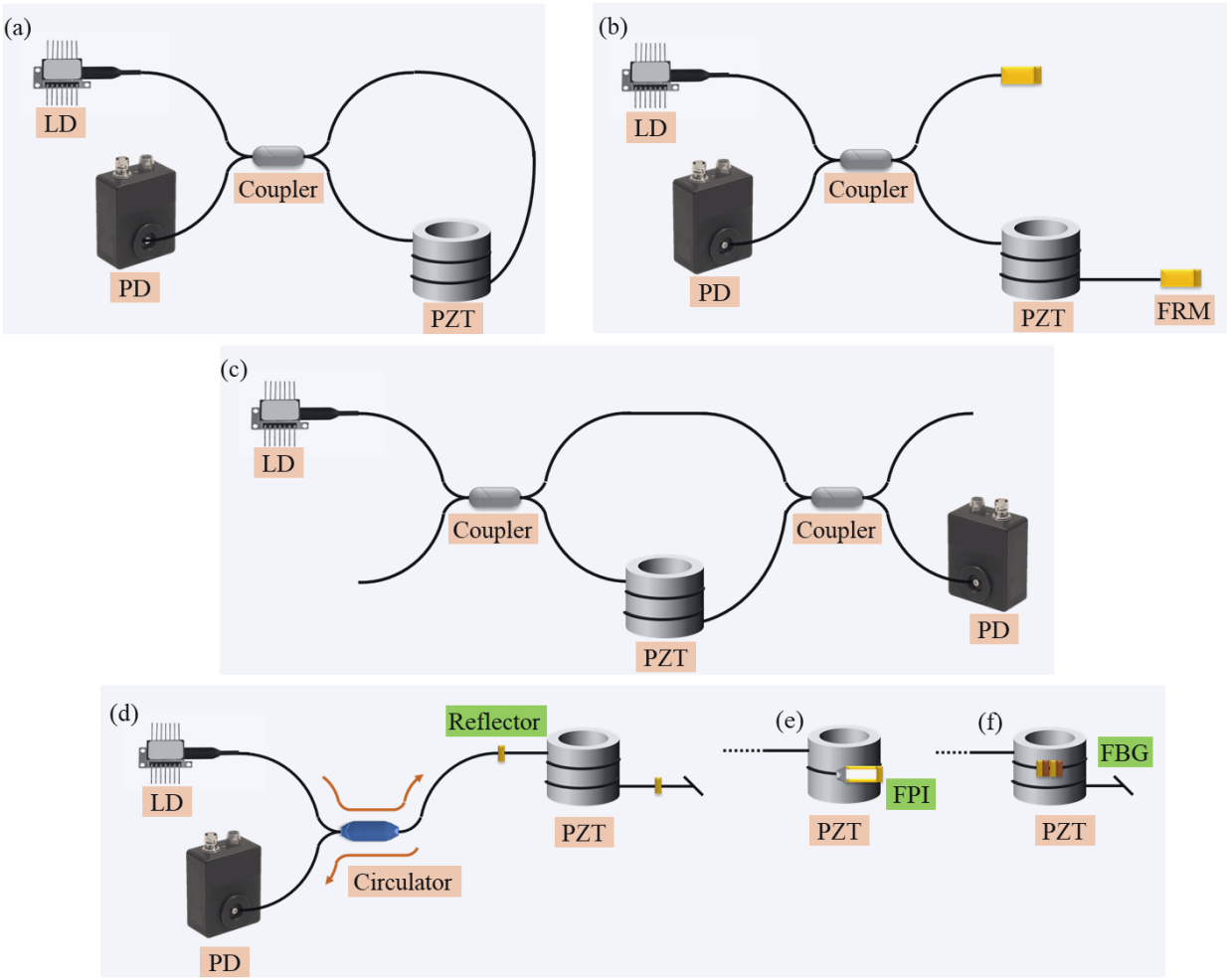


**Figure 2 Schematic of interferometers and resonators: (a) Sagnac, (b) Michelson, (c) Mach–Zehnder, (d) intrinsic Fabry–Perot, (e) extrinsic Fabry–Perot and (f) fiber Bragg grating. (LD: laser diode; PD: photodetector; PZT: lead zirconate titanate piezoelectric transducer.)**

Nearly all interferometers were based on quadrature point demodulation which maintains the wavelength of interrogating lasers in the slope of single interference fringe. Optical resonators employed similar demodulation that tuned interrogating wavelengths to the monotonic region of reflectance curve. It brought a similar linear intensity response for high-speed strain measurement. Figure 3 shows the quadrature point in the interference pattern as well as the curve center of optical resonator's reflectance slope. Although they still based on intensity-based demodulation, the

interferometers and optical resonators granted insight into sensing refractive index change instead of focusing on loss from light decoupling.

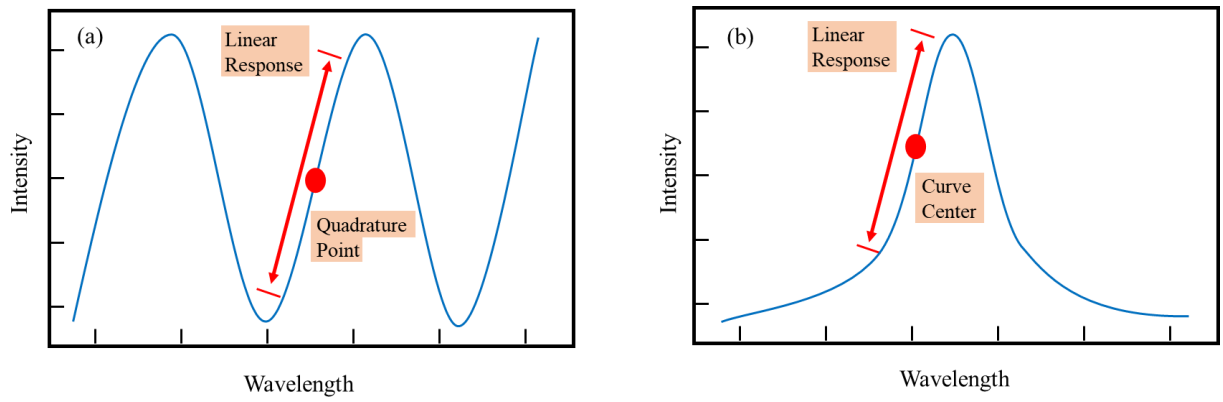


**Figure 3 Generic illustration of quadrature point demodulation for (a) interferometers and (b) optical resonators in like manner.**

### 1.2.2 Multi-points Ultrasound Sensors

In refractometry, strain-induced refractive index change affects the resonance frequency of resonators or the mean free path and phase of interrogating light in one arm of interferometer. It becomes much more sensitive to external mechanical force with superb SNR rather than decoupling loss. Some researchers have applied this simple intensity-based refractometry to multi-points dynamic strain measurement to enable multiplexing, such as MZIs [33] and FBGs [34-36]. Figure 4 shows the typical schematic of multi-points strain sensing including MZIs and FBGs. A PZT piezoelectric transducer was still used to mimic ultrasound generation.

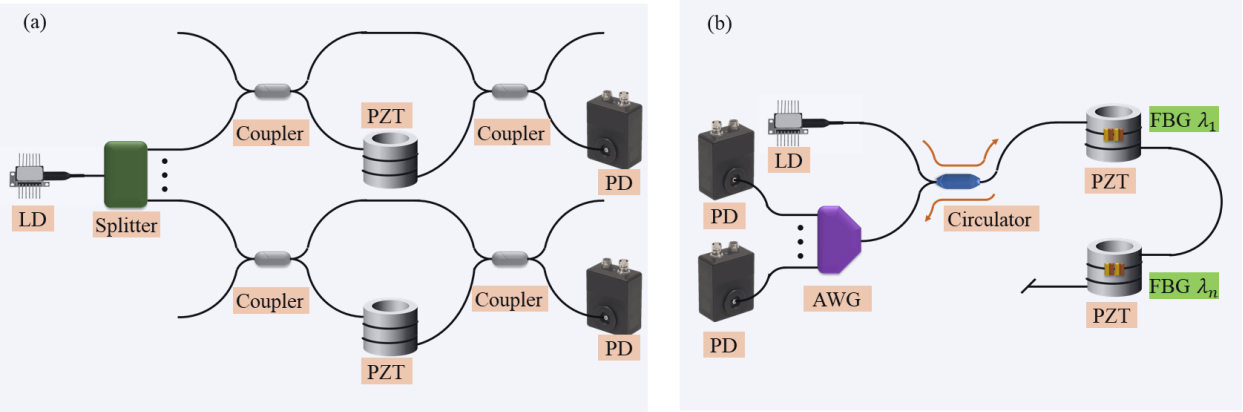


**Figure 4 Schematics of multi-points strain sensing (a) MZIs and (b) FBGs. (AWG: arrayed waveguide grating)**

Nevertheless, the use of massive couplers, splitters, and photodetectors in MZIs introduces additional losses and disproportionate burdens on data acquisition. And in some research studies, the use of optical switches in FBGs sacrifices the speed of interrogation. Besides, the control of inherent noise remains to be investigated.

Interferometers and resonators bear the inherent noise from lasers and optical fibers respectively. Several methods have been proposed to mitigate laser noise such as Pound-Drever-Hall, and used in frequency locking and phase-based quadrature demodulation as multiple-wavelength interrogation [37, 38]. The accuracies of strain measurement were greatly improved but in absence of considering the effects of relative intensity noise (RIN) for interrogating laser and polarization state drift of standard telecom fibers. RIN arises from relaxation oscillations in solid-state lasers or intrinsic phase and frequency fluctuations in distributed feedback lasers (DFB). It is a type of high-frequency noise that may affect the SNR in the ultrasound detection [39]. Another factor should be paid close attention is optical fiber selection in intensity-based refractometric methods. Even the minor mechanical perturbations along the fiber cable can cause certain intensity fluctuations of interrogating light with the consequence of polarization state drift.

It becomes much severer in some optical fibers with high numerical aperture such as introducing additional bending loss.

On the other hand, white light interferometry (WLI) offers an intensity-independent solution for reliable dynamic sensing. Estimating the accurate oscillation frequency of interference pattern can be used to extract the detailed optical path difference (OPD) within the interferometer. The assessment of OPD is directly oriented from spectrum analysis instead of intensity acquisition which avoids RIN and other intensity-based noise. Recently, multi-point strain measurements with WLI were investigated and reported in the use of several intrinsic FPIs with different cavity lengths [40, 41]. The miniaturized intrinsic FPIs are extremely suitable for extensive deployment compared to other interferometers. The amount of sensing points can be numerous because of the infinite choices present on cavity length design of separated intrinsic FPIs. However, due to the requirement of full spectrum acquisition, the limited speed of the spectrometer restricted the performance of WLI for ultrasound detection. The frame rate of charge-coupled device (CCD) in spectrometer is capped to several kHz which is far from enough for high-frequency strain measurements.

### 1.2.3 Distributed Ultrasound Sensors

The employment of interferometers and resonators in constructing a large sensing array for ultrasound detection often involves either the burden of data acquisition or the restriction of speed during the whole-spectrum scan. These are not the only solutions to decoding the dynamic strain from frequency and intensity of interrogating light. Optical reflectometry is another method broadly recognized to perform large-scale distributed strain sensing while revealing information on spatial location [23]. By exploiting the intrinsic scattering property of optical fibers, it scans

the strain-induced refractive index changes along the entire fiber with spatial continuity. These various mechanisms result in the forms of Rayleigh, Brillouin or Raman scattering. Figure 5 shows the spectral features of intrinsic scattering mechanisms from interrogating light $f_0$ within optical fiber. Those fundamental scatterings determine the differences in various systems on measurands, spatial resolutions, sensitivities, and sensing ranges. furthermore, they have been successfully applied in several well-known sensing systems including: Raman distributed temperature sensing, Brillouin distributed temperature and strain sensing and Rayleigh distributed acoustic sensing (DAS). These sensing systems also cover a wide range of applications on safety, security and structural health monitoring.

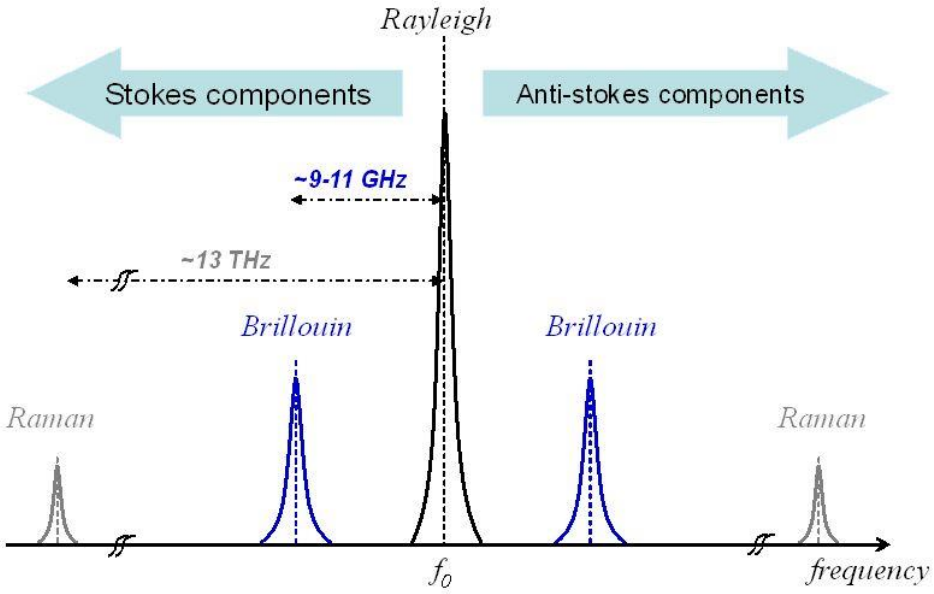


**Figure 5 The spectrum of three fundamental scatterings [42].**

Distributed dynamic strain measurement has drawn a lot of attention and has become a great challenge due to the requirement of fast response and high SNR. Several investigations of

Brillouin optical time domain reflectometry (B-OTDR) has been examined since it has superb SNR from nonlinear amplification [43]. But taking minutes to scan the Brillouin spectrum limits the maximum detectable frequency. Instead, Rayleigh scattering keeps the same frequency as interrogating light which avoids gain in the spectrum scan. This greatly expedites the speed of interrogation and features a fast response in dynamic strain measurement.

Previously, time-domain and frequency-domain Rayleigh reflectometry were introduced for distributed strain measurement [44, 45]. However, optical frequency-domain reflectometry (OFDR) was blocked from ultrasound detection due to the limitation of the interrogating source [46]. In each repetitive scan, it is hard to meet all the criteria such as high-speed sweeping velocity, broadband scan range and identical frequency. Conventional direct-detection in OTDR is also inapplicable for dynamic strain measurement since the dependence of Rayleigh scattering intensity on strain is too weak [47].

Phase-sensitive Rayleigh optical time domain reflectometry (φ-OTDR) offers interesting an solution for distributed ultrasound detection. It has become a core technology dependent on real-time dynamic event monitoring. φ-OTDR was first proposed as distributed intrusion sensor in 1993 following the concern of low SNR [48]. The performance of φ-OTDR system, such as sensing dynamic range, spatial resolution, and sensitivity, are strongly restricted by the SNR of system. Moreover, when the sensing length extends to hundreds of kilometers with high spatial resolution, the SNR becomes one of most crucial problems.

### 1.2.4 SNR Improvement and Pattern Recognition

In φ-OTDR system, continuous-wave (CW) light from the narrow linewidth laser is modulated to optical pulses and sent into the sensing fiber. Due to the inherently weak Rayleigh

backscattering signal from telecom-grade fibers, the φ-OTDR based on unmodified optical fibers often incurs poor SNR. The SNR of backscattered signals are proportional to the extinction ratio (ER) of both the laser pulse and intrinsic Rayleigh scattering coefficient of optical fiber. Either increasing the ER or enhancing Rayleigh coefficient helps to ameliorate SNR. The simplest method to improve ER is via a modulator cascade. The pulsed interrogating light is effectively further suppressed in cascaded modulators stemming from nonlinear Kerr effect [49]. On the other hand, several methods have been proposed to enhance Rayleigh scattering in fiber, such as ultraviolet (UV) exposure of the hydrogen-loaded single mode fiber [50, 51] and UV inscription of ultra-weak FBGs [52, 53]. However, the complexity of the fabrication procedure hampers its practical application. And they are not stable at elevated temperatures [54].

Various signal processing algorithms like moving average and wavelet transform have been demonstrated to improve SNR as well [55, 56]. Some novel two-dimensional edge detection [57] and bilateral filtering [58] methods have also reported. Relying on signal processing to improve SNR can be robust and cost-effective but still has the challenge of long processing time especially for huge amount of data.

Even if SNR of φ-OTDR system is enhanced to an adequate level, another well-known issue that limits the system in DAS applications is false alarms from ambient environmental disturbances. Perimeter security and structural health monitoring require systems to perform accurate judgments on threat identification apart from benign perturbations. Multi-scale wavelet decomposition [59], Gaussian mixture models (GMMs) [60, 61], and Morphologic feature extraction methods [62] have been used to classify specific events including pattern recognition (PR). Most of prior works focused on single-hidden-layer machine learnings approaches which are incapable of processing huge amount of data in real-time while distinguishing false alarms from

similar phase shift [60]. And since all of them are based on amplitude-measuring schemes, a low SNR system cannot be neglected that inordinately degrades the effectiveness of PR. The φ-OTDR in DAS system has only been applied to distinguish events with significantly different acoustic patterns such as human walking and motor vehicle movement, or classification of safe excavator operation, local traffic, and accidental excavator contact with a gas pipeline [63].

## 1.3 Thesis Contribution

Multi-points ultrasound fiber sensors or distributed ultrasound sensors appear to be a tool with great potential in PAT, NDT, perimeter security and seismic physical surveys. Current constraints in refractometry and reflectometry push the large-scale dynamic strain measurement into a bottleneck. WLI as an intensity-independent interrogation tool features multiplex scalability and wonderful reliability but stops at low-speed sampling. φ-OTDR owning fantastic interrogation range and broad detectable frequency was impeded by low SNR from intrinsic Rayleigh coefficient and unreliable PR. The goal of this thesis, is to circumvent the current barriers of refractometry and reflectometry and develop reliable and effective multi-point ultrasound fiber sensors and distributed ultrasound sensors. Furthermore, rather than depend on single-hidden-layer PR that requires filtration of demand information, the event recognition can be kept at a high-level of promising accuracy by using efficient artificial intelligence for PR.

The foundation of innovative system design was based on artificial Rayleigh scatters in telecom fibers inscribed by femtosecond laser direct writing. The nanostructures used as nano-reflectors inside fiber cores can drastically improve the intensity of Rayleigh backscattering to over 35 dB. They can be used to construct intrinsic FPI as reflectors or enhance the SNR of φ-

OTDR. Applications of laser-fabricated nanostructures were explored for ultrasound detection in both multi-points intrinsic FPI and distributed φ-OTDR.

Scanning white light interferometry with optoelectronic phase-locked loop (OPLL) was used in multi-point intrinsic FPI that interrogated cascaded FP cavities with the goal of obtaining temporal fringe patterns. The vibration-induced frequency shift can be extracted by tracking the maximum-energy ridges in time-frequency spectrogram after using reassigned short-time Fourier transform (STFT). It has potential to become the standard for real-time spectral analysis since field programmable gate arrays (FPGA) with embedding STFT has been reported [64]. 20 cm long intrinsic FP cavity within the polarization-maintaining (PM) fiber core was demonstrated for 20 kHz detection. And two intrinsic FPIs with different cavity length was cascaded into a single PM fiber that proved to be feasible on multi-points ultrasound sensing. This approach has shown the traits of finesse-insensitive, noise-free, high-sensitivity and multiplex scalability.

Another application of artificial scatters was to enhance Rayleigh backscattering profiles in the φ-OTDR system. The vibration-induced phase shift between adjacent scatters was tactfully designed to be extracted by using 3×3 coupler demodulation within unbalanced Michelson interferometers (MI). The enhanced SNR provided detailed delineation of distributed ultrasound signals that could be applied to recognize the subtle information in acoustic events. Distinguishing the locomotion difference between individuals and abnormal acoustic echoes from pipeline corrosions were assessed by using machine learning data analytics. Deep neural networks that use multiple hidden layers was implemented to address complex nonlinearity. Supervised neural networks provides a high degree of accuracy on event identification in both cases. Furthermore, unsupervised neural networks were investigated for the label-free potential.

## 2.0 Fiber Principle

Fiber sensors employ the unique properties of optical fiber to perceive the ambient environmental perturbation. External stress elicits strain inside fiber cores which results in geometric deformation and refractive index change of optical fiber. Shape deformation was utilized in loss-based interrogation for the measurement of decoupling ratio. The limited SNR limited its applicability for the detection of weak strains like micro-bending. Instead, monitoring the refractive index change was reliable and dependable for measurement of subtle strains that occurred at the fiber core.

### 2.1 Photo-elastic Response of Optical Fiber

Optical fibers as fused silica in the form of quartz is optical isotropic when there is an absence of stress. When mechanical deformation imposes on an optical fiber, the strain-dependent dielectric constant is governed by the photo-elastic effect. It highlights the occurrence of optical anisotropy as the presence of double refraction, birefringence, or dichroism. The relationship between the mechanical stress and refractive index was described by the photo-elastic effect that determined the phase shift of transmitting light at different polarization states.

For a linear elastic material, the refractive index is linearly proportional to the loads, which was first demonstrated by Maxwell. The principle stress $\sigma$ in the direction of x, y and z induce the variation of refractive index that can be expressed as:

$$n_x = n_0 + \left[C_1\sigma_x + C_2(\sigma_y + \sigma_z)\right],$$
$$n_y = n_0 + \left[C_1\sigma_y + C_2(\sigma_x + \sigma_z)\right], \quad (2\text{-}1)$$
$$n_z = n_0 + \left[C_1\sigma_z + C_2(\sigma_x + \sigma_y)\right],$$

where $n_0$ is unstressed refractive index, $C_1$and $C_2$ are direct and transverse opto-elastic constant respectively [65]. The linear relation between the refractive index and stress manifests a feasible way to measure the complete state of external stress on optical fibers. Refractometry and reflectometry are totally dependent on phase detection which corresponds to reliable strain measurements. Figure 6 shows the schematic of an external stress impacting optical fiber. Optical fiber as a homogeneous dielectric rod has an almost identical value to Young's modulus and Poisson's ratio in its core and cladding. Hence, the external stress can be approximated as two-dimensional plane-stress, where $\sigma_z = 0$. The two-dimensional plane-stress matching two orthogonal polarization modes of optical fiber brings the accumulation of relative phase retardation along each direction.

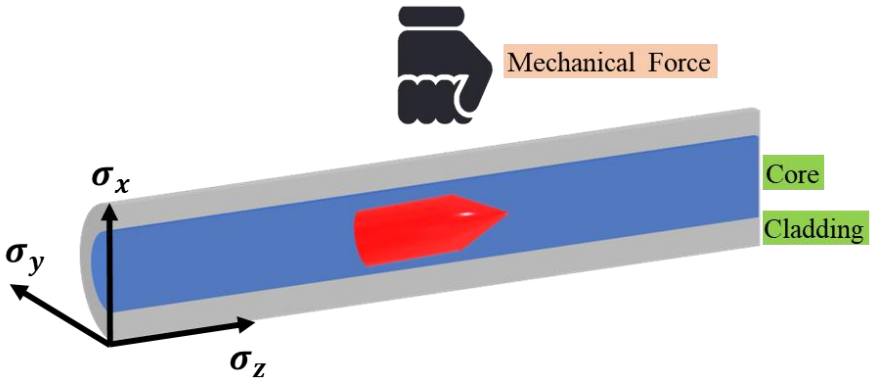


**Figure 6 Schematic of an optical fiber applied with external stress.**

Considering a section of optical fiber with effective length $l_{eff}$, the relative phase retardation at two orthogonal polarization modes of single mode fiber can be written as:

$$\begin{aligned} \Delta\varphi_x &= k_0 \Delta n_x l_{eff} = k_0 l_{eff} \left(C_1 - \frac{C_2}{3}\right) \sigma_x, \\ \Delta\varphi_y &= k_0 \Delta n_y l_{eff} = k_0 l_{eff} \left(C_2 - \frac{C_1}{3}\right) \sigma_y, \end{aligned} \tag{2-2}$$

where $k_0$ is the unstressed wavenumber and $\Delta n$ is stress-induced refractive index change [66]. Relative phase retardation at two orthogonal polarization modes have separated the response into the transverse principle stress.

In practical applications, optical fibers were embedded into host material performing strain measurements. Several types of host materials have been reported including plastic, graphite composite materials, concrete and alloy metal [67-69]. Due to a great diversity of host material with different mechanical properties and complex shapes of mold, the theoretical analysis of stress transfer was curbed by a lack of an appropriate model. For example, the frequency response of acoustic wave propagating in steel elbow and epoxy strip is hard to reconcile with a unified theory. Various validated models were reported corresponding to simple structures in a wide range of host materials. However, some of them ignored the impact of a soft coating on the outside an optical fiber, like silicone or polypropylene. The effect of a soft coating on stress transfer can be simulated by building a unified model. Figure 7 shows an optical fiber with soft coating that was embedded into a host material. The response of optical fiber to external stress depends on the mechanical interactions between optical fiber, soft coating and host material.

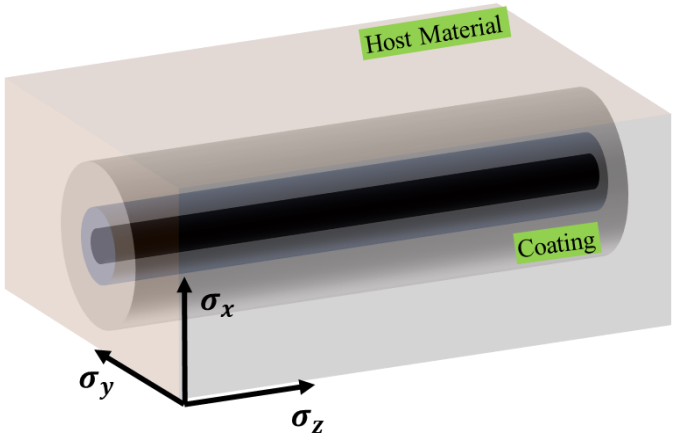


**Figure 7 Schematic of an optical fiber applied with external stress.**

Soft coating was expected to dampen the external stress response in an optical fiber as a consequence of small Young's modulus. The displacement $\xi$ in the x-axis of optical fiber follows the motion equation consisting of Young's modulus $E_c$ and damping coefficient $D_c$ of fiber coating [66],

$$\rho\frac{\partial^2\xi}{\partial t^2}+2D_c\frac{\partial\xi}{\partial t}+2E_c\xi=2A\sqrt{E_c^2+(\omega_a D_c)^2}\cos\left(\omega_a t-kx-tan^{-1}\left(\frac{\omega_a D_c}{E_c}\right)\right), \quad (2\text{-}3)$$

where $\rho$ is mass density, $A$ and $\omega_a$ are amplitude and angular frequency of external stress, respectively. After considering the initial set of conditions, the solution of the displacement equation depicts the frequency response of strain at the optical fiber. The inertial effect prevents the optical fiber from directly sensing the external vibrations.

## 2.2 Intrinsic Fabry–Perot Interferometer

Interferometry is the one of most common methods used to detect dynamic strain affecting optical fibers. IFPIs, which exhibit excellent multiplex scalability, are well-known for multi-point sensing. With two partial reflectors embedded in the fiber core, the interrogating light never escapes from the optical fiber. The typical structure of IFPI was shown in Figure 8. Two partial reflectors with reflectance $R_1$ and $R_2$, and transmittance $T_1$ and $T_2$, delineate the light propagation inside IFPI.

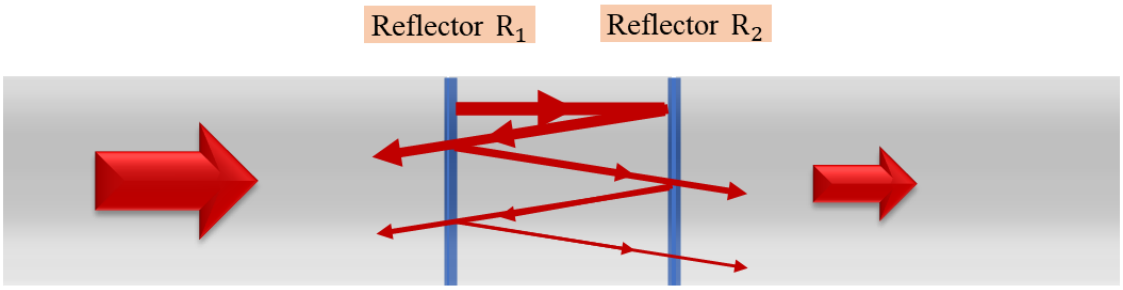


**Figure 8 Schematic of an optical fiber consisiting of IFPI at fiber core.**

The interrogating light with intensity $I_0$ was launched into the optical fiber and produced reflection and transmission repeatedly within cavity of IFPI. The $n^{th}$ reflected and transmitted light can be expressed as,

$$R^{(n)} = T_1^2 R_2 (R_1 R_2)^{n-1} \exp(-jn\varphi),$$
$$T^{(n)} = T_1 T_2 (R_1 R_2)^{n-1} \exp\left[-j\left(n - \frac{1}{2}\right)\varphi\right], \quad (2\text{-}4)$$

where $\varphi$ stands for the phase delay occurred at single round trip of interrogating light within FP cavity. The phase delay caused by OPD can be written as,

$$\varphi = k \cdot n_{eff} \cdot 2l + \phi, \tag{2-5}$$

where $n_{eff}$ is the effective refractive index of FP cavity at length $l$; $k$ is the wavenumber of interrogating light in vacuum, and $\phi$ is the phase variation induced by external forces. When the reflectance of two partial reflectors are approximately the same $R$, the simplified reflectivity and transmittivity of IFPI can be demonstrated as,

$$\begin{aligned} R_{FP} &= \frac{F sin^2 \frac{\varphi}{2}}{1 + F sin^2 \frac{\varphi}{2}}, \\ T_{FP} &= \frac{1}{1 + F sin^2 \frac{\varphi}{2}}, \end{aligned} \tag{2-6}$$

where $F$ is the finesse coefficient. The finesse depends upon the reflectance of FP reflector which is insensitive to cavity length,

$$F = \frac{4R}{(1-R)^2}, \tag{2-7}$$

The finesse coefficient was also determined by free spectral range (FSR) over the bandwidth of FP resonances. The spacing between two adjacent fringes from the interference pattern is defined as FSR. By ignoring the wavelength-dependent effective refractive index, FSR can be approximated as [70],

$$FSR = \Delta\lambda = -\frac{2\pi}{l}\left(\frac{\partial\beta}{\partial\lambda}\right)^{-1} \approx \frac{\lambda^2}{n_{eff} l}, \tag{2-8}$$

where $\beta$ is the propagation constant within the FP cavity. FSR manifests the dependency between interference pattern and wavelength of interrogating light at constructive interference. If the phase difference in a round trip of FP cavity is the integer number of 2π, partially reflected in interrogating lights, then a constructive interference can be generated,

$$\varphi = k_m \cdot n_{eff} \cdot 2l + \phi = m \cdot 2\pi, \tag{2-9}$$

$$k_m = \frac{2\pi}{\lambda_m} = \frac{m \cdot 2\pi - \phi}{n_{eff} \cdot 2l}, \tag{2-10}$$

where $m$ is a positive integer number called the peak order. Due to constructive interference, the peaks of fringes depend upon OPD within FP cavity and phase noise from external stress. By detecting the interference pattern using white-light or scanning-white-light interrogation methods, the stress-induced phase delay can be accurately extracted. The intensity of interference pattern can be expressed as [71],

$$I(k) = I(k) = 2I_0(k)[1 + \gamma \cos(\varphi)] = 2I_0(k)\left[1 + \gamma \cos\left(2kn_{eff}l + \phi\right)\right], \tag{2-11}$$

where $\gamma$ is the fringe visibility which quantifies the contrast of interference. The phase variation $\phi$ caused by external stress can be demodulated using the measured intensity.

## 2.3 Intrinsic Scattering of Optical Fiber

During transmission, material absorption loss is predominant. Light interacts with the constituent molecules resulting in photon-induced molecular vibration, which absorbs the light

energy and turns it into heat. Fused silica has two notable absorption bands located at ultraviolet (UV) and infrared (IR) regions. The doping impurities and residuals from fabrication creates additional absorption commonly referring to as OH ions. Apart from extra ions, the fabrication process also introduces irregularities such as micro-bending during fiber drawing. It also incurs mode coupling between the fundamental mode to higher order modes which generates the loss.

Another factor of fiber loss is spontaneous scattering. Part of light is redirected to the cladding or back to the source due to intrinsic scattering mechanisms. There are mainly three types of spontaneous scattering caused by elastic and non-elastic effects: Rayleigh, Brillouin and Raman. They involve interactions between external incident light and microscopic molecule movements [47].

Two non-elastic scatterings are Brillouin and Raman. Photons may lose or gain energy during the scattering process. In addition to being scattered by local irregularities, molecule vibration and electron excitation is also involved in the scattering process. When the wavelength of transmitting light is large enough to compare the distance between each molecule, intermolecular oscillation can be induced by electrical field of light. The collective oscillations generate large scale phonons which give rise to the frequency shift of scattered light. The scattering that involves phonons generation is named Brillouin. Besides, a small number of photons join vibrational and rotational transitions in the bonds between atoms. They are absorbed or emitted by electrons which precisely match the difference of their energy levels. The scattered light with frequency shift by effect of electron excitation is called Raman scattering.

Spontaneous scattering only takes place when the intensity of light is inadequate to change the property of the material. If optical property of the material is modified by a high-power incident light, a transition of the medium's behavior from a linear to a non-linear regime happens which is

called stimulated scattering. Brillouin and Raman can be stimulated and become more evident by pumping a high-intensity continuous light. Photons from the pump are annihilated to create more photons at the probe. By improving the efficiency of a nonlinear process, a wide variety of nonlinear effects can be observed in an optical fiber [72]. However, their application in ultrasound detection were severely limited due to the time-consuming gain spectrum scan.

Rayleigh is the only elastic scattering that occurs when light propagates in an optical fiber. It has been widely used to detect vibrations due to the ease of amplitude measurement at single frequencies. Unlike nonelastic scattering that requires scanning gain spectrum, Rayleigh scattering utilizes no energy transformation and/or frequency shifts which provides a fast response of dynamic measurement.

In a small spatial scale, molecules and molecule clouds are small enough to compare with a wavelength of transmitting light. A small portion of mutually incoherent electromagnetic (EM) fields between adjacent molecular clouds collectively respond to external light incidence and are orientated to perform macroscopic polarizations. The collective EM polarization induces a secondary light emission in all directions with the same energy which is Rayleigh scattering.

For an unpolarized input light, the ratio between the intensities of secondary light emission and incident light at distance $r$ and angle $\phi_z$ apart from the scatter can be described as:

$$\frac{I}{I_0} = \frac{8\pi^4 \nu^4 a^2}{c^4 r^2}(1 + cos^2\phi_z), \tag{2-12}$$

where $\nu$ is light frequency, $a$ is polarizability and $c$ is speed of light in vacuum. Therefore, the intensity of Rayleigh scattering is proportional to the incident power and inverse fourth power of the wavelength.

The quantity of the secondary light emission is largely determined by the dielectric parameter fluctuation of the material. Fused silica has molecule level irregularities such as microscopic defects and inhomogeneities. Those random orders of non-propagating density fluctuation in the material can be treated as the source of Rayleigh scattering [73]. The fluctuation of the dielectric constant $\Delta\epsilon$ can be used to represent these irregularities. Additional polarization induced by $\Delta\epsilon$ can be written as [74]:

$$\boldsymbol{P} = \Delta\chi \boldsymbol{E_0} = \Delta\epsilon \boldsymbol{E_0}, \tag{2-13}$$

where $\Delta\chi$ is the fluctuation in the susceptibility from the relation $\epsilon = 1 + \chi$. Hence, the Rayleigh-scattering coefficient of a random medium can be characterized by the variance $\langle\Delta\epsilon^2\rangle$ and correlation length $l_c$. By calculating the total scattered power over the solid angle $4\pi$, the Rayleigh-scattering coefficient can be obtained as [75]:

$$\alpha_R = \frac{16}{3} k^4 \langle\Delta\epsilon^2\rangle l_c^3 \qquad Booker - Gordon\ Mode, \tag{2-14}$$

$$\alpha_R = \frac{2\sqrt{\pi}}{3} k^4 \langle\Delta\epsilon^2\rangle l_c^3 \qquad Gaussian\ Model, \tag{2-15}$$

where $k$ is the wave number. The difference between the two models arises from the ratio of the integrals during calculations. If correlation length is much shorter than wavelength, then results are model independent.

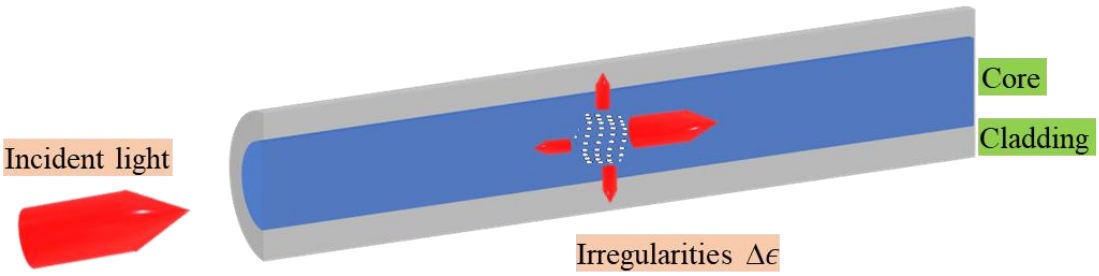


**Figure 9 Schematic of spontaneous Rayleigh scattering.**

The propagating light in optical fiber is elastically scattered to all directions which is simply illustrated by the schematic diagram in Figure 9. Some of scattered lights are redirected into cladding while some of them are recaptured by the fiber and generates a backward transmission. Supposed the incident light has a temporal width, $T$, and the intrinsic absorption of optical fiber, $\alpha$, then it is possible to write the power of Rayleigh backscattering after a single completely round trip as:

$$P(z) = P_{in}\left(\frac{v_g T}{2}\right) \cdot \alpha_R \cdot S \cdot exp(-2\alpha z), \tag{2-16}$$

Here $v_g$ is the group velocity of light in the optical fiber, $S$ is the recapture factor in single mode fibers and $\alpha_R$ is Rayleigh-scattering coefficient. $S$ is a constant related to the core diameter and is the refractive index of the optical fiber. For a single mode fiber, $S = 9.6 \times 10^4$, if $\Delta = 0.2\%$.

Therefore, the power of backscattered light at the input end as compared to the input power can be described as:

$$10\log\left(\frac{P(z=0)}{P_{in}}\right) = 10\log\left(\frac{v_g T \cdot \alpha_R \cdot S}{2}\right) = -55\ dB, \tag{2-17}$$

where $v_g = 2 \times 10^8\ m/s$, $T = 200ns$ and $\alpha_R = 1\ dB/km$ for normal single mode fiber.

A simple discrete model to describe the principle of Rayleigh backscattering has been reported previously [76]. It simulated the interference of Rayleigh backscattering as s summary of reflected light from finite scatters. Figure 10 illustrates the interference of the various reflections that occurred at location $z$ when using pulsed light during interrogation. The backward lights passing the location $z$ contained all Rayleigh backscattering in the range of $z$ to $z + \frac{\Delta z}{2}$, where $\Delta z$ is the distance of light propagation during the time of a single pulse period.

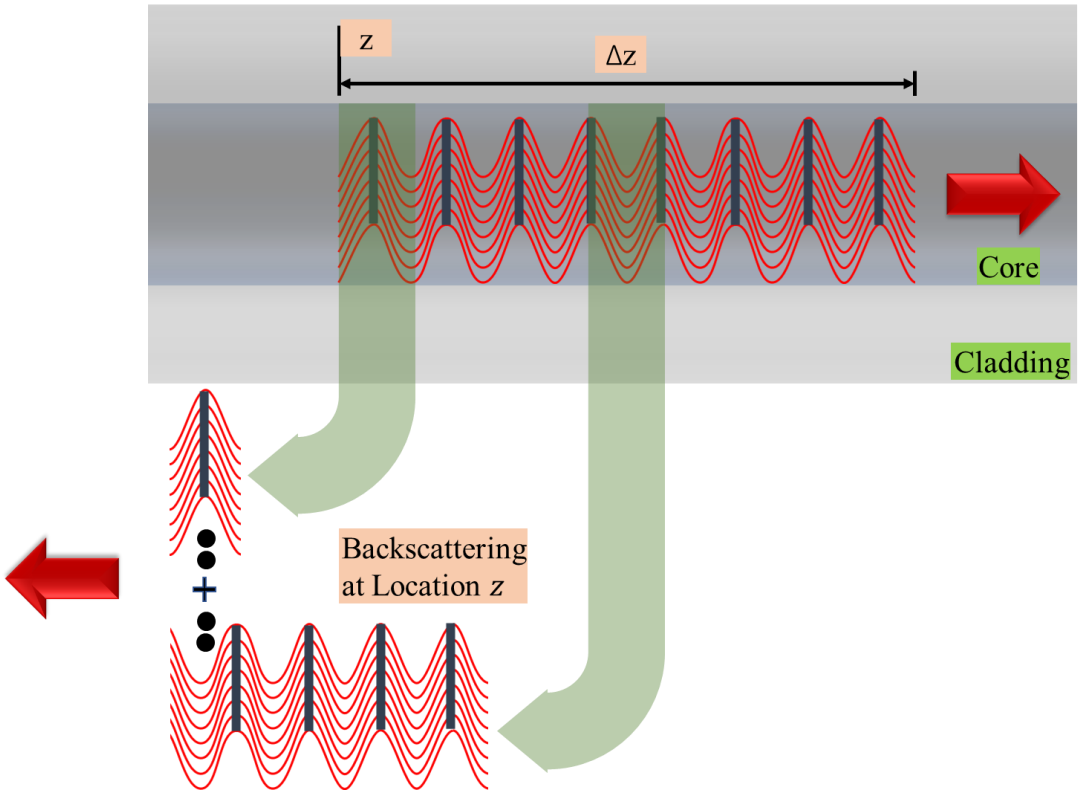


**Figure 10 Schematic of Rayleigh backscattering from a pulsed light.**

A more useful form of the equation with integral operation can be derived to describe the interference field,

$$E_b(z) = E_0 \int_z^{z+\frac{\Delta z}{2}} \gamma_z e^{-\alpha z} e^{j\phi_z} dt, \tag{2-18}$$

where $\alpha$ is attenuation coefficient of optical fiber; $\gamma_z$ and $\phi_z$ are amplitude and phase of backscattering occurring at location $z$. The traveling distance $\frac{\Delta z}{2}$ of light in half pulse duration is well-known in Rayleigh OTDR design as the spatial resolution of the system. Within the length of $\frac{\Delta z}{2}$, the complex sum of backscattering from enormous scatters can be described using the attenuation coefficient of an optical fiber, as well as the amplitude and phase of backscattering at a specific location. This corresponds to different interrogation strategies to detect strain-induced decoupling or phase changes like loss-based OTDR and phase-sensitive OTDR.

## 2.4 Rayleigh Enhancement

The entire sensing system of an optical fiber sensor is composed of three parts: sensor fabrication, interrogation system design and signal processing. Together, these all work effectively together to achieve reliable strain measurement. In addition to basic sensing functions, pattern recognition grants the system the ability to identify abnormal events that occur outside the optical fiber. The false alarm within the identification system is strongly affected by SNR. The term that significantly determined the performance of the system is the SNR which stems from fringe visibility in interferometry or from the Rayleigh backscattering intensity in Rayleigh OTDR. Fringe visibility depends on the reflectance of the embedded reflector while the backscattering intensity is determined by the intrinsic Rayleigh coefficient. Both quantities should be kept in a moderate range to avert from multi-reflection and evident attenuation.

An intrinsically weak Rayleigh scattering profile of telecom grade in the optical fibers severely limits SNR in OTDR. To address the challenge of low SNR, several methods have been employed to increase Rayleigh scattering but with a complicated fabricating procedure and time-consuming photo-sensitization. Recent advances in ultrafast laser direct-writing has led to successfully enhanced Rayleigh scattering at a single point [77] or segment of optical fiber [78]. As compared to weak FBGs and deep ultra-violet Rayleigh enhancement, it can withstand high temperatures of up to 800℃ and is often stable in harsh environments, like highly reactive fuel gas.

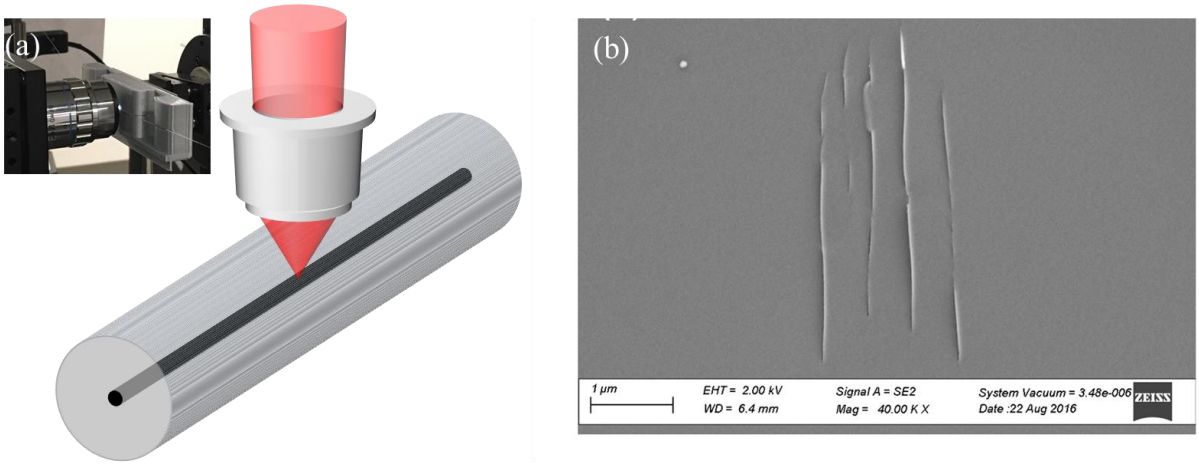


**Figure 11 Schematic of ultrafast laser direct-writing setup. (a) Laser pulse was radiated at optical fiber. (b) Scanning electron microscope (SEM) image of nano-reflectors morphology.**

Strongly pulsed laser light induced enhancement of Rayleigh scattering is a consequence of defects, reflected as discontinuities within the fiber core. It increases the fluctuation of the dielectric constant $\Delta\epsilon$ greatly. Figure 11 shows a schematic of ultrafast laser direct-writing setup and the SEM image of a typical microstructure written using a femtosecond-laser. This defect is similar to a permanent physical damage and works as a nano-reflector to scatter the interrogating

light at all wavelengths. The ultrafast laser enhancement of Rayleigh profiles in optical fibers is a general approach, which has been successfully applied to different types of optical fibers resulting in similar Rayleigh enhancement effects and temperature stabilities including those fibers with a high-temperature stable protective coating such as polyimide (up to 350℃) or fibers with dielectric coating ($TiO_2$) for higher temperature applications [79, 80].

The defects within the fiber core produce intensive Rayleigh backscattering which work as inline nano-reflectors. The dependency between pulse energy and the visibility profile of 1-millimeter IFPI was demonstrated in Ref. [71]. The insertion loss of each nano-reflector went up following an increase in pulse energy when inscribing severe nano-defects. The optimal pulse energy at the top of U-shape profile was 160nJ with 0.0012-dB loss.

## 3.0 Multi-point Ultrasound Sensing

Fiber FPIs become mature on ultrasound detection especially at single-point locations. Diaphragm-based FP cavity mounted at the fiber-end provided promising measurements by using quadrature point demodulation [81]. However, the drawback of fiber-end structure and intensity-based demodulation is the vacancy of multiplexing and susceptibility to environmental perturbations.

IFPI attracts a lot of attention due to its merits of multiplex scalability and ease of fabrication. Artificial Rayleigh scatters written by ultrafast laser direct writing is appropriate for being the reflectors of IFPI. Adequate enhancement of Rayleigh backscattering of two nano-reflectors constructs the interferogram by forming the FP cavity. Ambient stresses are detected through shifts of interference pattern. Serval researches on multiplexing weak reflectors as multi-points sensors were reported over the last decade. Most of them emphasized low-frequency stress measurements corresponding to temperature changes and static strain [77, 82, 83]. The bottleneck of low-speed spectrum-based demodulation has not been breached either with broadband CW light or scanning singe-wavelength laser [84]. The problems arise from the limited readout time of spectrometer in WLI and the linearity of sweeping frequency in a fast scanning source. The response speed of spectrometer is capped by a frame readout time of integrated charge-coupled device (CCD). The essential integration delay prevents the spectrometer from measuring the interferogram for ultrasound detection. Instead of employing full-spectrum acquisition, the use of a fast-swept laser improved the speed to obtain interference pattern without using spectrometers, however, this method lacks nonlinear frequency tuning.

## 3.1 Swept-frequency Interferometry

Swept-frequency interferometry makes use of vast and versatile measurements across several applications. With fixed-sweeping velocity, free-space ranging was achieved by using frequency-modulated continuous-wave radar [85]. Tunable-diode-laser absorption spectroscopy has been applied in the measurement of gas parameters over the last 40 years [86]. OFDR found the application of distributed temperatures and strain sensing in optical fibers [87]. Optical coherence tomography built a raster-scanning system for three-dimensional biological imaging [88].

### 3.1.1 Swept-frequency Laser

In fast swept-frequency interferometry, the sweeping rate, frequency linewidth and frequency range are vital characteristics to determine the performance of system. External-cavity lasers possess a large frequency range and narrow linewidth however, they also display discrete mode-hoping. Vertical-cavity surface-emitting lasers can be tuned by current injections or mechanical cavity change but these are limited within tens of MHz linewidth [89]. DFB was widely used in swept-frequency interferometry featuring high power output, stable single modes lasing and mode-hop-free tunability. High-speed modulation uses sweeping current injection which affects both bandgap and refractive index of the active layer on account of Joule heating. The heat generation and conduction along with thermal expansion causes the non-linearity of tuning wavelength [90]. Figure 12 shows the typical optical frequency deviation of DFB laser under fast current sweeping.

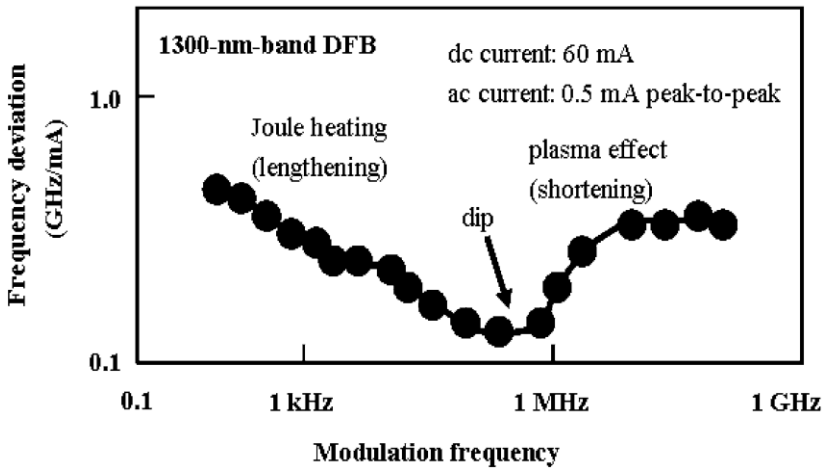


**Figure 12 The optical frequency deviation of DFB laser under fast current sweeping [90].**

Fast current modulation causes a dip caused due to detrimental competition between electrical tuning and thermal effect. The decrease of frequency deviation before the dip arises from a decline of the heat conduction response. The plasma effect that is dominant after the dip is known as the FM-response or chirping in the telecommunication [91]. Based on a lowpass-filter model of DFB laser frequency modulation, electrical tuning and thermal effects have opposite contributions to the refractive index of active layers [92]. The high-frequency modulation can break the weak response but again, there is a drawback of real-time nonlinearity control.

### 3.1.2 Laser Nonlinearity Control

The nonlinearity of instantaneous optical frequency in DFB laser sweeping invalidates spectrum analysis due to the distorted fringe pattern from the interferometer. Three aspects were investigated to ameliorate the nonlinear chirp rate, which focused on sweeping laser design [93], instantaneous phase locking or post-compensation [94], and resampled data acquisition[95]. Not all of these aspects were viable in ultrafast frequency sweeping especially for use in ultrasound

detection. The intrinsic speed limitation of mechanical modulation and thermal control pushed the current injection to become the only feasible driving source at high speeds. It is inevitable to have frequency nonlinearity from thermal effects such as heat generation and conduction following current modulation. Using interference pattern from an auxiliary interferometer to trigger acquisition for resampled data acquisition, can achieve equidistant frequency sampling. But the variation of the interference amplitude constrains its reliability due to the occurrence of sampling errors within the interferometric clock. And OPD between two arms of auxiliary interferometer pushes the sampling rate to the limitation of Nyquist Law [96]. Instead of employing various interference patterns to directly trigger data acquisition, concatenative reference methods were tried to emulate the use of multiple interferometers to increase the sampling rate [97]. However, the phase jitter and multiplication hardware remain challenging.

The use of an auxiliary interferometer provides transient monitoring of instantaneous optical frequency. The full interference pattern can be collected after a single scanning period. By obtaining the optical frequency or phase information within an interference pattern, the nonlinearity from laser tuning is proposed to be compensated based on two classes of algorithms: interpolation and phase unwrapping. Interpolation algorithms include linear or cubic spline interpolations [98] and non-uniform FFT [99] which do not have the restriction of OPD-dependent acquisition triggering, but suffer from phase noise. Phase unwrapping through Hilbert transformation eliminates the phase noise and effectively compensates nonlinearity, however this raises the problem of post-processing which is time-consuming [100].

The real-time locking of the chirp rate has been achieved by using an optoelectronic phase-locked loop (OPLL) [94, 101, 102]. Similar to implementing a fixed-delay auxiliary MZI to monitor the sweeping velocity of laser diode, the nonlinear chirp rate can be extracted by mixing

the beating interreference with external single-frequency reference. Figure 13 shows the typical frequency response of OPLL in small signal approximations using lock-in amplifier (LIA) as a phase extractor. External single-frequency reference was provided using a built-in direct digital synthesis of LIA. The phase difference from the LIA output renders the intuitionistic illustration of real-time laser sweeping velocity. It was fed back to a laser diode driver to lock the sweeping velocity to steady state.

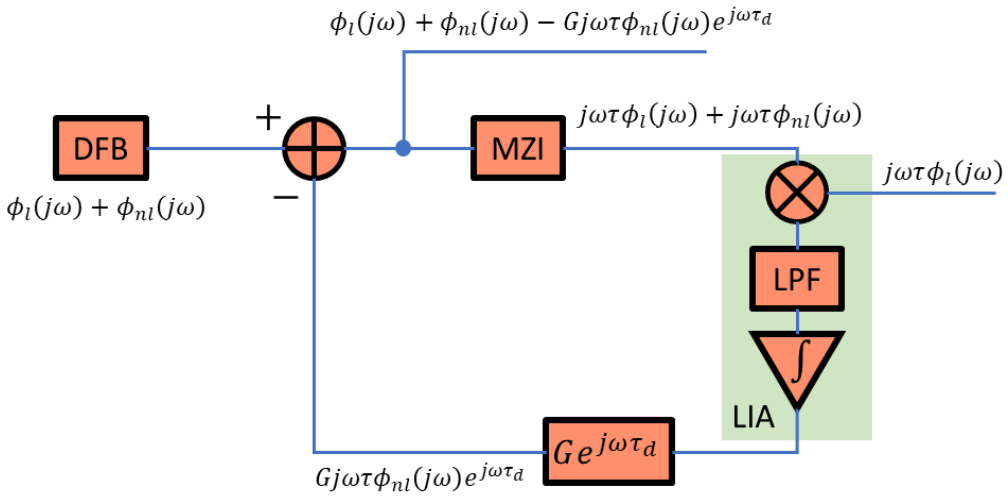


**Figure 13 The scheme of OPLL in frequency response analysis. DFB: distributed feedback laser; MZI: Mach–Zehnder Interferometer; LPF: Low-pass Filter; LIA: Lock-in Amplifier.**

The current injection to DFB laser induces a nonlinear sweeping that contains both linear and non-linear frequency components as an equation with quadratic form:

$$i_i(t) \propto \omega_l(t) + \omega_{nl}(t) = \omega_0 + \xi t + \gamma t^2, \tag{3-1}$$

where $\xi$ and $\gamma$ are the linear and non-linear coefficient of frequency sweeping, respectively. The laser output was fed into the auxiliary MZI with fixed time delay $\tau$ in its one arm. The beating

interference corresponding to the chirp rate of laser was connected to LIA for phase extraction. The fixed time delay $\tau$ was sufficiently small such that it could be neglected in cubic and quadratic varieties. Hence, the phase output of MZI is then:

$$\begin{aligned}\phi_{MZI}(t) = \phi_i(t) - \phi_i(t-\tau) &= \gamma\tau t^2 - \gamma\tau^2 t + \tau^3 + \omega_0\tau - \frac{1}{2}\xi\tau^2 + \xi\tau t \\ &\approx \gamma\tau t^2 + \omega_0\tau + \xi\tau t,\end{aligned} \tag{3-2}$$

Due to the mixing of the single-frequency reference and being filtered by a built-in lowpass filter in the LIA, the nonlinear chirp rate was embodied in the output of the phase difference. If setting the frequency of the reference signal to $\xi\tau$, the linear phase components were eliminated and left with only the nonlinear variables:

$$\phi_{LIA}(t) = \phi_{MZI}(t) - \phi_{ref}(t) \approx \tau\big(\omega_l(t) + \omega_{nl}(t)\big) - \int \xi\tau dt = \omega_{nl}(t)\tau, \tag{3-3}$$

Given the inherent gain $G$ and electrical delay $\tau_d$ in the circuits, and supposing the system is a linear time-invariant system, the frequency response of LIA phase output becomes:

$$\phi_{LIA}(j\omega) \approx Gj\omega\tau\phi_{nl}(j\omega)e^{j\omega\tau_d}, \tag{3-4}$$

The integral part of LIA generated a phase-dependent voltage output working as a phase detector. Through the electrical feedback loop, the voltage signal was launched back to a LD driver as external modulation. It was proportional to additional current injections as a correction to the original sweeping current. The relationship between the feedback current and phase output of LIA could be simplified as,

$$I_{LIA}(j\omega) \propto \phi_{LIA}(j\omega) = Gj\omega\tau\phi_{nl}(j\omega)e^{j\omega\tau_d}, \quad (3\text{-}5)$$

By subtracting the feedback current from DFB current injection, the phase output of OPLL turns into:

$$\phi_o(j\omega) = \phi_l(j\omega) + \phi_{nl}(j\omega) - Gj\omega\tau\phi_{nl}(j\omega)e^{j\omega\tau_d}, \quad (3\text{-}6)$$

In the steady state and small period of $\tau$, the non-linear component within the output phase could be cancelled. Only the linear frequency component that was left to serve as a locking to reference signal with single frequency.

## 3.2 Ultrasound Demodulation

Swept-frequency DFB interrogating IFPI generates a temporal fringe pattern by sweeping the frequency for laser output. The instantaneous resonance frequency of FP cavity can be demodulated through analysis of time-frequency representation (TFR). The effectiveness of TFR in audio signal processing and ultrasonic inspection have been studied previously [103, 104]. Popular decomposition strategies including short time Fourier transform (STFT), wavelets transform (WT) and Wigner-Ville distributions (WVD) have also been previously investigated. Furthermore, enormous linear and nonlinear denoising techniques have been developed following these common TFRs. The two-dimensional spectrogram becomes effective to depict joint time-frequency energy content precisely.

All TFRs share the same intrinsic limitation as denoted by the Heisenberg uncertainty principle that perfect resolution in both time and frequency cannot exist simultaneously [105]. Like in STFT, the narrow window brings an excellent time resolution but terrible frequency resolution, and vice versa. Keeping high resolution in both domains is unattainable. This is similar to a frequency-dependent time-frequency resolution in WT which has a superb frequency resolution at low-frequency and carries an awful time resolution. WVD automatically finds the balance point within the uncertainty principle, however, suffers from interference terms occurring in signals of various multicomponent. Although smoothing the WVD with a Gaussian filter eliminates the interference terms, the resolution uncertainty is changed to be determined by a Gaussian filter design. It also induces additional tradeoffs between interference attenuation and time-frequency concentrations [106].

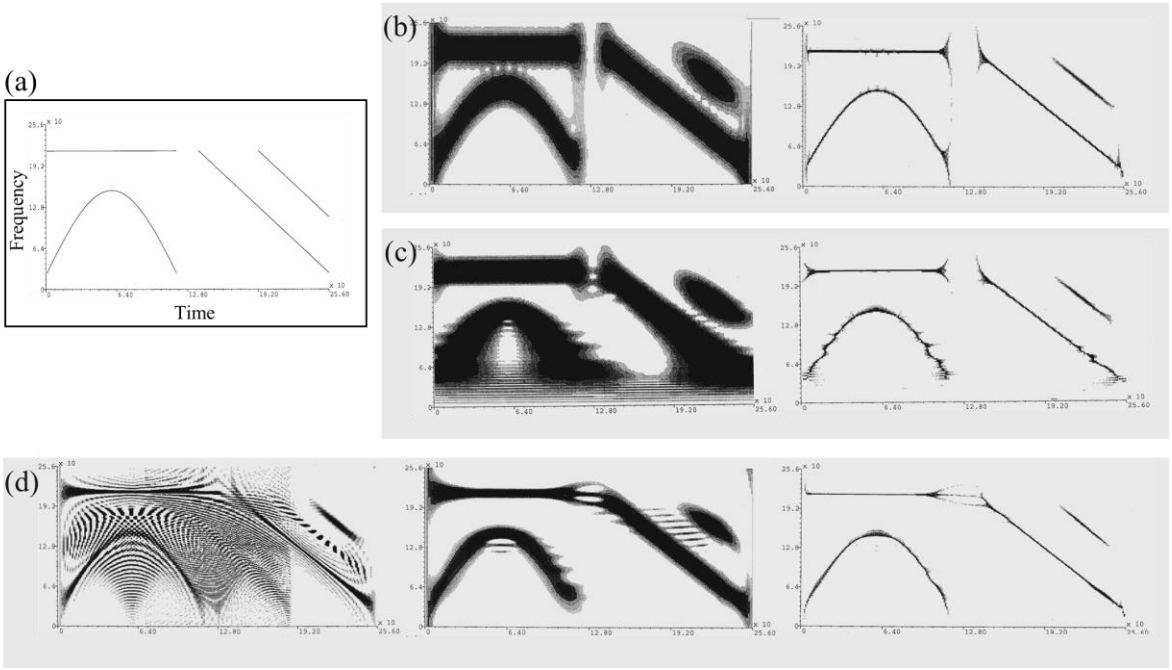


**Figure 14 TFRs for time- frequency decomposition. (a) Initial four frequency components; (b) STFT and its reassignment; (c) WT and its reassignment; (d) WVD, smoothed pseudo WVD and reassigned smoothed pseudo WVD [107].** 

As a complement to improve the time-frequency resolution, reassignment was commonly used in all TFRs through mapping the signal to the reassigned coordinates that concentrates its energy at the center of gravity [107]. Figure 14 shows the summary of these popularly applied TFRs to a spectral input with four frequency components. Among all TFRs, STFT is undoubtably the most popular decomposition algorithm with a well-developed analysis tool in speech recognition [108]. Moreover, previous studies have proven the high-fidelity measurements in ultrasonic frequency range with the help of a reassigned STFT [109].

STFT has segmented the temporal signal into multiple pieces by defining a window hopping through the entire signal. A series of small overlapping pieces represented as segments are processed by the Fourier transform individually. The STFT of temporal signal $s(t)$ with window function $h(t)$ can be expressed as:

$$S(\omega, t) = \frac{1}{2\pi} \int_{-\infty}^{\infty} e^{-i\omega\tau} s(\tau) h(\tau - t) d\tau, \tag{3-7}$$

Its energy density spectrum is named as a spectrogram. In the spectrogram of STFT, the Heisenberg uncertainty principle restricts the time and frequency resolutions. The standard deviations of time $\sigma_t$ and frequency $\sigma_f$ in the window function are closely interrelated and meet the inequality [110]:

$$\sigma_t^2 \sigma_f^2 \geq 0.25, \tag{3-8}$$

Selection of an appropriate window and hop length is very important to determine the time-frequency spread of a spectrogram. The Hanning window with $\sigma_t^2 \sigma_f^2$ at around 0.2635 is preferred

since it involves a compromise between maintaining the shape of the temporal signal and continuing across the boundaries of the windowed signal.

Using reassignment to improve the time and frequency resolution moves the energy center of the spectrogram to the new coordinates. The reassigned coordinates can be demonstrated as:

$$\hat{t} = t - Re\left(\frac{S_{Th}(\omega,t)S_h^*(\omega,t)}{|S_h(\omega,t)|^2}\right),$$
$$\widehat{\omega} = \omega - Im\left(\frac{S_{Dh}(\omega,t)S_h^*(\omega,t)}{|S_h(\omega,t)|^2}\right), \quad (3\text{-}9)$$

where $S_h$, $S_{Th}$ and $S_{Dh}$ are STFTs of $s(t)$ with window functions $h(t)$, $th(t)$ and $dh(t)/dt$, respectively. With the help of reassignment, the spectrogram sharpened the ridges of the spectral estimation and allowed it to be extracted by tracking the ridges at the true center of the spectral energy. Through mapping the maximum-energy time-frequency ridge to a continuous line, the dynamic signal was obtained from reassigned STFT.

### 3.3 System Design

The temporal fringes from swept-frequency interferometry generate time-frequency spectrogram by using TFRs. The spectral energy center represents the estimate of OPD within the interferometer's reaction to external stress. The number of fringes per second serves as the sampling rate of the interrogation system. Furthermore, the time interval between adjacent fringes implies a linearity of laser sweeping. Increasing the number of temporal fringes and equalizing the

time interval between them improves the demodulation accuracy, as well as the upper limit of the detectable frequency range.

### 3.3.1 Sensor Fabrication

The long-length FP cavity compensates the poor response of low-frequency modulation while maintaining control of nonlinearity to remain viable. The small FSR of fringe pattern from the long FP cavity gives rise to more temporal fringes within each scan. In turn, this expedites the sampling rate of interrogation that provides an accessible solution for ultrasound detection.

For a long FP cavity, maintaining polarization is extremely important to avoid polarization mode shift that destroy the fringe pattern. PM fiber can be used to fix the problem with strong built-in birefringence. The polarization status of transmitting light that matches one of the birefringent axes is preserved throughout entire fiber. The high birefringence brings a large difference in propagation constant between two polarization modes. Due to the principle of coherent mode coupling, varying ambient perturbations have significant impact on the polarization status of the transmitting light but only when its spatial wavenumber exactly matches the propagation constant difference. Usually, the PM fiber owning several millimeters polarization beating length which is in tantamount to a frequency difference of tens of GHz propagation constants. It is far from enough for ultrasound detection. Overall, fabricating IFPI in PM fiber has been a challenge with conventional micromachining or splicing. Any deformation of the birefringent axes in PM fiber brings about inferior influence on polarization maintaining.

Nano-reflectors written by ultrafast laser are right for inline IFPI within a PM fiber. Precisely targeting the femtosecond pulse inside the fiber core averts from damaging the birefringent axes of PM fiber while inscribing the Rayleigh enhanced points. The strength,

location, and section length of nano-reflectors are all controllable and can be be flexibly achieved during the fabrication process.

The detailed manufacturing process was described in a previous report [78]. Femtosecond-laser consisting of a Coherent MIRA 900 Ti: sapphire mode-locked oscillator and a Coherent RegA 9000 regenerative amplifier operated at 800 nm with 250 kHz repetition rate and 270-fs pulse duration. A cylindrical telescope was used to shape the laser beam and control the shape of the focal volume inside the core of a PM fiber (Thorlabs, PM1550-XP). In total, four nano-reflectors were inscribed within the core area at an on-target pulse energy of ~160nJ. The size of each nano-reflector was estimated to be 2×2-μm (Cross-section) by 7-μm (Length). The insertion loss showed a 0.0012 dB per nano-reflector [71]. Figure 15 illustrates the schematic of nano-reflectors inside the PM fiber, and their backscattering profile interrogated by an optical backscatter reflectometry (Luna OBR4600). The inline cavity length of two IFPIs was designed to be 10cm and 20cm respectively.

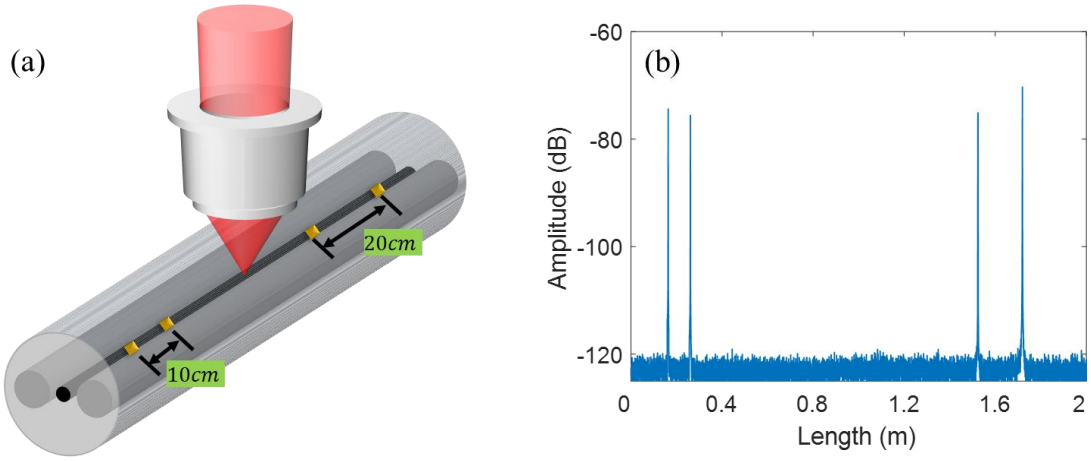


**Figure 15 Fabrication of nano-reflectors within PM. (a) The schematic of nano-reflectors inside PM fiber. (b) Backscattering profile of two inline IFPIs interrogated by Luna OBR4600.**

### 3.3.2 Interrogation System Design

High-speed ultrasound detection has great appeal to many applications but has a high system design requirement. Conventional WLI provides a reliable method for dynamic strain measurement but was capped by a low speed spectrometer. With the help of a DFB laser, swept-frequency interferometry can break the speed limit however, this is in the absence of proper chirp control. The frequency deviation in each scan depends on detrimental competition between electrical tuning and thermal effect. It brings about nonlinearity of frequency tuning and a decline in sweeping range at low-speed current modulation. The accuracy of spectral analysis with TFRs and fringe numbers as sampling rate are doomed to be restricted. Figure 16 shows the experimental setup that was used to construct an effective ultrasound sensor. OPLL and long-length IFPIs were adopted to solve those concerns.

This system implemented a DFB laser (QPHOTONICS, QDFBLD-1550-50N) with 45-mW output and less than a 1-MHz linewidth as a sweeping source. The laser was driven by an internal ramp current from the LD controller (Thorlabs, ITC4001) to provide sweeping optical frequency. Most of the light passing through a fiber splitter was launched into inline IFPIs for ultrasound detection. The backscattering interference from long-length IFPIs was captured by an avalanche photodetector (Thorlabs, APD 410C). The other 1% was launched into an auxiliary MZI for the purpose of OPLL. The instantaneous sweeping velocity of DFB laser was monitored by a LIA (Stanford Research, SR830) in real-time. LIA generated a single-frequency reference from a built-in direct digital synthesis. Through mixing the beating interference of auxiliary MZI with single-frequency reference signal, the spectral variation of beating interference was embodied in the phase difference between them. The voltage output of LIA was proportional to the phase

difference through mixing and filtering. It was sent back to the LD driver as an instantaneous correction to sweeping velocity.

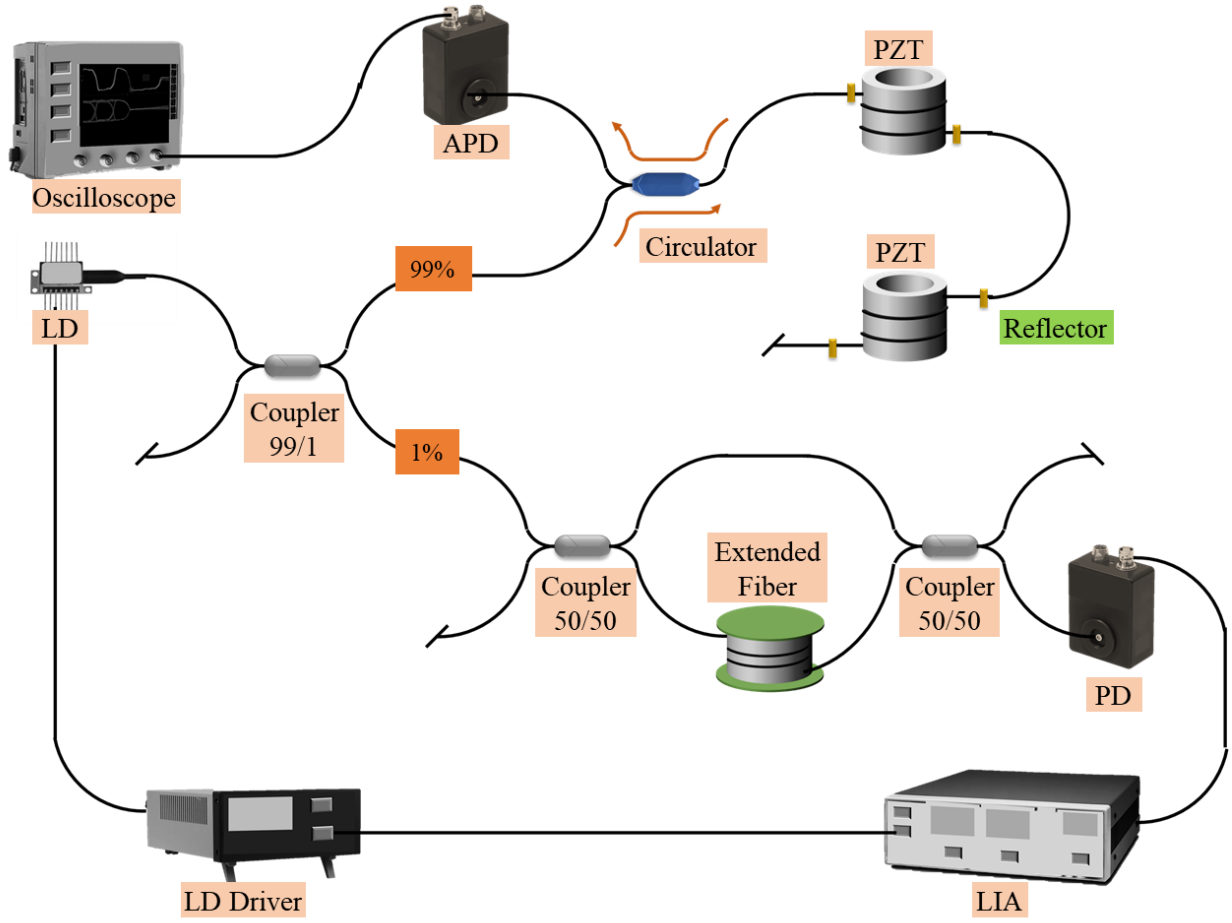


**Figure 16 The schematic of multi-points ultrasound fiber sensor. (APD: avalanche photodetector)**

Long-length IFPIs were created for the large number of temporal fringes from swept-frequency interferometry under low-speed current modulation. The number of temporal fringes per second was increased due to the small number of FSR on account of the long-length cavity. Adequate fringe numbers corresponding to high-speed samplings subsequently become capable on ultrasound detection. Largely different FSR values from various cavity length features separated and isolated the energy center in TFRs. Multi-points IFPIs can be achieved by tracking

energy centers located at the parted spectral range. The reassigned STFT with a simple algorithm and reliable performance for ultrasound demodulation was chosen to validate this multi-point interrogation system.

### 3.4 Ultrasound Detection

Swept-frequency DFB laser was used to interrogate inline IFPIs and return the temporal fringe pattern to a photodetector. The chirp rate of DFB laser was locked to steady state by using an OPLL consisting of auxiliary MZI and LIA. The DFB laser was driven by a 400Hz symmetrical ramp current considering the capability of electrical components in LIA and inferior frequency response of laser source. A 30-cm long single mode fiber was used to construct a fixed-delay in one arm of MZI.

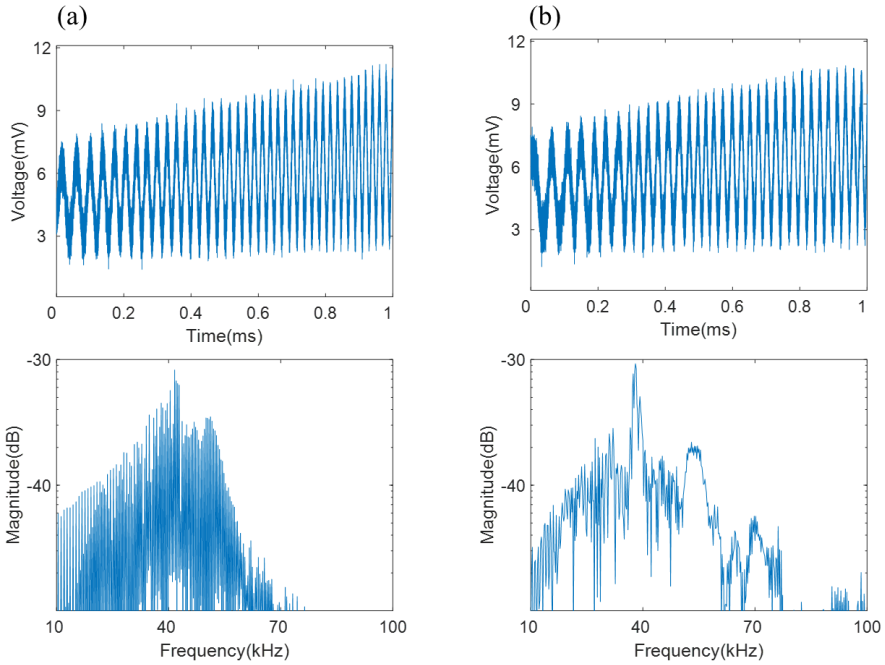


**Figure 17 The interference pattern of auxiliary MZI and its spectrum (a) without OPLL or (b) with OPLL .**

The sweeping velocity was calculated to be 25.13 THz/s, which brings a 37.7 kHz beating frequency of interference pattern in MZI. The single-frequency reference generated from LIA was also set to the same value to monitor the phase difference between them. Figure 17 shows the spectrum of interference pattern in auxiliary MZI with either OPLL or not.

The auxiliary MZI and LIA provided real-time feedback to lock the chirp rate of the DFB laser. After successful locking, the energy center of spectral interference was evidenced to be focused at 37.7 kHz. Better linearity of laser sweeping was confirmed to be achieved.

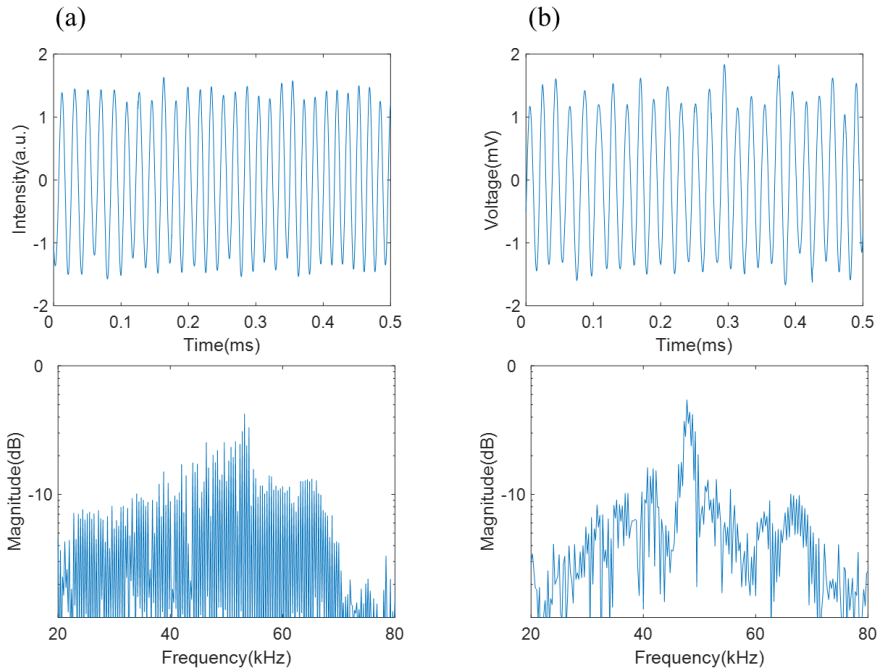


**Figure 18 The interference pattern of 20 cm IFPI and its spectrum (a) without OPLL or (b) with OPLL.**

With the help of phase-locked laser, two IFPIs with 10 cm and 20cm cavity length were interrogated to generate temporal fringe pattern. Similar to the fringe pattern from auxiliary MZI, ramp current injection to a DFB laser brought a fluctuation of intensity in interference. It deteriorated the time-frequency analysis of reassigned STFT which involved additional intensity

noise. Lowpass filtering and root mean square average were taken as pre-processing to normalize the fringes. Figure 18 shows the spectrum of interference pattern from the 20 cm IFPI, which compared the use of OPLL. The energy center of spectrum changed and was located at 48 kHz after phase-locking. It is equivalent to 48 kHz sampling rate in dynamic measurement.

The ambient ultrasonic perturbation was mimicked by wrapping the IFPIs on the surface of a piezoelectrical ceramic cylinder. The high-frequency sinusoidal voltage from the function generator was amplified by voltage amplifier (MATSUSADA HEOPS-0.6B50) then used to drive a piezo-cylinder. Ultrasonic dynamic strain which occurred at the optical fiber was calculated to be 2.4 με and stemmed from the calculation of dimension, voltage, and piezoelectric constant of PZT.

The temporal fringes pattern from IFPIs were launched into reassigned STFT to decompose the time-frequency spectrogram. The stress-induced interference changes can be revealed as shifts of spectral energy center. Figure 19 shows the spectrogram of interference pattern from 20 cm IFPI which showed evidence of a spectral energy center shift. The dynamic vibration can be extracted by tracking the ridges with maximum energy.

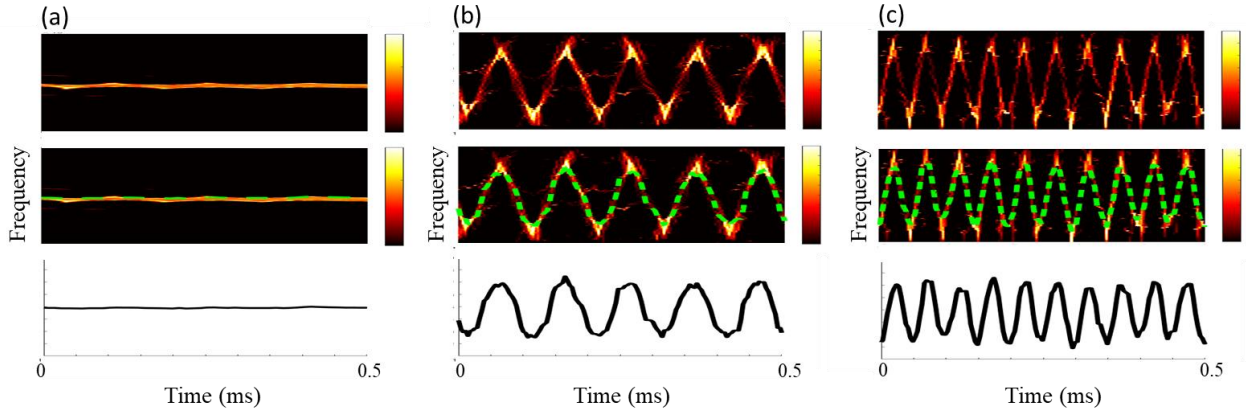


**Figure 19 The spectrogram of interference pattern from 20 cm IFPI and automatic ridges extraction. The vibration frequency of piezo-cylinder was set to be (a) 0-Hz; (b)10-kHz; (c)20-kHz.**

The finesse of temporal fringes from IFPIs was determined using the reflectance of nano-reflectors within the PM fiber core. Maximum finesse was achieved when the reflectance of two reflectors are equal. Manually writing nano-reflectors into the fiber core by using ultrafast laser is impossible to keep the same reflectance. Reassigned STFT offer finesse-insensitive solutions for dynamic strain demodulation, as well as multiplex scalability.

Multi-points detection was achieved by cascading another 10 cm IFPI following the previous 20 cm IFPI within same PM fiber. It was wrapped and glued around another identical piezoelectrical ceramic cylinder. The same voltage amplifier was used to drive the second piezo cylinder but changed to opposite bias. Figure 20 shows the spectrogram of interference pattern from the two IFPIs affected by 1.6 kHz piezo vibration at different bias directions.

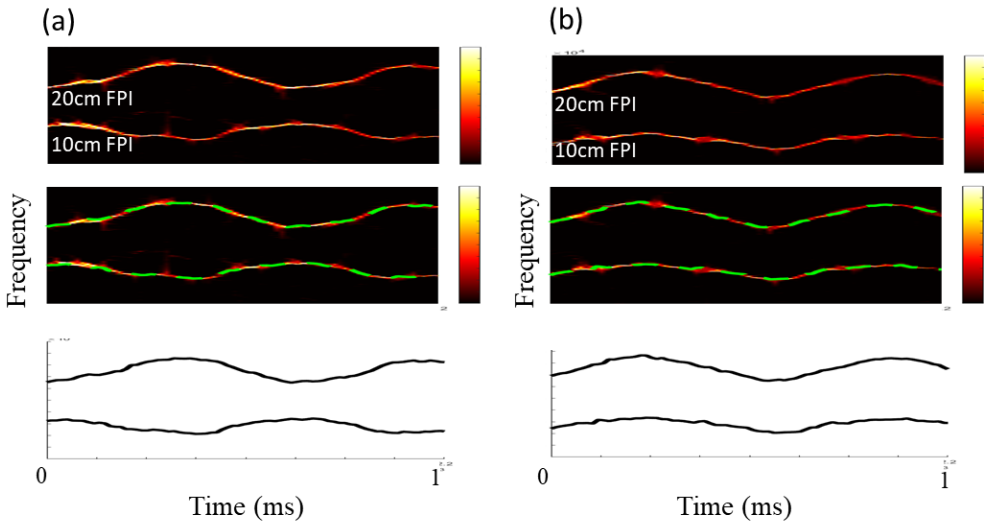


**Figure 20 The spectrogram of interference pattern from two IFPIs and automatic ridges extraction. The vibration frequency of piezo-cylinder was set to be 1.6 kHz at (a) opposite bias or (b) identical bias.**

The separated spectral region related to two different cavity lengths was illustrated through the spectrogram. However, the current 48 kHz sampling rate curbed ultrasound recognition at a

higher detectable frequency. The crosstalk between two separated spectral regions limited the performance of the reassigned STFT, especially when considering the Heisenberg uncertainty principle. Fringe numbers in each segmented window determined the time resolution of spectrogram, as well as the upper limit of detectable frequency range. The experimental piezo vibration was enforced and kept at a low frequency to achieve adequate visualization of the spectral shift while averting from crosstalk. Higher sampling rate was desirable for a wide detectable frequency range.

## 4.0 Distributed Ultrasound Sensing

Distributed fiber sensors utilize the intrinsic attenuation of optical fiber to measure the ambient environmental change. The reduction in intensity of the light over long-distance transmission is the result of absorption, bending and scattering. They form the basic concept of distributed sensing.

### 4.1 Conventional Optical Time-domain Reflectometry

In Rayleigh-based OTDR, the impurities in optical fiber absorb part of the incident light due to certain ions while increase the quantity of scattering based on secondary light emission. The bending caused decoupling as lateral dielectric constant change affects those secondary lights in terms of intensity, phase and polarization. In order to capture those secondary lights solely, the only feasible way is to detect the backscattered light at input end since part of them are recaptured into fiber and propagate backward. And the location of bending can be extracted by utilizing the travelling time of a light pulse because of constant light speed in optical fiber. Hence the ambient physical perturbation can be profiled along the fiber length which is called Rayleigh OTDR.

Figure 21 shows a typical structure of Rayleigh OTDR. A narrow pulse is generated by optical modulator and amplified by Erbium-doped fiber amplifier (EDFA). It then launches into sensing fiber to probe the fiber under test. The Rayleigh backscattering signals are collected in photodetector and digitized into data processing. Since the signals are in time-domain, it is equivalent to the distance of pulse travelling. In a round trip of light in optical fiber as incidence

and backscattering, the location accuracy can be described by pulse width $\tau$ and speed of light $c/n_{eff}$,

$$\Delta z = \frac{\tau c}{2n_{eff}}, \tag{4-1}$$

where $n_{eff}$ is the effective refractive index of optical fiber. The location accuracy is commonly named as spatial resolution in OTDR.

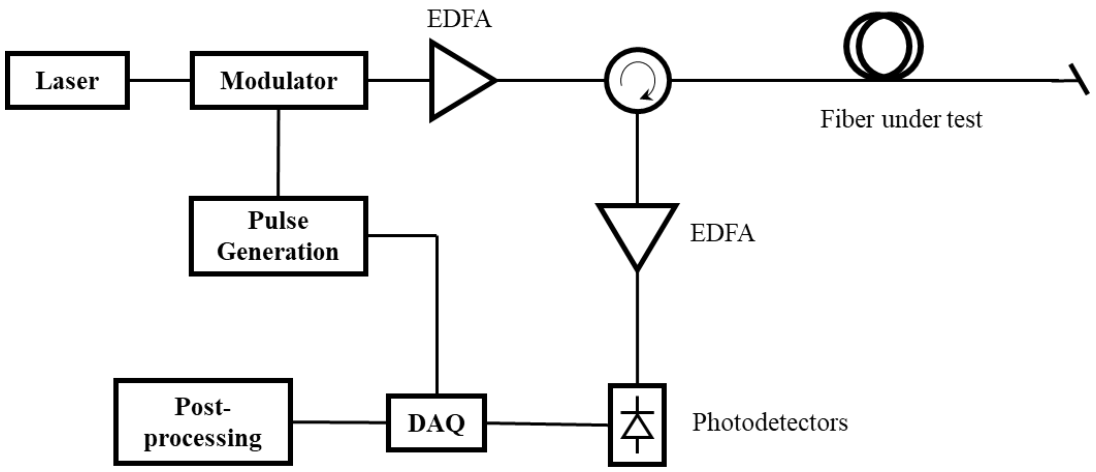


**Figure 21 Schematic of typical Rayleigh OTDR. (EDFA: Erbium-doped fiber amplifier; DAQ: data acquisition)**

In 1976, the first OTDR was reported to measure the loss of optical fiber along with estimation of scattering and mode mixing. [44] The system implemented a short pulse with broad linewidth to probe a single mode fiber following backscattering detection. The intensity of backscattered light conveys the information of absorption and physical discontinuities. Figure 22 shows the result of conventional intensity sensitive OTDR.

The slop of Rayleigh trace implies the decaying intensity which presents attenuation coefficient of optical fiber. And the isolated peaks are the location of high reflection caused by

discontinuities of optical fiber such as cracks and connectors. There are also some mild disorders of material like bends and fusion splices performing as slight drop on Rayleigh trace.

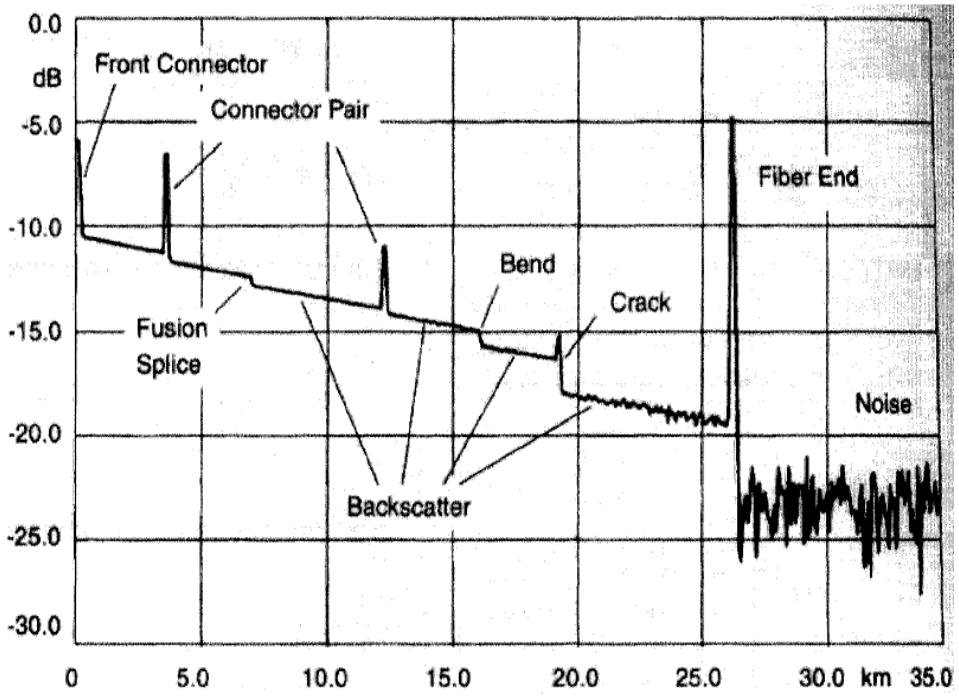


**Figure 22 The result of Rayleigh trace in intensity sensitive OTDR [111]**

However, for normal silica fiber, the dependence of Rayleigh backscattering intensity on micro-bending is too weak to construct an effective sensor. The performance of temperature and dynamic vibration measurements are significantly limited. The only practical application of conventional OTDR is to find high loss section of optical fiber in telecommunication industry.

### 4.2 Phase-sensitive Optical Time-domain Reflectometry

Several properties of backscattered light are affected by local perturbations, which includes the phase of light. For fiber as a perfectly symmetric waveguide, light in the core region is

considered as a plane wave with Gaussian radial distribution. The phase of light can be regarded as location of wavefront. To measure the phase change, the system alternates to use temporal coherent light. With well temporal coherence, the wavefront of transmitting light is evenly distributed along optical fiber. Any phase change induced by perturbations disorganizes the order of wavefronts and carries the information of those perturbances. Figure 23 shows the illustration of wavefront variations induced by perturbations.

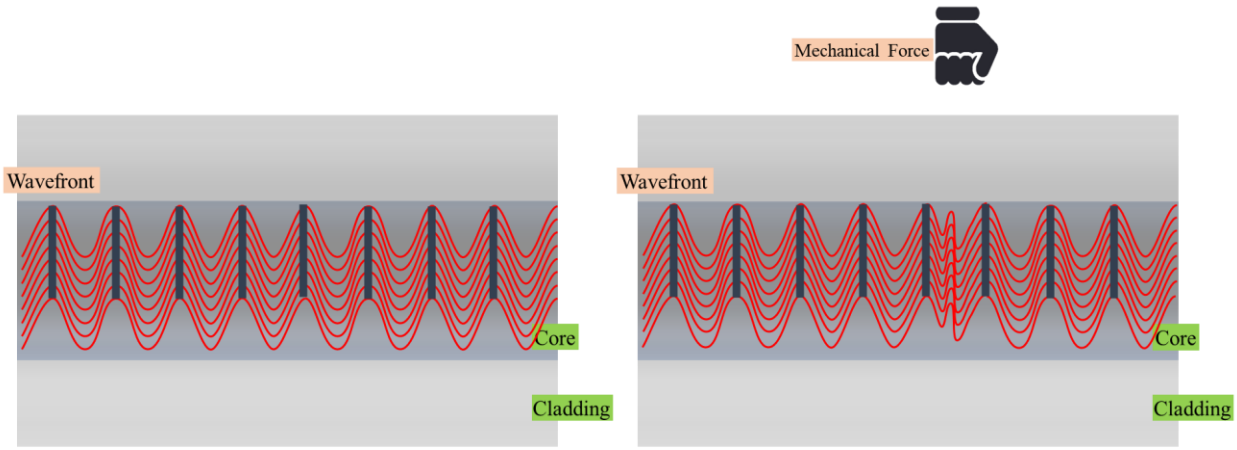


**Figure 23 The schematic of phase change induced by external perturbations**

Within the spectral width of light, the phase of backscattered light at location of scatter can be treated as consistent with incident light since Rayleigh scattering is elastic phenomenon. Hence the backscattering light conveys the information of instantaneous perturbations as well.

Although the narrow linewidth laser provides the feasibility of phase detection, it imposes restriction on sensing length due to short coherent time. The coherent time is in the same order of light linewidth inverse. For example, a common several kHz narrow linewidth laser brings about $10^{-4}s$ coherent time which is 20 $km$ sensing length.

Researchers have put lots of efforts on improvement of accuracy and reliability in φ-OTDR. Since the optical frequency of light is too high to be locked, homodyne and heterodyne

interference provides feasible solutions to extract the phase. Because of square law of photodetector, the intensity of beating signal from interferometer can be expressed as

$$I_0 = E_1^2 + E_2^2 + 2\sqrt{E_1 E_2}\cos\left[(\omega_1 - \omega_2)t + \Delta\varphi\right]. \quad (4\text{-}2)$$

Here $\Delta\varphi$ is the phase difference of two arms in interferometer. If the lights with optical frequency $\omega_1$and $\omega_2$ from two arms are same, the intensity of beating interference is proportional to phase difference. Or keeping their optical frequency difference within the capability of electrical oscillator, the phase difference can also be extracted by using LIA or other indirect methods. Figure 24 shows the light propagation in typical heterodyne and homodyne interference. They rely on certain optical frequency shift or fixed-time delay in one arm of interferometer, respectively.

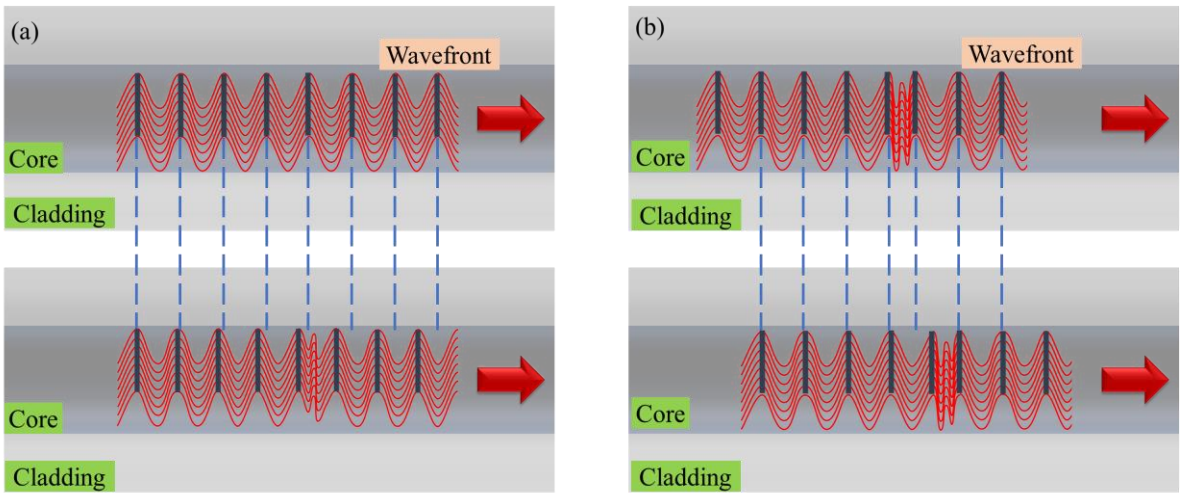


**Figure 24 The schematic of typical interferometry. (a) Heterodyne and (b) homodyne interference of pulsed interrogating light inside the two arms of interferometer.**

In brief, the interference from two lights with same frequency is homodyne while closed frequency is heterodyne. The heterodyne method such as digital coherent input-quadrature [112]

shifts the light frequency in one arm of interferometer to generate low-frequency beating interference. The beating frequency is much lower than light frequency which is in the working range of LIA. Then the phase components at beating frequency can be simply extracted. Figure 25 gives a clear illustration on typical structure of heterodyne method using digital coherent input-quadrature.

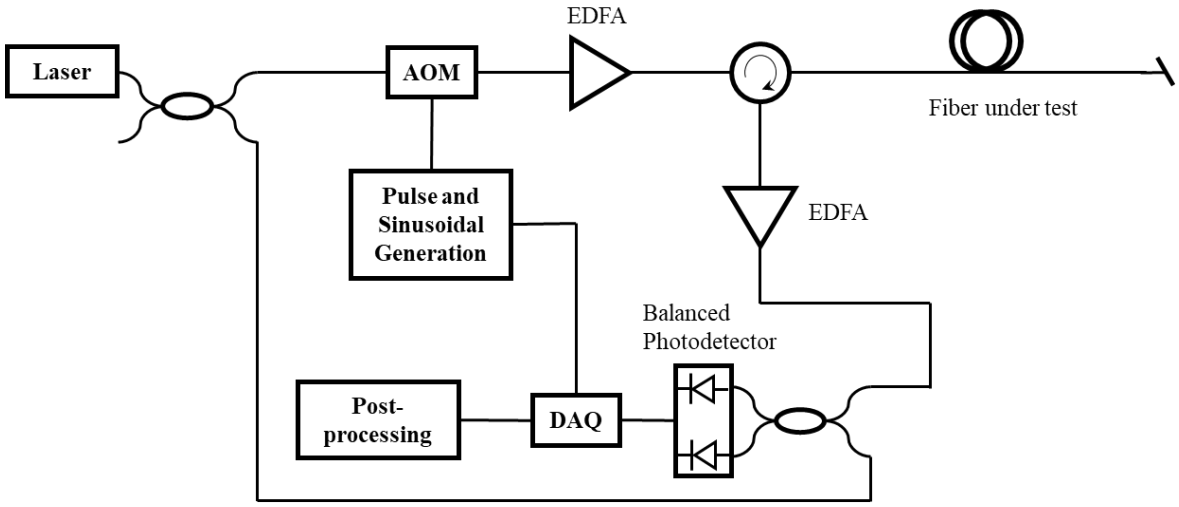


**Figure 25 The schematic of φ-OTDR using demodulation method of digital coherent input-quadrature.**

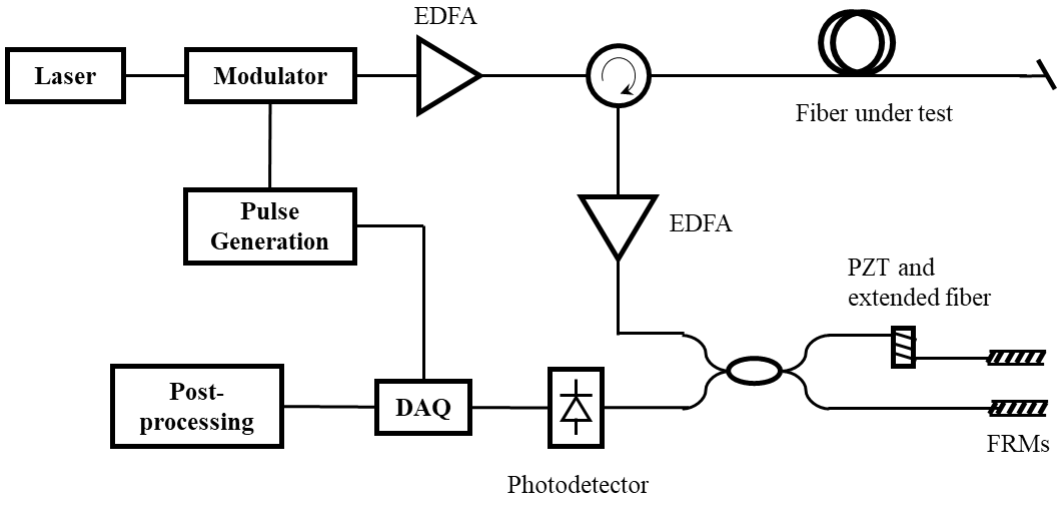


**Figure 26 The schematic of φ-OTDR using demodulation method of phase generated carrier. (FRM: Faraday rotation mirror; PZT: lead zirconate titanate transducer)**

The homodyne method is also applicable that can be achieved by extending the length of one arm in interferometer to create a time delay. Two identical lights within interferometer eliminates the oscillation of optical frequency. And certain time delay only leaves fixed phase difference in addition to perturbation-induced phase variation. However, the phase difference is hard to be extracted since it is in the same order of intensity offset. Phase generated carrier (PGC) [113] is one of the most widely used method as phase extraction shown in Figure 26.

PGC exerts additional piezoelectric transducer in one arm of Michelson interferometer along with extended fiber length [114]. It brings about a sinusoidal amplitude modulation as an external carrier inducing to interferometer. The intensity of interference including fixed time delay and large carrier can be expressed as,

$$I(t) = A + Bcos[Ccos(\omega_c t) + \varphi_s(t) + \varphi_0(t)], \tag{4-3}$$

where $Ccos(\omega_c t)$ contributes to external carrier, $\varphi_s(t)$ is phase difference between two arms and $\varphi_0(t)$ is initial phase difference of system and drift noise. The large carrier brings a low frequency component into interference signal which can be decomposed to several harmonics all carrying the same $\varphi_s(t)$. Through some algorithms like differentiate cross multiply or arctangent, the phase difference $\varphi_s(t)$ between two arms can be extracted.

The use of Faraday rotation mirrors (FRMs) within Michelson interferometer is a common technique to eliminate the polarization-induced fading owning simple and effective configuration [115]. A polarization-insensitive interferometer is very important in PGC scheme to resist polarization shift at carrier generation. It also has positive effects in 3×3 coupler scheme for polarization control. Figure 27 show the schematic of an unbalanced Michelson interferometer consisting of a 3×3 optical fiber coupler and two Faraday rotator mirrors. It bears much similarity

to PGC on extracting phase difference of two arms of interferometer with certain time delay. But it depends on the intrinsic property of 3×3 coupler instead of utilizing large carrier to analyze its harmonic components.

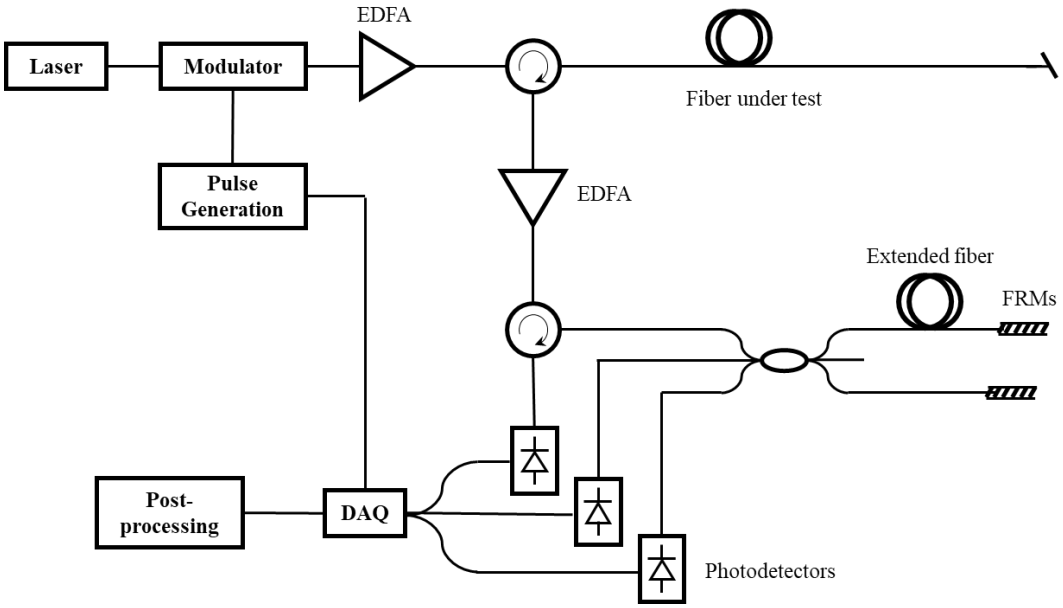


**Figure 27 The schematic of φ-OTDR using demodulation method of 3×3 coupler.**

### 4.3 Phase Extraction in 3×3 Coupler Demodulation

The effectiveness of using 3×3 fused optical fiber coupler for phase demodulation has been studied in various applications [116, 117]. The basis of demodulation stems from hypothesis of ideal symmetric 3×3 coupler that has 120° fixed phase difference between each two arms. As symmetric coupler, three waveguides arranged as equilateral triangle share the same coupling coefficient $k$. The conservation of optical energy principle leads to a simplified description of Jones matrix for 3×3 coupler [118, 119].

$$M_3 = \begin{bmatrix} \frac{e^{2ki}+2e^{-ki}}{3} & \frac{e^{2ki}-e^{-ki}}{3} & \frac{e^{2ki}-e^{-ki}}{3} \\ \frac{e^{2ki}-e^{-ki}}{3} & \frac{e^{2ki}+2e^{-ki}}{3} & \frac{e^{2ki}-e^{-ki}}{3} \\ \frac{e^{2ki}-e^{-ki}}{3} & \frac{e^{2ki}-e^{-ki}}{3} & \frac{e^{2ki}+2e^{-ki}}{3} \end{bmatrix} = \begin{bmatrix} 1 & e^{\frac{2\pi}{3}} & e^{\frac{2\pi}{3}} \\ e^{\frac{2\pi}{3}} & 1 & e^{\frac{2\pi}{3}} \\ e^{\frac{2\pi}{3}} & e^{\frac{2\pi}{3}} & 1 \end{bmatrix}, \quad (4\text{-}4)$$

In the unbalanced Michelson interferometer, fixed-time delay in one arm imposes additional phase shift to transmitting light. Two FRMs reflect the lights back to coupler resulting additional phase shift doubling. The polarization tuning of FRMs are neglected in the simplified model of matrix analysis. By serving as simple mirrors, FRMs keep the properties of transmitting lights within interferometer and only reverse their directions. Two reflected lights are launched into 3×3 coupler that generates the beating interference at three output ports.

$$\begin{aligned} E_{out} = M_3 T_{fiber} M_3 E_{in} &= \begin{bmatrix} 1 & e^{\frac{2\pi}{3}} & e^{\frac{2\pi}{3}} \\ e^{\frac{2\pi}{3}} & 1 & e^{\frac{2\pi}{3}} \\ e^{\frac{2\pi}{3}} & e^{\frac{2\pi}{3}} & 1 \end{bmatrix} \begin{bmatrix} 1 & 0 & 0 \\ 0 & e^{i\phi} & 0 \\ 0 & 0 & 0 \end{bmatrix} \begin{bmatrix} 1 & e^{\frac{2\pi}{3}} & e^{\frac{2\pi}{3}} \\ e^{\frac{2\pi}{3}} & 1 & e^{\frac{2\pi}{3}} \\ e^{\frac{2\pi}{3}} & e^{\frac{2\pi}{3}} & 1 \end{bmatrix} \begin{bmatrix} E_{in} \\ 0 \\ 0 \end{bmatrix} \\ &= \begin{bmatrix} 1 + e^{i(\phi + \frac{4\pi}{3})} \\ e^{\frac{2\pi}{3}}(1 + e^{i\phi}) \\ e^{\frac{2\pi}{3}}(1 + e^{i(\phi + \frac{2\pi}{3})}) \end{bmatrix} E_{in} \end{aligned} \quad (4\text{-}5)$$

The measured intensities from three output ports of 3×3 coupler can be calculated as,

$$\begin{bmatrix} I_{out1} \\ I_{out2} \\ I_{out3} \end{bmatrix} = \begin{bmatrix} E_{out1}E_{out1}^* \\ E_{out2}E_{out2}^* \\ E_{out3}E_{out3}^* \end{bmatrix} \propto \begin{bmatrix} 1 + \cos\left(\phi - \frac{2}{3}\pi\right) \\ 1 + \cos(\phi) \\ 1 + \cos\left(\phi + \frac{2}{3}\pi\right) \end{bmatrix}, \quad (4\text{-}6)$$

Two different demodulation schemes were reported to extract the phase $\phi$ from measured intensities. They were known as Naval Research Laboratory (NRL) method and Naval Postgraduate School (NPS) method [120]. NRL randomly picked two measured intensities as input into the integrated operation of differential cross-multiplying demodulator [121]. By eliminating the direct current (DC) offset, the voltage output of demodulator was purely proportional to the phase $\phi$. The DC bias was preset with predicted value might not to be properly accurate. It brought about an additional oscillation as $sin\phi$ giving rise to signal distortion.

NPS improved the reliability by utilizing all three output symmetrically [122]. The basis of demodulator design to eliminate the DC bias and extract the phase information arose from two trigonometric identities,

$$\sum_{n=1}^{3} \cos\left[\phi - (n-1)\frac{2}{3}\pi\right] = 0, \qquad \sum_{n=1}^{3} \cos^2\left[\phi - (n-1)\frac{2}{3}\pi\right] = \frac{3}{2}, \tag{4-7}$$

Instead of presetting DC bias, the two trigonometric identities provide a viable way to cancel the offset automatically. The phase can be extracted through an integrated operation including differential and integral as an analog processing algorithm. Hence, the output of NPS demodulator can be expressed as,

$$V(t) = \frac{\sqrt{3}A_D A_3 A_R}{A_2}\phi(t), \tag{4-8}$$

where$A_2$, $A_3$, $A_R$ and $A_D$ are gain of second adder, third adder, differentiator and divider in the algorithm respectively. The quantity of the transient phase is directly proportional to the output of the deterministic demodulator.

In high-speed dynamic strain measurement, the maximum detectable frequency was determined by repetition rate of interrogating pulsed light. Sending the next pulse into fiber under test should wait for receiving all of backscattered lights from the last one, which depends upon the interrogating length. That puts a restriction on upper limit of detectable frequency range.

$$f < \frac{v_g}{2L}, \tag{4-9}$$

where $v_g$ is the group velocity of light transmitting in optical fiber, and $L$ is the length of fiber under test. Typically, the upper limit of detectable frequency range was set to 1 MHz when interrogating at most 100 meters optical fiber.

## 4.4 System Design

Using symmetric 3×3 coupler of unbalanced Michelson interferometer along with NPS demodulation is viable to detect dynamic strain throughout entire fiber. Phase changes induced by external stress can be captured and demodulated. However, telecom grade optical fibers have an intrinsically weak Rayleigh scattering profile that severely limits SNR in strain sensing. The deficiency of SNR decreases the accuracy of phase demodulation. Nano-reflectors written by ultrafast laser provides an accessible solution to enhance SNR of φ-OTDR. The Rayleigh enhanced region can be a single point or a segment of fiber. All of parameters of nano-reflectors regarding

strength, location, and section length are controllable in fabrication process. Figure 28 shows different Rayleigh profiles of 9 nano-reflectors along 30 meters long optical fiber, interrogated by commercial OBR. Each nano-reflector was estimated to be 2×2-μm (Cross-section) by 7-μm (Length) while kept 3 meters interval.

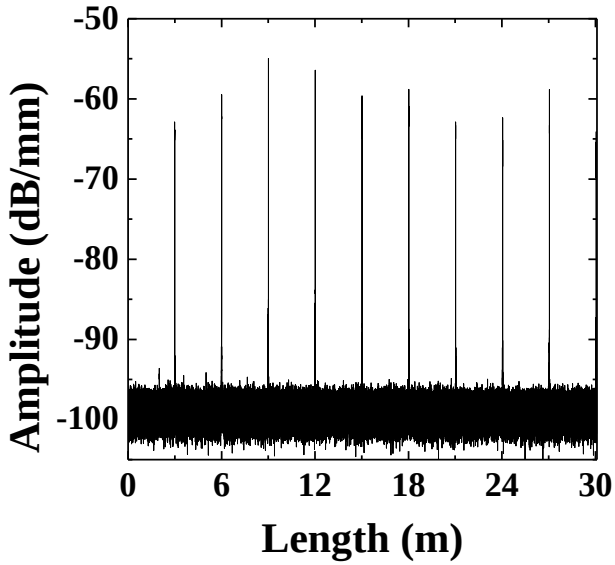


**Figure 28 Rayleigh profiles of 9 nano-reflectors with 3 meters interval.**

Focusing femtosecond laser into small point at optical fiber induced over 35 dB enhancement of Rayleigh backscattering. Through roll-to-roll setup, the fabrication of nano-reflectors has great potential into mass production. When infinite number of nano-reflectors were written throughout entire optical fiber, they can be utilized to construct successive homodyne interferences with superb SNR to reveal the phase information. The system tactfully designed to extract phase within homodyne interferences from enormous nano-reflectors was described in Figure 29.

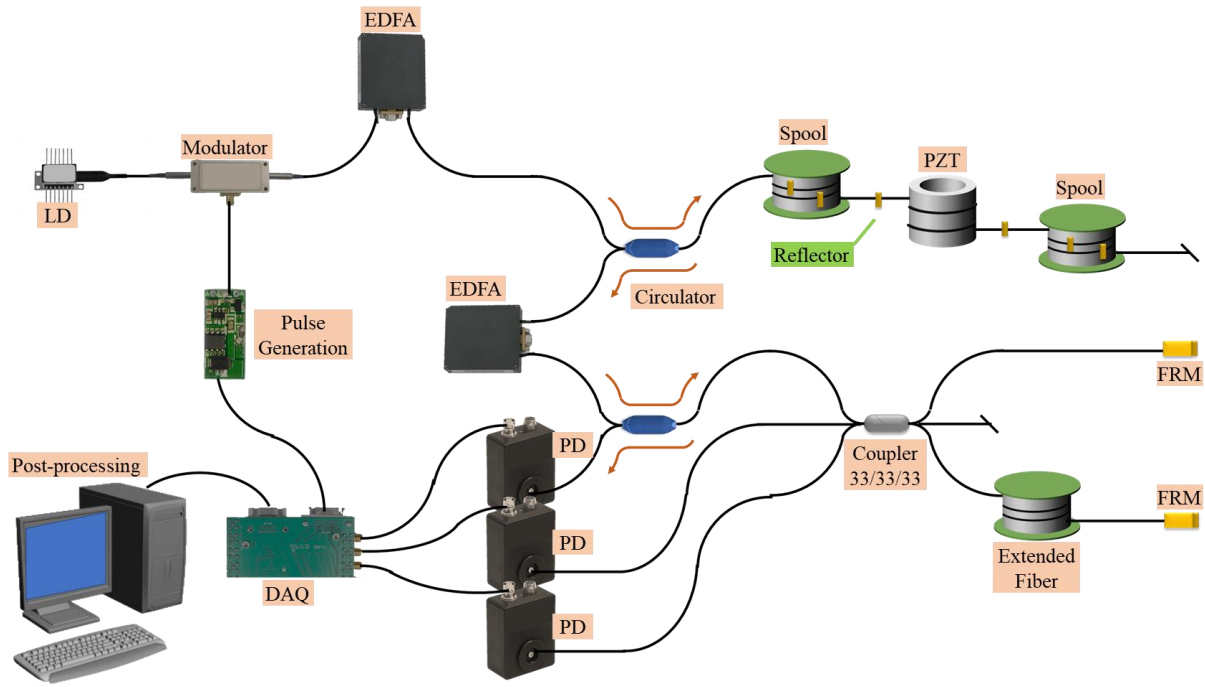


**Figure 29 Schematic diagram of the homodyne φ-OTDR inscribed with nano-reflectors.**

A single wavelength 1550.12 nm light from a 6 kHz narrow linewidth laser (NKT Basik C15) was modulated to generate 10 ns pulses with a 66 kHz repetition rate by using a semiconductor optical amplifier (SOA, Thorlabs, SOA1013SXS). The pulsed lights were amplified by an Erbium-doped fiber amplifier to reach 150-nJ/pulse (10 mW output power) and launched into the single mode fiber inscribed with nano-reflectors. The backscattered lights from the sensing fiber returned to an unbalanced Michelson interferometer (MI) consisting of 3×3 coupler and two FRMs. A section of extended optical fiber was used to produce fixed-time delay in one arm of MI. Two parted backscattered lights from 3×3 coupler reencountered each other after FRM reflection that generated homodyne interference.

The entire fiber under test kept generating Rayleigh backscattering when interrogating pulses travelled through it. Relatively strong reflectance of nano-reflectors rendered sudden increase of intensity to form successive short pulses within backscattering. These short pulses

presented transient status of interrogating light when passing specific nano-reflectors. Figure 30 shows the illustration of short pulses within Rayleigh backscattering from nano-reflectors.

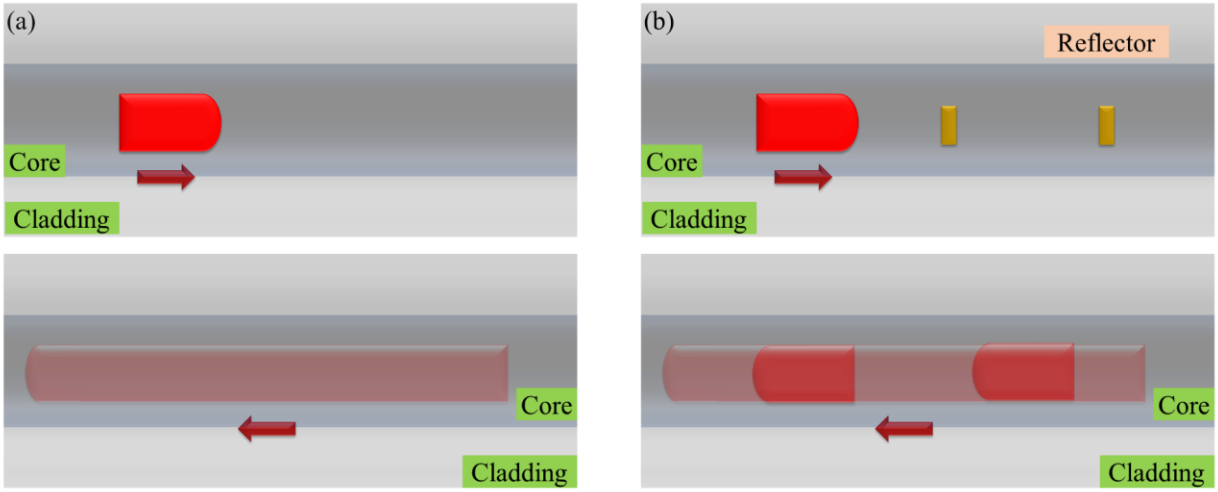


**Figure 30 The illustration of pulsed light propagation in optical fiber to produce Rayleigh backscattering. (a) Normal Rayleigh backscattering interrogated by pulsed light. (b) Short pulses within Rayleigh backscattering from nano-reflectors.**

If the length of extended fiber in MI exactly matched the spatial interval of nano-reflectors, short pulses from adjacent nano-reflectors were overlapped to become prominent throbbing. Figure 31 shows the diagram of homodyne interference generated in MI. Proper time delay caused the interference of short pulses from adjacent nano-reflectors.

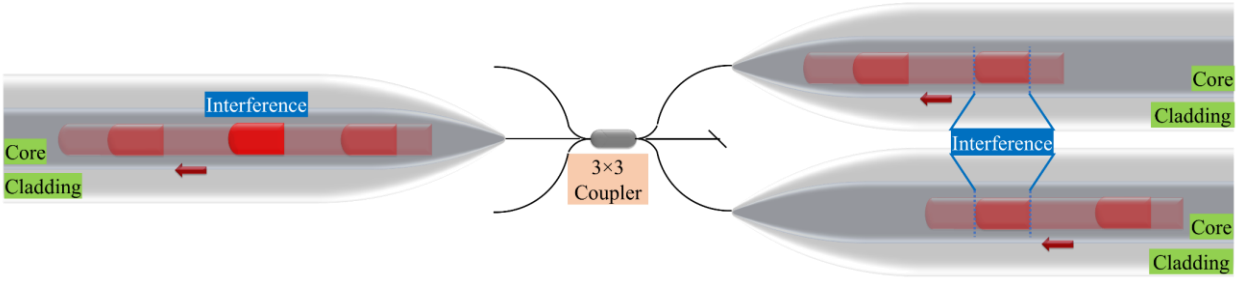


**Figure 31 The interference of short pulses from adjacent nano-reflectors with higher intensity.**

The interference of short pulses from adjacent nano-reflectors implied the transient phase shift occurring between them. Unlike the typical unbalanced MI, 3×3 coupler has three outputs with 120° fixed phase difference which can be used for phase demodulation by using NPS method. Hence, those short pulses from nano-reflectors were able to be monitored and processed to extract the quantitative phase shift in real-time.

## 5.0 Pattern Recognition in Distributed Ultrasound Sensing

Ultrasound interrogation and structural health monitoring technology has found a wide array of applications in heath cares, aerospace industry, autonomous driving, and energy infrastructure monitoring. The acoustic signals within broad frequency range can be used to recognize detailed perturbations occurring around transducer. These perturbations may come from external threats such as malicious intrusion, tempering attempts, illegal tapping, construction accidents, and natural disasters, as well as from internal structural degradation, like corrosion/erosions, due to aging and wear from weather.

A unique trait of fiber optical sensors is their capability to perform distributed strain measurement across very long distance by using telecom fiber [123]. Large-scale facilities and critical infrastructures are required to be monitored and inspected for the purpose of perimeter security and structural health diagnosis. Fiber-based distributed acoustic sensing become a far more appealing technical approach that can perform dual functions, both defending against external threats and performing active measurements to monitor the structural degradation.

However, the performance of system is limited on the aspects of low SNR, slow interrogation and complex pattern recognition. So far, the proposed event recognition can only distinguish significant difference within low-frequency acoustic patterns, such as comparing safe excavator operations and accidental contact to a pipeline [63]. In order to detect the subtle structural defects or minor hidden threat, a reliable distributed ultrasound sensor is desired with enhanced SNR and efficient PR.

## 5.1 Pipeline Protection

Oil, gas, petro-chemical, and energy industries employ pipelines to deliver flammable or explosive material from source to ultimate consumers. Millions of miles pipelines around whole nation demand enormous expenditures in maintenance of structural deficiency. Various corrosions happen across long-distance pipeline either on the internal/ external surface or at the joint of two metal components. And a great diversity of intentional intrusion, construction accident and natural disaster threaten the safety of pipeline all the time. As key infrastructures, these pipelines are important to national security and economic vitality. It is important to develop a comprehensive monitoring scheme to protect the integrity of the pipeline networks.

For perimeter security, conventional surveillance system based on imaging sensors has large installation cost especially in extensive deployment at desolate and harsh environment. The limited information within the line-of-sight is also incapable of accessing pipes buried underground and prewarning the potential threats. The long-distance underground pipes certainly cause protection dilemma that are difficult to be reached. For a very long time, visual or ultrasonic assessment after excavation of pipes has been desirable for damage detection and identification. However, it becomes more and more unaffordable and impractical along with a substantial growth of pipeline networks. A fully in-line non-destructive tool is needed which allows pipes to be inspected and repaired at early stage of cracks.

Permanently installed guided acoustic wave sensors currently have been reported and tested in industry that can reliably detect and size local defects. [124] With over 50-meter detection range of each sensor, the whole pipeline can be covered and remotely screened. [125] Although they have promising results on monitoring simple structures such as straight pipes and pulled bends, their abilities are limited due to overlapping of echoes and discontinuity of acoustic wave

when the complexities of structure extend to tees, welding elbow and diameter changes. [126] It's unsuccessful to delineate or distinguish tangled echoes reflected by corrosions or benign welds. Some unwanted modes and imperfect direction control also strongly affect the reliability of detection as background noise. [127] And a large number of sensors to be deployed in long-distance pipeline surely increase the complication of system and difficulty of signal processing.

Distributed optical fiber sensors are considered promising candidates for pipeline monitoring. Fiber Bragg gratings array [128], OTDR [129], and φ-OTDR [130, 131] have been reported in either leakage detection or pipeline security. They achieved nonintrusive characterization of intrusions or defects by listening to intrinsic acoustic echoes or extrinsic acoustic perturbations. φ-OTDR based on Rayleigh scattering is known as a fully distributed sensor for long-distance and high-sensitivity detection without the drawback of interrogation speed limit [60]. For various applications, strain-dependent Rayleigh backscattering along optical fibers has been a leading approach to perform DAS. Using φ-OTDR, distributed vibration measurement with bandwidth up to 80 kHz across a 5-km long optical fiber was reported [132]. Fast dynamic measurement promises wide detectable frequency range that can harness transient ultrasonic waveforms [47]. Adequate frequency features aided the improvement of recognition accuracy.

### 5.1.1 Experimental Setup

The Rayleigh enhanced φ-OTDR can be a good fit for perimeter security and structural inspection of pipeline networks. φ-OTDR with over 35 dB enhancement of Rayleigh backscattering has showed a great potential on dynamic strain measurement. Since the presence of sharp bending is the top concern in guided acoustic pipeline inspection, two iron pipes connected

by a 90-degree iron elbow was designed to be interrogated with Rayleigh enhanced φ-OTDR. Figure 32 shows the schematic of Rayleigh enhanced φ-OTDR for pipeline protection.

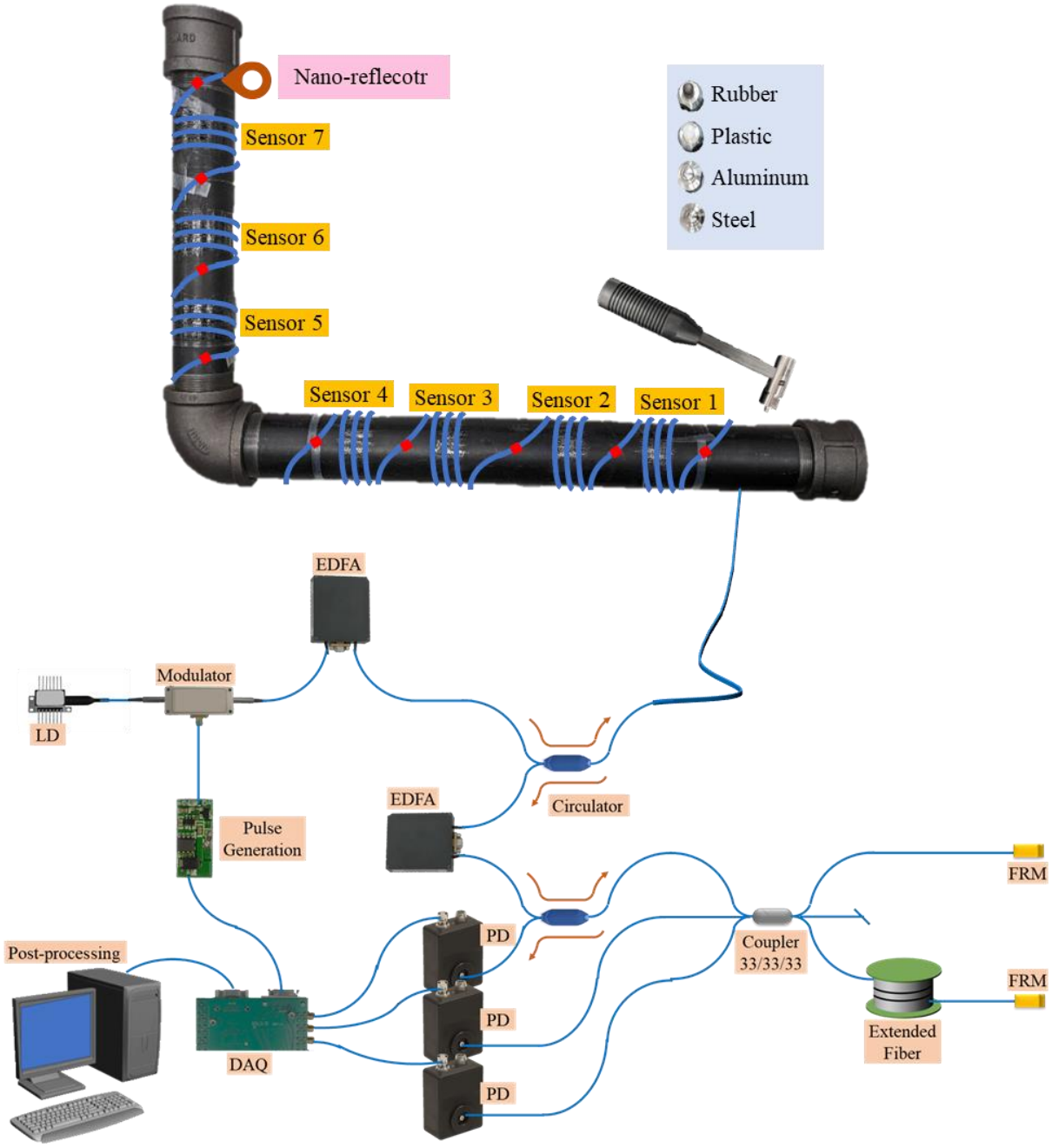


**Figure 32 Schematic diagram of Rayleigh enhanced φ-OTDR for pipeline protection.**

The pipes were 3 inches inner diameter with 0.5 inches wall thickness. Two straight sections of total 5-feet long tightly screwed by a 90-degree iron elbow. Nine nano-reflectors were inscribed along 30-meter standard telecom fiber with interval of 3 meters. They formed 7 ultrasound sensors which were wrapped around two iron pipes. Three photodetectors simultaneously kept monitoring the Rayleigh backscattering from the optical fiber by using high-speed data acquisition. Nano-reflectors within fiber core contributed on enhancement of SNR illustrated in the Figure 33. The intensity peaks of backscattering arise from the relative strong reflectance of nano-reflectors.

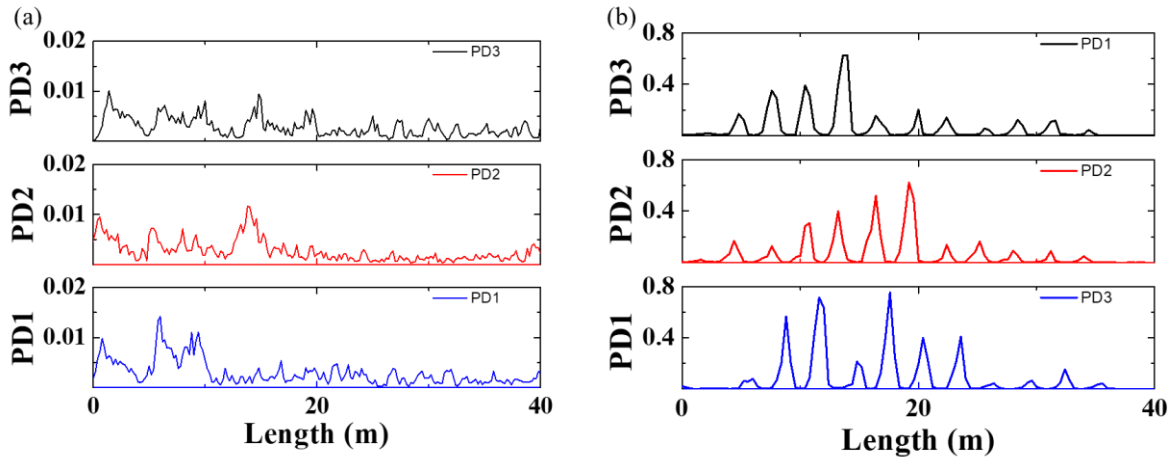


**Figure 33 Rayleigh backscattering detected by three photodetectors by interrogating a section of optical fiber (a) without Rayleigh enhancement, or (b) owning nine nano-reflectors.**

The interrogating pulse was set to be 10 nanoseconds with 66 kHz repetition rate, which brought 33 kHz frequency bandwidth for the ultrasound detection. The ultrasonic signals were recorded continuedly into 0.3 seconds segments. Large volume of acoustic signals was simultaneously harnessed by 7 sensors and launched into signal processing. Vast datasets with distinct features were waiting to be identified by a versatile analytics tool.

### 5.1.2 Perimeter Security

Important infrastructure had a great risk facing structure damage when encountered intentional or accidental contacts from external threats. Evaluating risk levels of forthcoming threat is the basis to enact the proper treatment. A specialized hammer had several heads made of four different materials, including soft rubber, hard plastic, aluminum, and steel.

These various hammer heads were used to generate acoustic waves with different frequency characteristics that mimic different external impacts to pipelines. Soft rubber and hard plastic hammer heads were used to simulated low frequency acoustic signals similar to striking on insulation and protective layers. And aluminum and steel hammer heads were tried to take the direct contact between pipes and metal tools into account. Figure 34 show the transient wave form produced by four hammer heads and captured by seven sensors when tapping the hammer at one end of pipe. Both time-domain and frequency-domain were illustrated for comparison.

Seven sensors simultaneously monitored the transient acoustic wave from hammer single-tapping. Due to the presence of 90-degree iron elbow, overlapping echoes and disturbance of acoustic waves occurred as the forms of forward propagation and backward scattering. They become frequency-dependent attenuation or reflection shown in the spectral analysis. Most acoustic energy from aluminum and steel hammer heads located at relatively high frequencies between 1.5 kHz and 2 kHz. The high-frequency components faded away quickly when passing through the elbow. Soft rubber offers the lowest frequency and weakest intensity among the four kinds of materials. But its low-frequency components propagated well through whole structure. This frequency-dependent attenuation was well-depicted in the acoustic signals from hard-plastic hammer head. The high-frequency components dissipated in forward propagation and did not have enough amplitude to cross the elbow. Low-frequency components of acoustic signals below 500

Hz can pass the elbow without significant attenuation. Based on this low-pass filtering effects of iron elbow, four types of acoustic events from various hammer heads showed relatively distinct features that contributed to the classification.

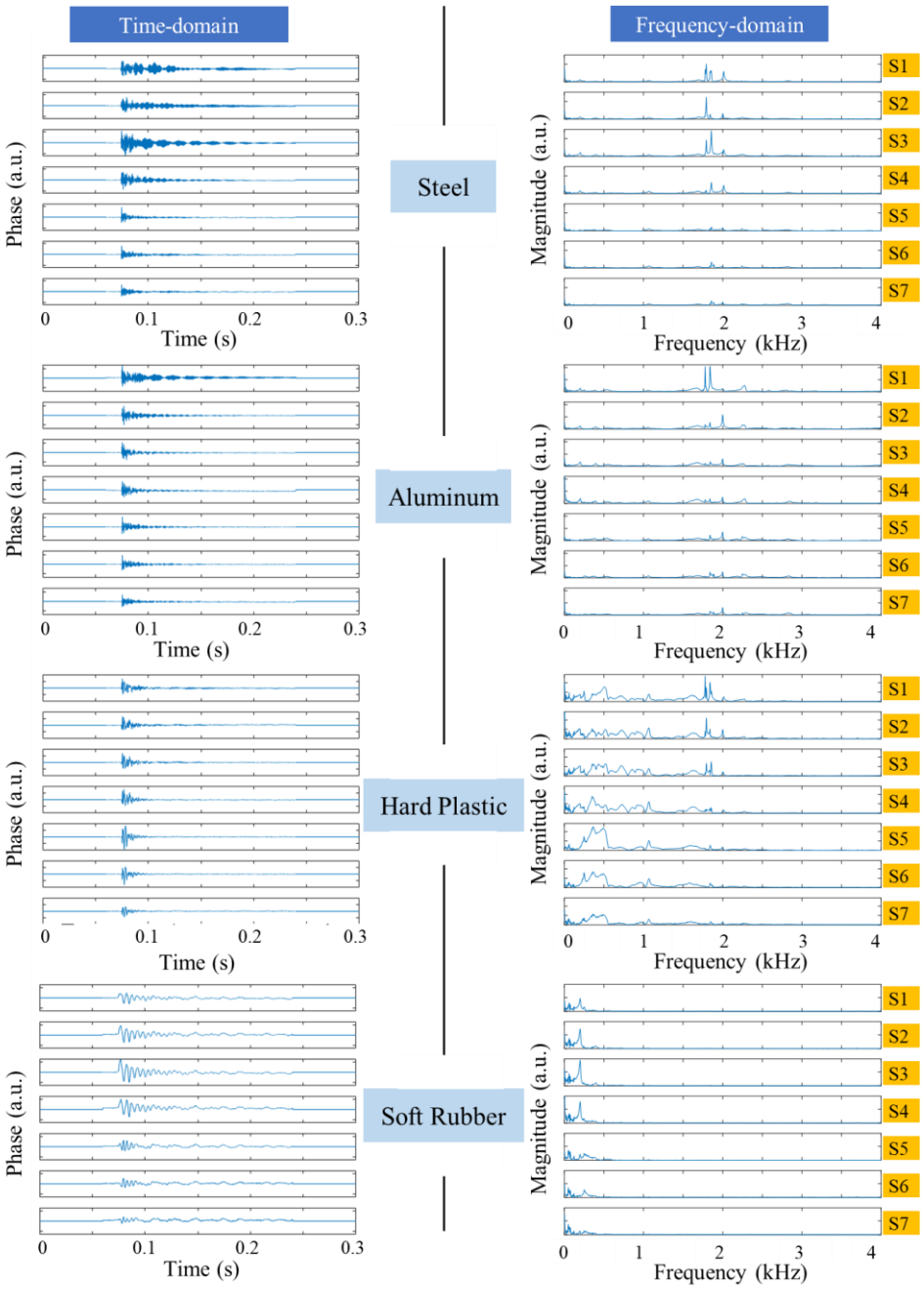


**Figure 34 The time-domain and frequency-domain acoustic waveforms from 7 sensors (S1-S7) by single tapping with steel, aluminum, hard plastic and soft rubber hammer heads.**

### 5.1.3 Structural Health

Instead of prewarning the potential threats striking to the surface of pipeline, discovering existing structural defects caused by aging and weathering was the top concern in pipeline inspection. Corrosion or erosion occurring at inner surface was hard to be reached and inspected. Especially when facing the sharp bending to impede the travelling acoustic wave, abnormal echoes mislead the guided acoustic wave interrogation to generate erroneous judgement.

Wrapping the fiber covering the whole pipeline promised to receive both forward propagation and backward scattering of acoustic wave. It has overwhelming advantage for pipe inspection especially near sharp bending. Electrical transducers might face the problem of insufficient magnitude or tangled acoustic echoes for inspection of complex structure. The high spatial resolution data harnessed by distributed fiber sensors can detect both forward propagation and back-scattered acoustic signal as it passes through the elbow. Given the weak intensity of backscattered acoustic wave, forward propagating guided acoustic wave can offer additional information for defect detection and classification.

Since sharp bending was inevitable problem for conventional ultrasonic interrogation, seven installation scenarios have been designed to mimic various corrosions at 90-degree iron elbow, like flow-accelerated corrosions and galvanic corrosions. Figure 35/36 show the time-domain and frequency-domain acoustic signal acquired in seven installation scenarios.

Sharp bending was susceptible to flow-accelerated corrosion induced by turbulent flows. And loose connection between two components leaded to galvanic corrosion at the joint of sharp bending. Seven installation scenarios have been designed to mimic these corrosions, including four types of simulated pitting defects on inner surface (Case 1–4), pipe insulation failure causing

external corrosion (Case 5) and galvanic corrosion at the joint of two metal components (Case 6), comparing with pipe structure without defect (Case 7).

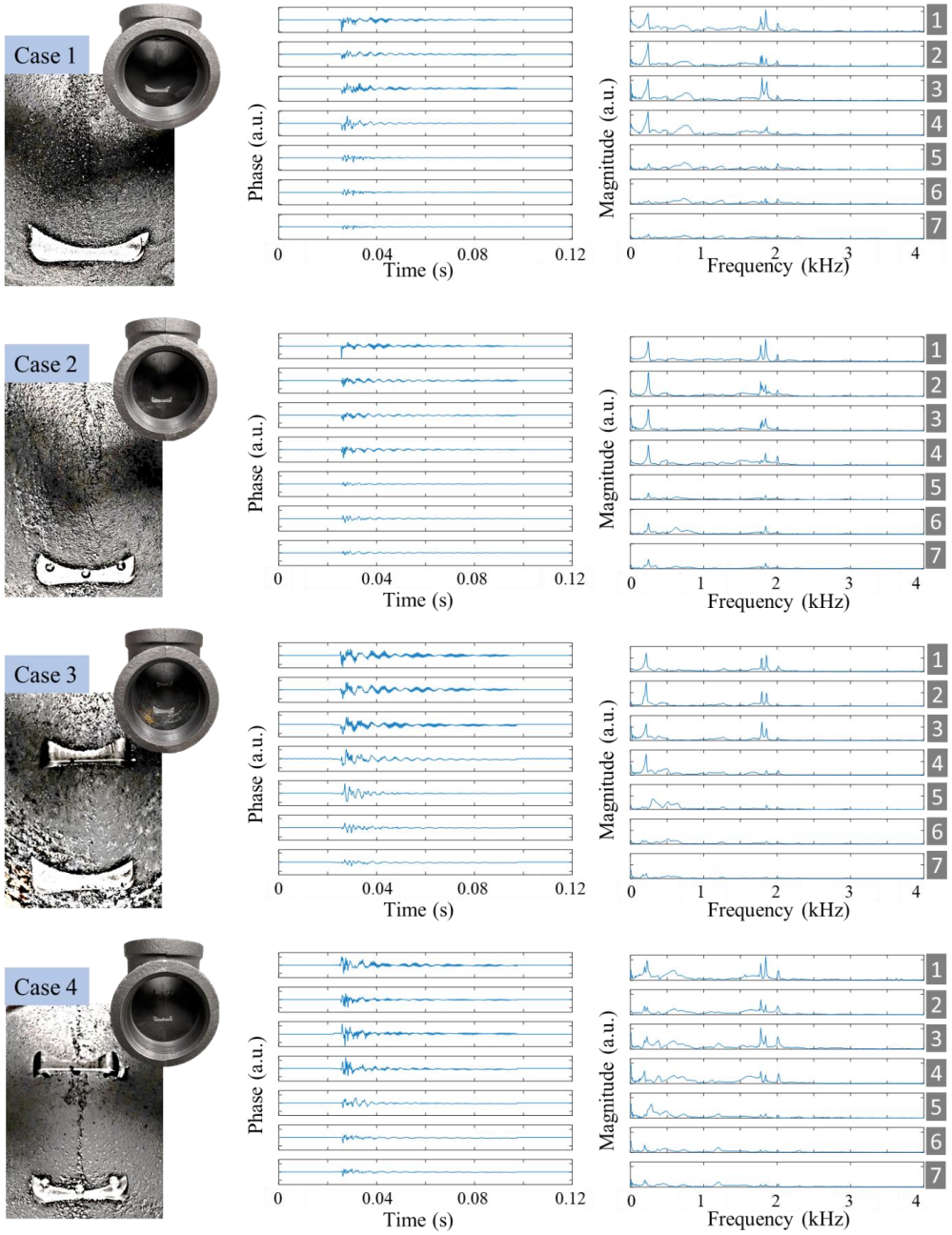


**Figure 35 Four installation scenarios and their waveforms at time-domain and frequency-domain by single taping with a hard-plastic hammer. Case 1: One cutting groove; Case 2: One cutting groove with three drilling holes; Case 3: Two cutting grooves; Case 4: Two cutting grooves, six drilling holes.**

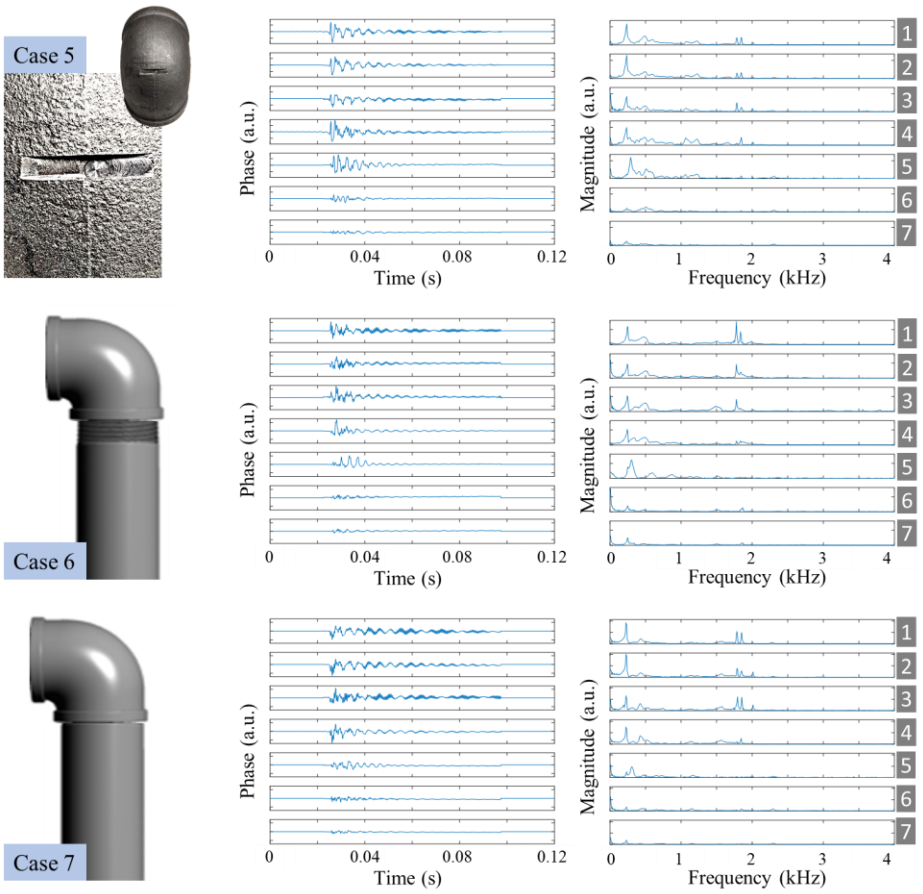


**Figure 36 Another three installation scenarios: Case 5: One trench at external surface; Case 6: loose connection; Case 7: normal connection.**

The trench and grooves were set to be 1.5 in. (length) × 0.25 in. (width) × 0.08 in. (depth). And holes were 0.125 in. (diameter) ×0.2 in. (depth). Acoustic excitation was chosen to be hard plastic hammer due to aforementioned study. The spectral characteristics of acoustic excitation with hard plastic hammer showed multiple frequency components covering broad bandwidth. It also provided sufficient signal intensity to pass through the iron elbow owning significant attenuation. With the help of 66 kHz sampling rate, adequate frequency features were captured and recorded on all scenarios.

## 5.2 Pattern Recognition

Sound generated by excavators at nearby construction sites are different from those produced by intentional sabotage of pipeline, which produce high pitch noise due to metal contacts. On the contrary, various corrosions inside pipeline owned subtle difference due to their small dimension and minor damage at early stage. The distinct or similar features hiding in enormous volume of acoustic dataset demanded versatile data analytics tool for event identification and feature classifications. Filtering out the pertinent information was inapplicable to cover a great diversity of events from external intrusion to internal inspection.

Machine learning approach could potentially handle the large amount of data and unveil various patterns associated with both external threats and pipeline corrosions. As a revolutionary solution for pattern recognition, machine learning has undergone substantial development over the past few decades. It has been extensively studied due to the increased availability of big data and abundance of processing power.

As most common subbranch of machine learning, supervised learning algorithm infers a function from labeled training data. It is well-known in pattern recognition to predict the correct label for newly presented input data. Shallow non-convolutional neural networks owning only one hidden layer of neurons has simplest structure among all supervised learning algorithm. It is easy to implement with low computation burdens and has theoretical capacity of approximating any continuous function on a compact domain.

The distinct extrinsic acoustic events from four different hammer heads subjected to simple correlation between them. The shallow non-convolutional neural networks had a desired trait to handle the acoustic signals featuring great diversity. The architectures of the shallow neural network used in this work are shown in Figure 37.

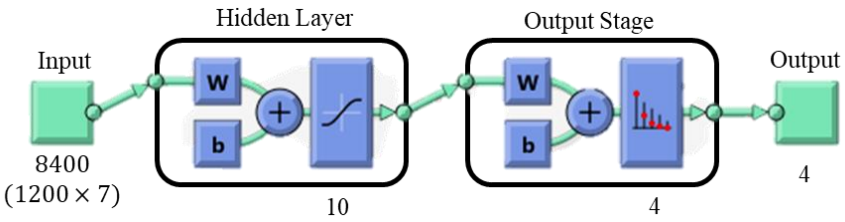


**Figure 37 Architectures of shallow non-convolutional neural network.**

In the data of each trial harnessed from seven sensors, the first 1200 frequency components (DC to 4 kHz) were used as input to the shallow neural network. After integrating the acoustic signals from seven sensors into an input vector consisting of 8400 elements (1200×7), they were labeled and sent into shallow neural network for training. The hidden layer within shallow neural network contained 10 neurons and was attached by a softmax output layer for classification among 4 possible events.

The nonlinear complexity within the acoustic data degraded the effectiveness of single hidden layer shallow neural networks. Deep neural networks often outperform it on the account of multiple hidden layers. Each layer extracts features of different levels from the input data. These levels can take an example as an image that subject to edges, corners, and intensity gradients as basic features; shapes and objects as intermediate level; object combination or arrangement specific to the application as high-class. Abundant features of various levels provide lots of accessible parameters to fully describe the function for classification.

Convolutional neural networks (CNNs) are a popular deep neural network structure in the analysis of image pattern. By using series of convolution and pooling operations to reduce the number of parameters, CNNs are especially successful in processing large-size inputs with spatial invariance.

CNNs were also applied on classification of extrinsic acoustic events to explore the nonlinearity of acoustic data. Figure 38 shows architectures of CNNs that processed 1200 (frequency)×7(sensors) as input matrix. Three convolution layers are applied including 2×3 or 3×3 convolutional filters and 2×2 max pooling. Rectified Linear Unit gradually decreased the size of image and increased the number of extracted features. A fully connected softmax layer was attached at the end resulting 4 types of output.

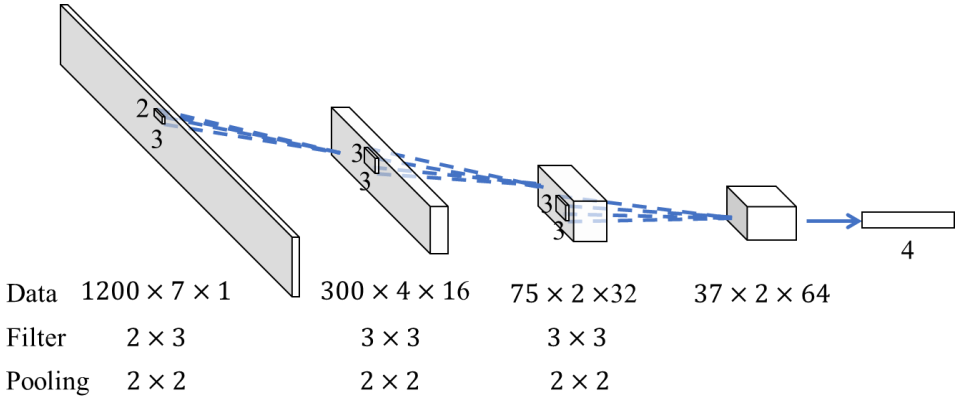


**Figure 38 Architectures of convolutional neural network.**

The acoustic data from single-tapping with four kinds of hammer heads were labelled into four difference classes. Using each type of hammer performed seventeen sets of trial that were randomly divided to 12 and 5 for training and testing respectively. Each classification was run 10 times to determine uncertainty of data selection and obtain the range of accuracy. Instead of using average and standard deviation, the range of accuracy clearly showed the capability of machine learnings for event recognition, since the lower limit is equivalent to false rate of system. The accuracy to classify those four classes was show in Table 1 including the use of shallow non-convolutional neural network and CNN. Slightly better performance of CNN comparing with

shallow non-convolutional neural network presents certain nonlinearity existed in acoustic signals. CNN have better competence to make more accurate estimate based on its multiple hidden layers.

**Table 1 Classification result of four types of extrinsic acoustic sources by using shallow non-convolutional neural network and CNN.**

| Material | Dataset | Shallow Neural Network | CNN |
|---|---|---|---|
| Rubber | 17 | 80%−100% | 85%−100% |
| Plastic | 17 | | |
| Aluminum | 17 | | |
| Steel | 17 | | |

Machine learning provides a revolutionary solution for events recognition not only relied on supervised learning algorithm. Unsupervised learning aims at finding relations inside the data themselves without burdensome and tedious labelling. Given large diversity in shape and size of defects, it is inapplicable to find an all-round function covering all scenarios. The algorithm better to have adaptive potential to train itself without manually labelling. The latent features within the data should be characterized and clustered leading to accurate classification.

Self-organizing map (SOM) and autoencoder are two famous unsupervised neural networks to decompose the latent features into a rich class of resulting clusters. Their performance on analyzing acoustic signals from distributed fiber sensors were investigated for comparison. It provided an intuitive insight of different models affecting classification of corrosion with subtle difference.

SOM employs neuromorphic principles to sensitize neighboring neurons to similar inputs with much faster training speed. The neurons in a SOM are generally placed on a grid with well-defined distance between any two of them. During the training phase, their weights are randomly

initialized. For each input sample, the SOM picks the neuron owning whose closest weight to the input data as the best matching unit (BMU). The weight of each neuron is updated following the distance approaching to input data. The closer to the BMU a neuron is in tantamount to more significant the update on its weight. Simply put, the update of neuron $i$'s weight is given by:

$$w_i' = w_i + \alpha\big(d(i, \mathrm{BMU})\big)(x - w_i), \tag{5-1}$$

where $x$ is the input data, $d$ is the distance between neuron $i$ and the BMU, and $\alpha$ is a decreasing function of $d$, which can be a Gaussian function.

SOM was trained by unlabeled data to form the neurons as BMU. A trained SOM can be naturally used as a classification network to categorize the input data to various clusters. Figure 39(a) show the architectures of SOM used in corrosion classification. Similar to shallow neural network, first 1200 spectral components from seven acoustic sensors were stacked together to form vector inputs consisting of 8400 elements. Seven types of known condition made the SOM topology as a 3D grid of size 2×2×2. It brought 8 closely located neurons within SOM algorithm.

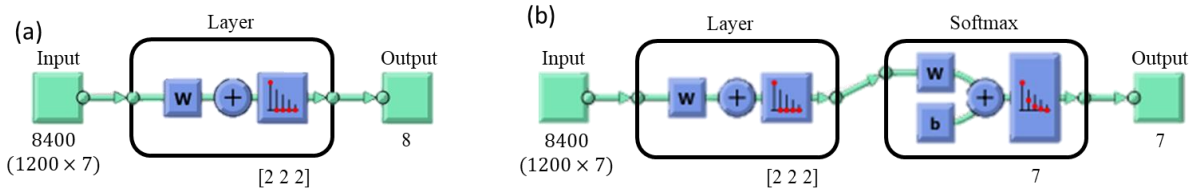


**Figure 39 The schematic of self-organizing map to be explored in event recognition. (a) Architectures of self-organizing map. (b) Self-organizing map attached with softmax layer at output stage.**

Instead of labeling the input data into several categories, all of unlabeled dataset were sent into SOM for training purpose. But a trained SOM outputted unlabeled clusters that was hard to

be interpreted and identified in association with actual defects. Manually link the unidentifiable output to actual scenario was required for evaluation.

Another convenient approach was to investigate the relation between unlabeled results and defect types through training a softmax layer attached at the output stage. This small-scale supervised layer can easily learn the association between the actual defect and the features which determine the cluster assignment. Figure 39(b) show the architectures of SOM attached with a softmax layer.

Autoencoder implemented a different strategy on unsupervised learning. Similar to common data compression processes, the autoencoder aims at minimizing the distortion when compressing the data into the feature space. Figure 40 show the architectures of autoencoder consisting of two neural networks.

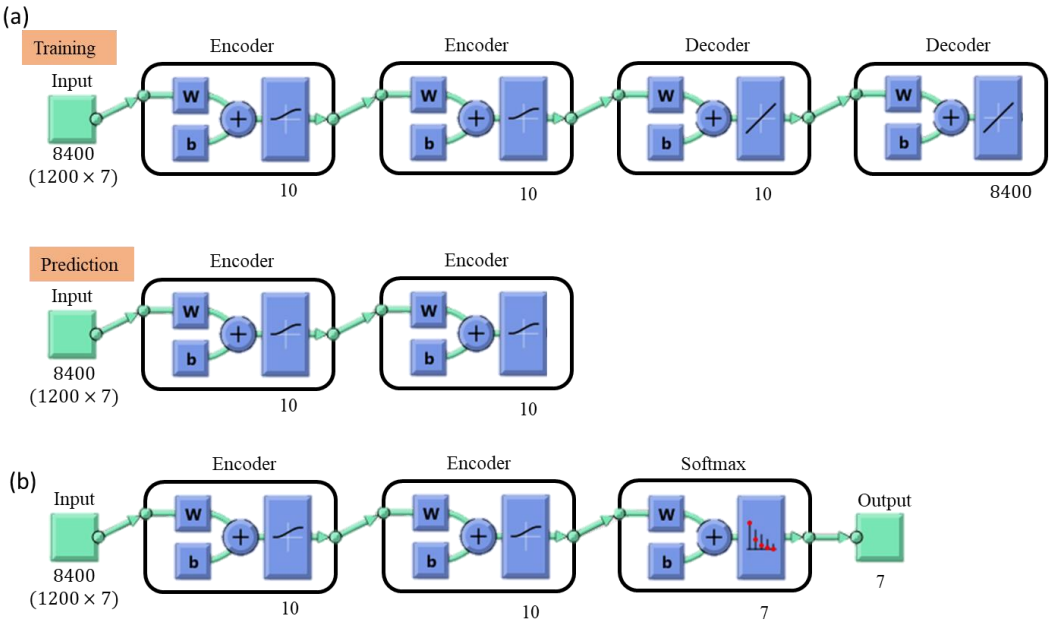


**Figure 40 The schematic of autoencoder to be explored in event recognition. (a) Architectures of autoencoder. (b) Autoencoder with softmax layer at output stage.**

The input signals at data space is firstly matched to feature space ($F: \mathbb{R}^n \rightarrow \mathbb{R}^m$) by using encoder network. The transformed data within feature space is projected back to data space ($G: \mathbb{R}^m \rightarrow \mathbb{R}^n$) with decoder network. The difference between the original data and the decompressed data is minimized through gradient-based back propagation. The algorithm of autoencoder can be expressed as solving an equation ($X \in \mathbb{R}^{k \times n}$) of

$$\min_{F,G} \left\| G\big(F(x)\big) - x \right\|, \tag{5-2}$$

where $k$ is the number of given input samples. The encoder output $F(x)$ directly indicates the classification of sample $x$ which is known as sparse autoencoder. A regularization term is added in the loss function to make sure the features are uniquely presented in each sample. As usually $m \ll n$, the large size data can be represented by a few crucial features. Doubling the autoencoders as two cascades can accelerate the learning giving rise to improvement of the classification accuracy.

**Table 2 Classification result of seven installation scenarios by single tapping with hard plastic hammer.**

| Scenario | Data | Shallow | CNN | SOM | SOM +Softmax | Auto-encoder | Autoencoder +Softmax | SOM +Softmax |
|---|---|---|---|---|---|---|---|---|
| Normal | 17 | 97.1%–100% | 94.3%–100% | 71.4%–83.3% | 74.3%–85.7% | 73.8%–84.5% | 94.3%–100% | 74.3%–85.7% |
| Loose | 17 | | | | | | | |
| 1 inner groove | 17 | | | | | | | |
| 1 inner groove and 3 holes | 17 | | | | | | | |
| 2 inner grooves | 17 | | | | | | | |
| 2 inner groove and 6 holes | 17 | | | | | | | |
| 1 external trench | 17 | | | | | | | |

A total of 119 trials of unlabeled data associated with various installation scenarios were investigated thoroughly. Within autoencoder, the stacked encoder reduced the data size to 10 features. Table 2 shows the classification result by either manually associating unlabeled clusters or deploying a softmax layer at output.

Most of error stemmed from either underfitting (the program fails to distinguish between two defects) or overfitting (the program splits a defect into both of two classes). They were the intrinsic problems of unsupervised learning which were hard to be corrected without feedback from the actual labels. The softmax layer at output stage abate overfitting and underfitting errors resulting a better accuracy. Autoencoder with softmax provided over 94% superb accuracy comparing with mediocre performance of SOM. It is a rather satisfactory result to distinguish seven scenarios as various pipeline corrosion types.

### 5.3 Analytics of Pattern Recognition

The effectiveness of machine learning on analysis of acoustic signal has been validated in the previous section. The subtle difference within internal corrosion of 90-degree iron elbow could be successfully recognized through machine learning algorithm. In the previous intrusion prewarning, four extrinsic acoustic events with distinct spectral features were tested to mimic the intentional sabotage to pipe surface. It is ponderable to broaden the investigation into security problem with more nuanced features and exam the performance of various machine learning tools.

Many distributed or multi-points fiber sensors were explored for intrusion detection in the last two decades, such as FBG array [133] [134], Michelson interferometer [135], Mach-Zehnder interferometer [136], Sagnac interferometer [137], Rayleigh OTDR [138], φ-OTDR [139], and

Brillouin OTDR [140]. But the proposed event recognitions have only been able to distinguish events with significantly different acoustic patterns such as classifying human walking and motor vehicle movement [63].

With Rayleigh enhancement, the over 35 dB SNR improvement of φ-OTDR should induce more sensitive dynamic strain detection. It was evaluated to recognize the subtle locomotion difference between individuals. Multiple machine learnings were discussed to promptly handle complicated dataset and extract the salient features, which include both supervised and unsupervised algorithms. It has great importance to manifest the potential of machine learning on identification of nuanced features.

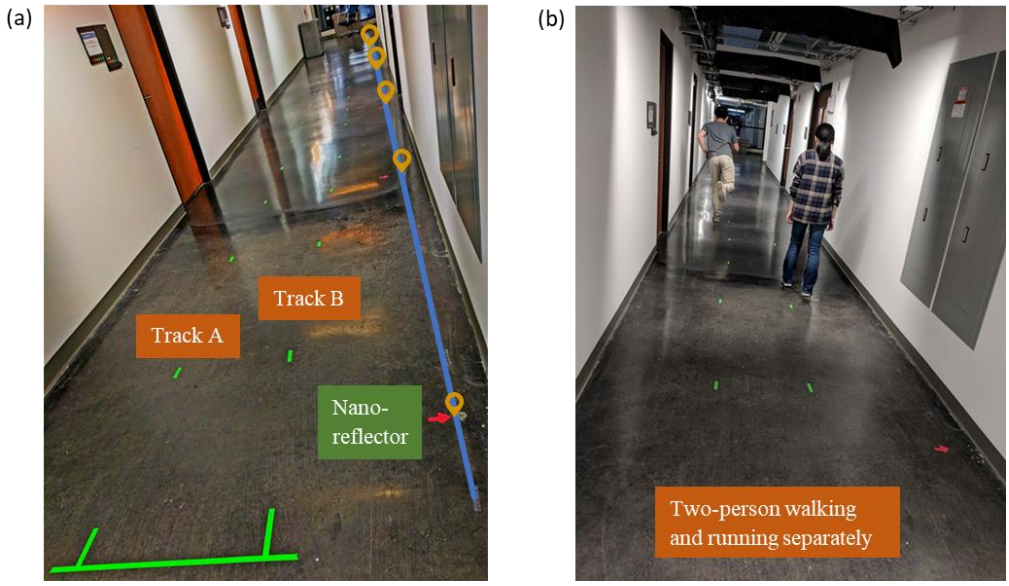


**Figure 41 Identification of human locomotion by using Rayleigh enhanced φ-OTDR. (a) 15-meter hallway marked for two tracks and sensing fiber. (b) An acoustic event of one person running and another walking.**

By using exactly same interrogation system as Rayleigh enhanced φ-OTDR, the experiments were carried out in a 15-meter long hallway as shown in Figure 41. Sensing optical fiber inscribed with nano-reflectors were tapped to lay straight on the concrete floor. In total 6

nano-reflectors were written within standard telecom fiber at 3-meter interval, which brings about 5 active sensors along entire fiber.

Two tracks were marked in green with 80 cm and 140 cm distance to sensing fiber. Five sensing regions across optical fiber monitored the footsteps of participants moving at either tracks simultaneously. In total 8 people joined the experiment to form different groups of movements. Each person repeated a given event (e.g. running, walking) on both tracks 26 times. Some additional variation such as alternative shoes and pushing cart were recorded as well. Table 3 concluded the detailed dataset of human locomotion detection. Eight events brought about 1196 set of trials for further analysis.

**Table 3 Description of dataset from human movements.**

| Event | Participant | Track | Repetition | Samples |
|---|---|---|---|---|
| One-person walk | 8 | 2 | 26 | 416 |
| One-person walk with different shoe | 1 | 1 | 26 | 26 |
| One-person walk with cart | 1 | 1 | 26 | 26 |
| One-person run | 8 | 2 | 26 | 416 |
| One-person run with different shoe | 1 | 1 | 26 | 26 |
| Two-person walk | 4 | 1 | 26 | 104 |
| Two-person run | 3 | 1 | 26 | 78 |
| One-person walk and one-person run | 4 | 1 | 26 | 104 |
| Total Samples | 1196 | | | |

The acoustic signals from each sensor were recorded into 1-second segment for ten sequential frames. There was idle time existing between adjacent frames on the account of limited operational capability in the computer-based data acquisition and processing. In order to abate the computational burden of signal processing, the spectral acoustic data were filtered to leave the low-frequency components supported by previous studies [141], that vibration signatures below 500 Hz were sufficient to recognize walking styles in terms of energy and variability. All data

were analyzed in frequency-domains in order to offer machine learnings direct access to the global properties of the signals.

In the spectral analysis, the low-pass filtering was equivalent to retain the amplitudes of first 32 frequency components. A sinc filter was used to highlight the latent spectral features and facilitate the algorithms by smoothly interpolating 32 amplitudes to 256 points. Figure 42 shows the filtered data after pre-processing. It included overlay curve plots of both time-domain and frequency-domain, and stacked intensity maps for visualization as well.

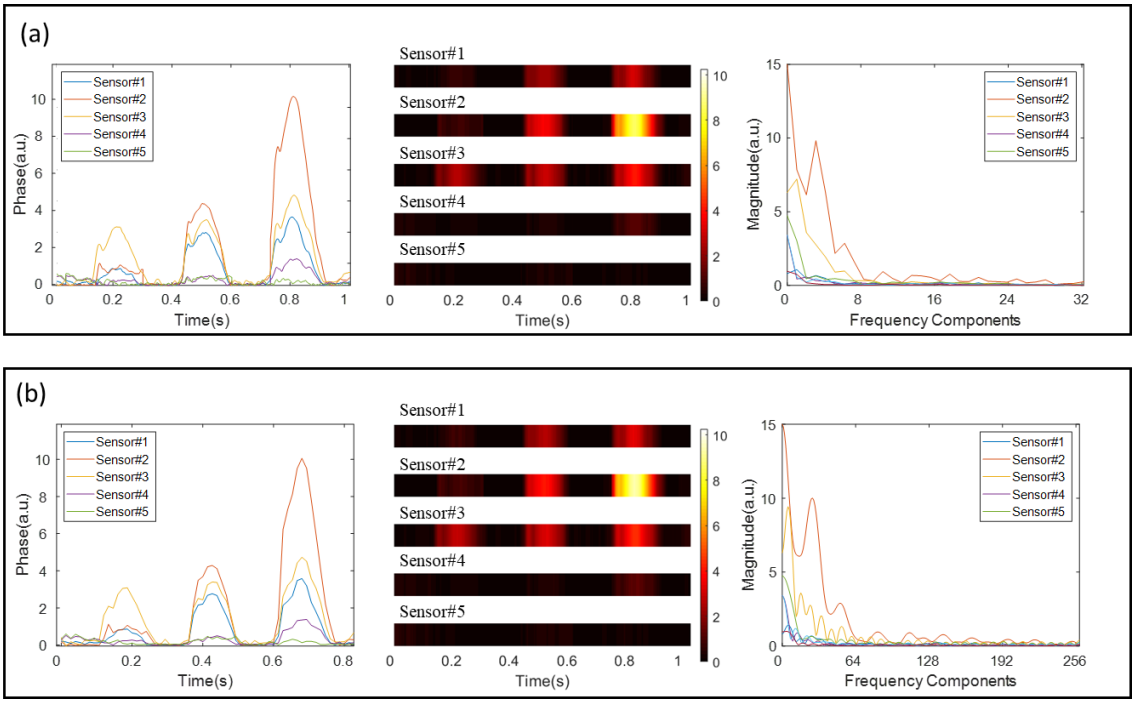


**Figure 42 Plots of acoustic signals in the event of one-person running including (a) unfiltered and (b) filtered dataset: overlaid raw data, intensity map for visualization, and spectral components (from left to right).**

The time-domain plot showed three footsteps subjecting to running motion of a single person. It was obvious to deduce the occurrence of running was between the 0 and 9-meter section of the hallway from the location of the first nano-reflector, which was exactly consistent with the

actual event. The data pre-processing using sinc and low-pass filter was evidenced to keep the predominant features of signals, which was qualified to be used in event identification.

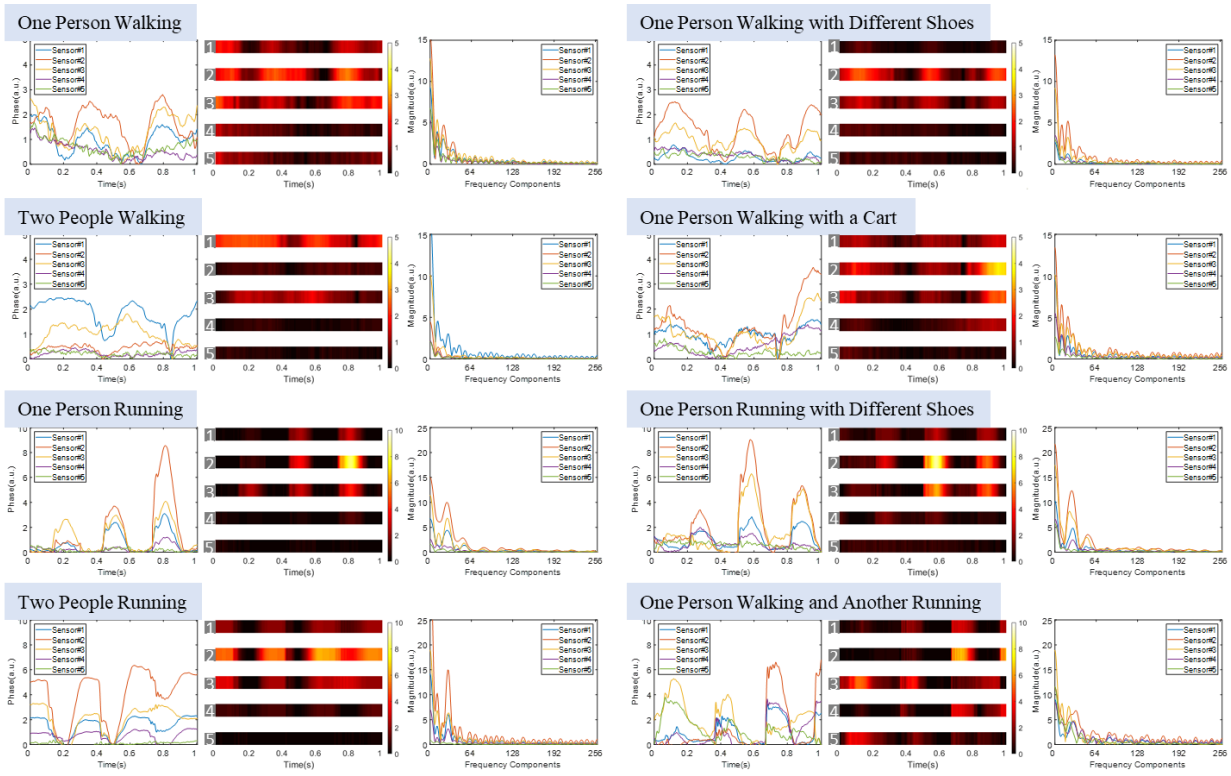


**Figure 43 Eight acoustic events participated by eight people in overlaid curve plots of time-domain and frequency-domain, and intensity maps for visualization.**

Temporal acoustic signals from five cascaded sensors revealed direction of movements and imbalance in a person's stride as well. Integrating all the variants as latent features within acoustic signals could be used to investigate the effectiveness of machine learning algorithms. Normally, the identification through data analysis using the qualitative "eye-ball" approach in the time domain, or quantitative analysis in the frequency domain, become extremely difficult if a large number of participants or a wide range of events are involved. Machine learnings offered an accessible method to simplify the feature extraction and output reliable classification. The detailed

temporal and spectral acoustic signals were shown in Figure 43. They included walking or running with different footwear, walking while pushing a cart, and locomotion involving multiple participants.

The nuanced features between different events was hid withing enormous volume of data. The frequency/rhythm of human locomotion, imbalances in a person's stride, and the temporal characteristics of foot impact were hard to be delineated by predictive data analysis. Machine learnings could potentially handle them and assess the right features relative to characteristics of participants.

Considering the similar temporal acoustic signals from each event, the nonlinearity within dataset should be a great importance on pattern recognition. CNN implemented multiple layers of convolution filters to exact the feature and map them onto various categories of classification. Due to the help of non-linear activation and pooling processes, the covert traits of acoustic events could be found and interpreted at the end of a fully connected layer. The acoustic signals from ten time-frames and five sensors were compiled into three-dimensional data structures in order to accommodate CNN. By transforming into a three-dimensional tensor within the frequency domain, the global properties of various intrusions can be efficiently accessed. Figure 44 shows the architecture of CNN used to explore the nonlinear feature of eight acoustic events.

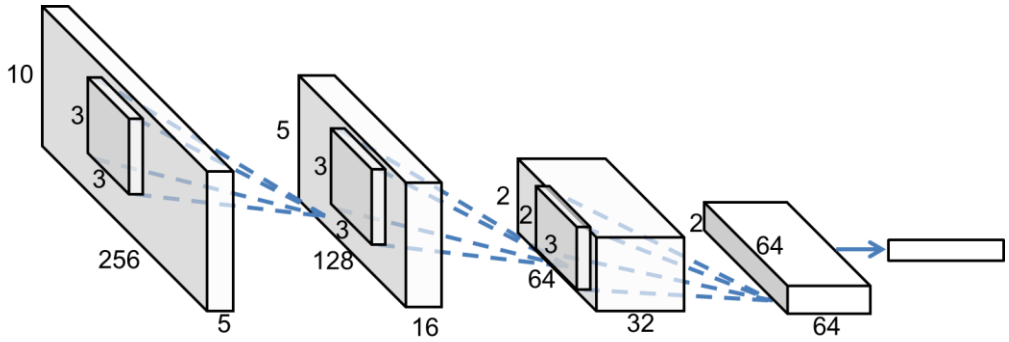


**Figure 44 Architecture of the CNN for identification of human locomotion.**

**Table 4 Classification results using CNN for different scenarios.**

| Training | Testing | Recognition | Accuracy |
|---|---|---|---|
| One-person Walking | One-person walking | Person | 78.75%-86.25% |
| | One-person walking with different tracks | Track | 85.00%-100.00% |
| | One-person walking with different shoes | Shoes | 80.00%-100.00% |
| | One-person walking and pushing cart | Cart | 93.75%-100.00% |
| One-person Running | One-person running | Person | 76.25%-86.25% |
| | One-person running with different tracks | Track | 95.00%-100.00% |
| | One-person running with different shoes | Shoes | 75.00%-90.00% |
| One-person Walking | Two-person both walking | Person | 63.85%-78.46% (Either)<br>28.46%-44.62% (Both) |
| One-person Running | Two-person both running | Person | 60.26%-76.92% (Either)<br>34.62%-50.00% (Both) |
| One-person Walking + One-person Running | Two-person walking and running separately | Person & Movement | 54.62%-69.23% (Either)<br>46.92%-61.54% (Both) |

At the input stage, the acoustic signals from five sensor and ten time-frames were constructed to be a matrix of 256 (frequency dimension) × 10 (seconds) × 5 (sensors). Three layers of convolutional filters were applied in the CNN structure. Rectified Linear Unit and max-pooling were used between each layer to reduce the data size in each channel. However, the growth of channel number implied more features were arranged and extracted. At output stage, a fully connected softmax predicted the probability of fitting into different categories based on existing features. Overall, 2/3 of data were used for training, while the remaining data was used for testing. Table 4 shows the Performance of CNN on gauging various acoustic data generated by eight different events. By separately arrange the training and testing data, recognizing individual, tracks or shoes were performed in a like manner. With much confidence on CNN, identifying both individual and movement at same time was advanced to explore its limit.

Over 76.25% accuracy has been achieved to identify the person presenting in individual movement while over 80% on cart, tracks and shoes classification. Walking and running showed minor difference from identification results. The accuracy decreased a lot to recognize the person or movement presenting in grouped events. A plausible cause of the failure is that the signal of one subject may be overwhelmed by the other. An advanced mathematical model needs to be developed to address this problem.

Due to the great diversity of machine learning algorithm, it is hard to claim a conclusive method specifying to handle pattern recognition of acoustic signals. Another attempt has been made to reveal the potential of machine learning on event recognition in time-domain. Beside CNN, long short-term memory (LSTM) is a popular architecture of Recurrent Neural Network especially being adept at dynamical systems and real-time temporal signal processing. Speech recognition and intrusion detection supported its effectiveness with convinced result.

By letting the output serve as its own input, the recurrent layer generates a feedback loop as memory units to track intrinsic dependencies during dataflow. The memory units are controlled at the location of being received (input gate), retained (forget gate), or used in the output (output gate). Nonlinear functions regulated the gates and controlled the dataflow.

The comparison between CNN and LSTM was shown in Table 5 by identifying the person within one-person walking events. Low accuracy of LSTM reveals its weakness in segmented signal recognition. It was inevitable to face the idle time between adjacent time-frames in the consequence of limited computational capability. The inferior result proved the unsuccessful attempt on ignoring the gap between time-frames to from the continuous temporal inputs of LSTM.

Back to spectral analysis, three more methods were discussed to investigate their effectiveness, Error-Correcting Output Codes (ECOC), K-Nearest Neighbor (KNN), and Naïve

Bayes (NB) classifiers. They are well-developed owning strong outcomes in a variety of applications.

ECOC works as a multiclass extension of the Support Vector Machine (SVM) algorithm that trains multiple SVM binary classifiers for each bit of the coded classes. Distance-dependent KNN classifies the input data based on a plurality of its *K* nearest neighbors from the training set belong. NB classifier learns the probability model from training data to categorize multiple classes corresponding to the maximum a posteriori estimate of the model parameters. The comparison between those methods shows the spectral analysis of machine learnings based on the models of SVM, distance and probability. The result shown in Table 5 provided a direction for improving the accuracy of event recognition with machine learning. The CNN clearly outperforms all other methods, with LSTM being the most inefficient.

**Table 5 Classification results using different machine learning algorithms or neural networks.**

| Method | Accuracy |
|---|---|
| CNN | 78.75%-86.25% |
| LSTM | 12.50%-20.62% |
| ECOC | 63.44%-76.92% |
| KNN | 44.69%-62.50% |
| NB | 42.50%-64.42% |

On the contrary to supervised learning, adaptively partitioning the data into different clusters based on certain criteria is attractive without tedious work of labeling. K-means clustering with Euclidean distance is a basic clustering method commonly used for feature extraction. By minimizing the sum of total variances within the clusters, it is viable to distinguish the latent features. Although the exact solution of K-means clustering is NP-hard (non-deterministic

polynomial-time), Lloyd's algorithm provides an effective method of relaxation by iteratively updating the centroids of the clusters. Let $(x_i)_{1\leq i\leq N}$ be the datapoints and denote the centroids of cluster $k$ at iteration $j$ by $c_{kj}$. Lloyd's algorithm includes two steps in each iteration, classifying each datapoint $x_i$ into the cluster whose centroid is closest to $x_i$ (i.e., $\arg\min_k \|x_i - c_{kj}\|$), and calculating the centroids for the next iteration based on the current clustering.

$$c_{k(j+1)} = \frac{1}{|C_{kj}|} \sum_{i \in C_{kj}} x_i, \tag{5-3}$$

where $C_{kj}$ is set of the indices of all datapoints in cluster $k$ at iteration $j$. Lloyd's algorithm is reluctant to guarantee the optimality of the solution while showing a fast convergency. However, it provides intuitive illustration on evaluation of well-behaved datasets. The classification results rank the cluster from distinct features to nuanced features.

The unlabeled output of K-means algorithm was hard to be interpreted. By using a hierarchical two-class clustering, potential features were compared with output at each step. The accuracy shown in Table 6 is not an objective evaluation of the unsupervised learning method, but simply an indication of the type of features the algorithm prioritizes and finds.

Unsupervised learning is inapplicable to find the range of uncertainty due to absence of training and validation groups. The accuracy was described as rate to form the top cluster. Feeding the data individually was opposite to feeding them together. This can be explained by the fact that more subjects in the input data equal more secondary features in the dataset—a potential source of confusion for the algorithm.

Unsupervised learning can characterize the acoustic signals based on priority of prominent features. Some covert but important features may be lost during classification. Precise and

successful identification must result from sifting through a multitude of possibilities and determining a specific combination of features, such as the strength, duration, and location of steps, as well as the speed and rhythm of movement. Characterizing the acoustic wave based on onefold criteria severely limited its performance on event identification. However, it is still a valuable tool to reveal apparent features within the dataset.

**Table 6 Tendency of classification in K-means clustering for various training dataset.**

| Training | Top Clusters | Accuracy |
|---|---|---|
| One-person Running | Direction1<br>Direction2 | 53.85% (All)<br>92.31% (Individual) |
| Unidirectional One-person Running | Person | 77.65% (All)<br>100% (Individual) |
| One-person Walking | Direction1<br>Direction2 | 65.38% (All)<br>96.15% (Individual) |
| Unidirectional One-person Walking | Person | 88.46% (All)<br>94.23% (Individual) |
| One-person Walking + One-person Running | Movement1 (running)<br>Movement2 (walking) | 94.71% |

# 6.0 Conclusion and Further Improvement

Distributed ultrasound sensing has a great appeal to many applications for prominently detailed information in characterizing the propagation path of acoustic wave or specifying its initial releasing status. Electronic-based sensors were standard technologies for ultrasonic detection but subjected to complex and cumbersome for large scale deployments. Optical fiber provided a promising alternative with merits of multiplex scalability and adequate sensitivity.

## 6.1 Conclusion

In the high-speed distributed strain measurement within optical fiber, conventional methods were limited by slow response of spectrometer in spectral interferometry and low intrinsic Rayleigh scattering in temporal reflectometry. The nano-reflectors inscribed by ultrafast laser direct-writing provided possible solutions to break the bottleneck. With over 35 dB enhancement of Rayleigh backscattering and 0.0012 dB insertion loss, nano-reflectors were able to construct effective inline FP cavities along entire fiber. Long-length IFPIs incorporating with reassigned STFT and OPLL achieved multi-points ultrasound detection on 20 kHz PZT vibration as low as 2.4 με. Homodyne Rayleigh-enhanced φ-OTDR was setting to 66 kHz sampling rate to receive the acoustic wave propagating along iron pipes generated by specific hammer. Four types of external intrusion events and seven installation sceneries were delicately designed to investigate the performance of Rayleigh-enhanced φ-OTDR. Based on high-quality acoustic signals of dynamic strain measurement, machine learnings were used to promptly handle the large volume of dataset

and make a reliable classification. Both supervised and unsupervised algorithms were explored to exam their effectiveness in PR and find the cluster of latent features. And they have been extended to distinguish the nuanced features within human locomotion that provided intuitive depiction on their capability. CNN has been proved to be impressive and effective in all cases with input of three-dimensional spectral data matrix. On the contrary, unsupervised learnings were reluctant to grasp a useful combination of features to make a valid classification. It was fit for revealing the interrelation among latent features within the dataset.

## 6.2 Further Improvement

Ultrasound detection always craves for wide detectable frequency range and high SNR. Although fiber-based distributed strain sensors have proved their robustness on high-frequency dynamic strain measurement, undoubted drawbacks urge more endeavors should be paid for improvement.

Ultrafast laser direct-writing owns incomparable merits on fabrication of nano-reflectors. The wavelength-independent Rayleigh enhancement is right for constructing FP cavity. And roll-to-roll setup promise its prospect in mass production. The further improvement should focus on extensively making nano-reflectors with same reflectance. Keeping the same reflectance is the premise to achieve high visibility of FPI.

Based on nano-reflectors within inline IFPIs, the long-length FP cavity speeds up the sampling rate of spectral interferometry. A noise-free dynamic strain measurement was achieved by using OPLL to linearize the frequency output and using reassigned STFT to demodulate ultrasound through tracking the energy center. However, the current experimental setup was far

from optimal from a couple of unconsidered aspects. Reassigned STFT still suffered from Heisenberg uncertainty principle and was hard to fine-tune the window size for better resolution. Reassigned smoothed pseudo WVD found the balance point within uncertainty principle should be investigated for its potential on prompt time-frequency decomposition. FPGA was also reported to support various TFRs including WVD. Besides, commercial LIA and LD driver composed OPLL leading to limited capability on phase-locking. An analog feedback circuit consisting of function generator, automatic gain control, double balanced mixer and low pass filter can alternate to better the performance. It might need a customized design of integrated circuits.

The long-distance interrogation of dynamic strain by using φ-OTDR was curbed by polarization fading, low SNR and accurate phase demodulation. These improvement has been discussed and undergone substantial development over the past few decades. Polarization fading can be fixed by the use of PM fiber, polarization diversity detection or measuring impulse response with polarization switch. Low intrinsic SNR has the solution of Rayleigh enhancement, cascaded modulators, hybrid gain from Raman and EDFA, and pulsed coding as Golay or Simplex. For accurate phase demodulation, homodyne and heterodyne interferometry were the basis owning different strategy for noise reduction. Like in NPS method, commercially 3×3 optical fiber coupler is usually asymmetric. The phase difference between three output ports have to be calibrated before applying the demodulation algorithm. And the compensation of phase offset introducing additional processing like ellipse fitting definitely increases the complexity of system.

To achieve a perfect distributed ultrasound system is painstaking which need dedicated design on sensors fabrication, interrogation strategy and hardware of fast processing. For now, the cost-effective solution is impractical due to the intrinsic limit of light manipulation in optical fiber.

But considering the extraordinary scalability of optical fiber, it is still valuable in the market of large-scale monitoring.

## Bibliography


1. Feynman, R.P., *The Feynman lectures on physics*. 1963: Reading, Mass. : Addison-Wesley Pub. Co., c1963-1965.

2. White, R.M. *Acoustic sensors for physical, chemical and biochemical applications*. in *Proceedings of the 1998 IEEE International Frequency Control Symposium (Cat. No. 98CH36165)*. 1998. IEEE.

3. McDicken, W. and T. Anderson, *Basic physics of medical ultrasound.* Blood, 2011. **1570**(1.61): p. 105.

4. Mujahid, A., A. Afzal, and F.L. Dickert, *An Overview of High Frequency Acoustic Sensors—QCMs, SAWs and FBARs—Chemical and Biochemical Applications.* Sensors, 2019. **19**(20): p. 4395.

5. Thijssen, J.M. and M. Mischi, *2.13 - Ultrasound Imaging Arrays*, in *Comprehensive Biomedical Physics*, A. Brahme, Editor. 2014, Elsevier: Oxford. p. 323-341.

6. Szabo, T.L., *Chapter 5 - Transducers*, in *Diagnostic Ultrasound Imaging: Inside Out (Second Edition)*, T.L. Szabo, Editor. 2014, Academic Press: Boston. p. 121-165.

7. Hunt, J.W., M. Arditi, and F.S. Foster, *Ultrasound transducers for pulse-echo medical imaging.* IEEE Transactions on Biomedical Engineering, 1983(8): p. 453-481.

8. Shung, K.K., J. Cannata, and Q. Zhou, *Piezoelectric materials for high frequency medical imaging applications: A review.* Journal of Electroceramics, 2007. **19**(1): p. 141-147.

9. Bernstein, J.J., et al., *Micromachined high frequency ferroelectric sonar transducers.* IEEE transactions on ultrasonics, ferroelectrics, frequency control, 1997. **44**(5): p. 960-969.

10. Bhuyan, A., et al., *Integrated circuits for volumetric ultrasound imaging with 2-D CMUT arrays.* IEEE transactions on biomedical circuits systems, 2013. **7**(6): p. 796-804.

11. Helin, P., et al. *Poly-SiGe-based CMUT array with high acoustical pressure*. in *2012 IEEE 25th International Conference on Micro Electro Mechanical Systems (MEMS)*. 2012. IEEE.

12. Khuri-Yakub, B.T. and Ö. Oralkan, *Capacitive micromachined ultrasonic transducers for medical imaging and therapy.* Journal of micromechanics microengineering, 2011. **21**(5): p. 054004.

13. Roberts, M.J., *Design and fabrication of a flexible membrane ultrasound transducer*. 2018, Massachusetts Institute of Technology.

14. Donnelly, N.J. and C.A. Randall, *Refined model of electromigration of Ag/Pd electrodes in multilayer PZT ceramics under extreme humidity.* Journal of the American Ceramic Society, 2009. **92**(2): p. 405-410.

15. Bayram, B., et al., *Finite element modeling and experimental characterization of crosstalk in 1-D CMUT arrays.* IEEE transactions on ultrasonics, ferroelectrics, frequency control, 2007. **54**(2): p. 418-430.

16. Hecht, J., *City of light : the story of fiber optics*. The Sloan technology series. 1999, New York: Oxford University Press. xii, 316 p.

17. Culshaw, B. and A. Kersey, *Fiber-optic sensing: A historical perspective.* Journal of Lightwave Technology, 2008. **26**(9-12): p. 1064-1078.

18. Udd, E., *Fiber optic smart structures.* Proceedings of the Ieee, 1996. **84**(6): p. 884-894.

19. Tracey, P.M., *Intrinsic fiber-optic sensors.* IEEE Transactions on Industry Applications, 1991. **27**(1): p. 96-98.

20. Yu, F. and Y. Shizhuo, *Fiber Optic Sensors, Marcel Decker.* Inc., Newyork, 2002.

21. El-Sherif, M., *Smart structures and intelligent systems for health monitoring and diagnostics.* Applied Bionics Biomechanics. 2005. **2**(3-4): p. 161-170.

22. Inaudi, D. and B. Glisic. *Overview of fibre optic sensing applications to structural health monitoring*. in *Symposium on Deformation Measurement and Analysis*. 2008.

23. Méndez, A. and A. Csipkes. *Overview of Fiber Optic Sensors for NDT Applications*. 2013. Dordrecht: Springer Netherlands.

24. Wissmeyer, G., et al., *Looking at sound: optoacoustics with all-optical ultrasound detection.* Light: Science Applications. 2018. **7**(1): p. 1-16.

25. Nelson, D., D. Kleinman, and K. Wecht, *Vibration-induced modulation of fiberguide transmission.* Applied Physics Letters, 1977. **30**(2): p. 94-96.

26. Chen, R., et al., *Linear location of acoustic emission using a pair of novel fibre optic sensors.* Measurement Science Technology, 2006. **17**(8): p. 2313.

27. Rines, G.A., *Fiber-optic accelerometer with hydrophone applications.* Applied optics, 1981. **20**(19): p. 3453-3459.

28. Bucaro, J.A., H.D. Dardy, and E.F. Carome, *Optical fiber acoustic sensor.* Applied optics, 1977. **16**(7): p. 1761-1762.

29. Imai, M., T. Ohashi, and Y. Ohtsuka, *Fiber-optic Michelson interferometer using an optical power divider.* Optics letters, 1980. **5**(10): p. 418-420.

30. Udd, E. *Fiber-optic acoustic sensor based on the Sagnac interferometer*. in *Single Mode Optical Fibers*. 1983. International Society for Optics and Photonics.

31. Murphy, K.A., et al., *Quadrature phase-shifted, extrinsic Fabry–Perot optical fiber sensors.* Optics letters, 1991. **16**(4): p. 273-275.

32. Webb, D.J., et al. *Miniature fiber optic ultrasonic probe*. in *Fiber Optic and Laser Sensors XIV*. 1996. International Society for Optics and Photonics.

33. Bauer-Marschallinger, J., et al. *Low-cost parallelization of optical fiber based detectors for photoacoustic imaging*. in *Photons Plus Ultrasound: Imaging and Sensing 2013*. 2013. International Society for Optics and Photonics.

34. Fujisue, T., K. Nakamura, and S. Ueha, *Demodulation of acoustic signals in fiber Bragg grating ultrasonic sensors using arrayed waveguide gratings.* Japanese journal of applied physics, 2006. **45**(5S): p. 4577.

35. Takahashi, N., K. Tetsumura, and S. Takahashi. *Multipoint detection of an acoustic wave in water with a WDM fiber-Bragg-grating sensor*. in *Optical Engineering for Sensing and Nanotechnology (ICOSN'99)*. 1999. International Society for Optics and Photonics.

36. Li, Y., et al., *An all-fiber multi-channel ultrasonic sensor using a switchable fiber Bragg gratings filter in erbium-doped fiber laser.* Journal of Lightwave Technology, 2019. **37**(17): p. 4330-4339.

37. Chow, J.H., et al., *Demonstration of a passive subpicostrain fiber strain sensor.* 2005. **30**(15): p. 1923-1925.

38. Liu, Q., et al., *Quadrature phase-stabilized three-wavelength interrogation of a fiber-optic Fabry–Perot acoustic sensor.* 2019. **44**(22): p. 5402-5405.

39. Photonics, E. *Relative Intensity Noise of Distributed Feedback Lasers*. Application note.

40. Wada, A., S. Tanaka, and N. Takahashi, *Multi-point strain measurement using Fabry–Perot interferometer consisting of low-reflective fiber Bragg grating.* Japanese Journal of Applied Physics, 2017. **56**(11): p. 112502.

41. Wang, M., et al. *Ultrafast Laser Enhanced Rayleigh Backscattering on Silica Fiber for Distributed Sensing under Harsh Environment*. in *CLEO: Applications and Technology*. 2018. Optical Society of America.

42. Zou, W., X. Long, and J. Chen, *Brillouin scattering in optical fibers and its application to distributed sensors.* Advances in Optical Fiber Technology: Fundamental Optical Phenomena Applications, 2015: p. 1.

43. Bergman, A., et al., *Dynamic and distributed slope-assisted fiber strain sensing based on optical time-domain analysis of Brillouin dynamic gratings.* Journal of Lightwave Technology, 2015. **33**(12): p. 2611-2616.

44. Barnoski, M. and S. Jensen, *Fiber waveguides: a novel technique for investigating attenuation characteristics.* Applied Optics, 1976. **15**(9): p. 2112-2115.

45. Gifford, D., et al. *Millimeter resolution otpical reflectometry over up to two kilometers of fiber length*. in *2007 IEEE Avionics, Fiber-Optics and Photonics Technology Conference*. 2007. IEEE.

46. Bao, X., et al., *Recent development in the distributed fiber optic acoustic and ultrasonic detection.* 2016. **35**(16): p. 3256-3267.

47. Bao, X. and L. Chen, *Recent progress in distributed fiber optic sensors.* sensors, 2012. **12**(7): p. 8601-8639.

48. Taylor, H.F. and C.E. Lee, *Apparatus and method for fiber optic intrusion sensing*. 1993, Google Patents.

49. Baker, C., et al., *Enhancement of optical pulse extinction-ratio using the nonlinear Kerr effect for phase-OTDR.* Optics Express, 2016. **24**(17): p. 19424-19434.

50. Jin, J., et al., *Distributed Temperature Sensing Based on Rayleigh Scattering in Irradiated Optical Fiber.* IEEE Sensors Journal, 2016. **16**(24): p. 8928-8935.

51. Loranger, S., et al., *Rayleigh scatter based order of magnitude increase in distributed temperature and strain sensing by simple UV exposure of optical fibre.* Scientific reports, 2015. **5**: p. 11177.

52. Wang, C., et al., *Distributed OTDR-interferometric sensing network with identical ultra-weak fiber Bragg gratings.* Optics express, 2015. **23**(22): p. 29038-29046.

53. Zhu, F., et al., *Improved Φ-OTDR sensing system for high-precision dynamic strain measurement based on ultra-weak fiber Bragg grating array.* Journal of Lightwave Technology, 2015. **33**(23): p. 4775-4780.

54. Morey, W.W., G. Meltz, and J.M. Weiss. *High-temperature capabilities and limitations of fiber grating sensors*. in *Tenth International Conference on Optical Fibre Sensors*. 1994. International Society for Optics and Photonics.

55. Qin, Z., L. Chen, and X. Bao, *Wavelet denoising method for improving detection performance of distributed vibration sensor.* IEEE Photonics Technology Letters, 2012. **24**(7): p. 542-544.

56. Lu, Y., et al., *Distributed vibration sensor based on coherent detection of phase-OTDR.* Journal of lightwave Technology, 2010. **28**(22): p. 3243-3249.

57. Zhu, T., et al., *Enhancement of SNR and Spatial Resolution in$\varphi$-OTDR System by Using Two-Dimensional Edge Detection Method.* Journal of Lightwave Technology, 2013. **31**(17): p. 2851-2856.

58. He, H., et al., *SNR Enhancement in Phase-Sensitive OTDR with Adaptive 2-D Bilateral Filtering Algorithm.* IEEE Photonics Journal, 2017. **9**(3): p. 1-10.

59. Wu, H., et al. *Multi-scale wavelet decomposition and its application in distributed optical fiber fences*. in *Fifth Asia-Pacific Optical Sensors Conference*. 2015. International Society for Optics and Photonics.

60. Tejedor, J., et al., *A novel fiber optic based surveillance system for prevention of pipeline integrity threats.* Sensors, 2017. **17**(2): p. 355.

61. Tejedor, J., et al., *Real field deployment of a smart fiber-optic surveillance system for pipeline integrity threat detection: Architectural issues and blind field test results.* Journal of Lightwave Technology, 2018. **36**(4): p. 1052-1062.

62. Sun, Q., et al., *Recognition of a phase-sensitivity OTDR sensing system based on morphologic feature extraction.* Sensors, 2015. **15**(7): p. 15179-15197.

63. Madsen, C., T. Bae, and R. Atkins. *Long fiber-optic perimeter sensor: Signature analysis*. in *Photonic Applications Systems Technologies Conference*. 2007. Optical Society of America.

64. Bahoura, M. and H. Ezzaidi. *FPGA implementation of a feature extraction technique based on Fourier transform*. in *2012 24th International Conference on Microelectronics (ICM)*. 2012. IEEE.

65. Namihira, Y.J.J.o.l.t., *Opto-elastic constant in single mode optical fibers.* 1985. **3**(5): p. 1078-1083.

66. Yuan, L., L.-m. Zhou, and W. Jin, *Detection of acoustic emission in structure using Sagnac-like fiber-loop interferometer.* Sensors Actuators A: Physical, 2005. **118**(1): p. 6-13.

67. Sandlin, S. and A. Hokkanen, *Embedding optical fibers in metal alloys.* IEEE instrumentation measurement magazine, 2003. **6**(2): p. 31-36.

68. Calero, J., et al., *Theory and experiments on birefringent optical fibers embedded in concrete structures.* Journal of Lightwave Technology, 1994. **12**(6): p. 1081-1091.

69. Lee, C., et al., *Metal-embedded fiber-optic Fabry–Perot sensors.* Optics letters, 1991. **16**(24): p. 1990-1992.

70. Rabus, D.G., *Integrated ring resonators*. 2007: Springer.

71. Wang, M., et al., *Multiplexable high-temperature stable and low-loss intrinsic Fabry-Perot in-fiber sensors through nanograting engineering.* Optics Express, 2020. **28**(14): p. 20225-20235.

72. Agrawal, G.P., *Nonlinear fiber optics*, in *Nonlinear Science at the Dawn of the 21st Century*. 2000, Springer. p. 195-211.

73. Debye, P., *Molecular-weight determination by light scattering.* The Journal of Physical Chemistry, 1947. **51**(1): p. 18-32.

74. Boyd, R.W., *Chapter 8 - Spontaneous Light Scattering and Acoustooptics*, in *Nonlinear Optics (Third Edition)*, R.W. Boyd, Editor. 2008, Academic Press: Burlington. p. 391-428.

75. Nakazawa, M., *Rayleigh backscattering theory for single-mode optical fibers.* JOSA, 1983. **73**(9): p. 1175-1180.

76. Seo, W., *Fiber optic intrusion sensor investigation.* 1995.

77. Chen, Z., et al., *Ultraweak intrinsic Fabry–Perot cavity array for distributed sensing.* Optics letters, 2015. **40**(3): p. 320-323.

78. Yan, A., et al., *Distributed Optical Fiber Sensors with Ultrafast Laser Enhanced Rayleigh Backscattering Profiles for Real-Time Monitoring of Solid Oxide Fuel Cell Operations.* Scientific reports, 2017. **7**(1): p. 9360.

79. Yan, A., et al. *Ultrafast Laser Enhanced Rayleigh Scattering Characteristics in D-Shaped Fibers for High-Temperature Distributed Chemical Sensing*. in *Photonics and Fiber Technology 2016 (ACOFT, BGPP, NP)*. 2016. Sydney: Optical Society of America.

80. Grobnic, D., C. Hnatovsky, and S.J. Mihailov, *Thermally stable type II FBGs written through polyimide coatings of silica-based optical fiber.* IEEE Photonics Technology Letters, 2017. **29**(21): p. 1780-1783.

81. Ma, J., et al., *Fiber-optic Fabry–Pérot acoustic sensor with multilayer graphene diaphragm.* 2013. **25**(10): p. 932-935.

82. Huang, J., et al., *Spatially continuous distributed fiber optic sensing using optical carrier based microwave interferometry.* Optics express, 2014. **22**(15): p. 18757-18769.

83. Wada, A., S. Tanaka, and N. Takahashi, *Partial scanning frequency division multiplexing for interrogation of low-reflective fiber Bragg grating-based sensor array*. Optical Review, 2018. **25**(5): p. 615-624.

84. Wada, A., S. Tanaka, and N. Takahashi, *Fast interrogation using sinusoidally current modulated laser diodes for fiber Fabry–Perot interferometric sensor consisting of fiber Bragg gratings.* Optical Review, 2018. **25**(5): p. 533-539.

85. Hymans, A., J.J.P.o.t.I.-P.B.e. Lait, and c. engineering, *Analysis of a frequency-modulated continuous-wave ranging system.* 1960. **107**(34): p. 365-372.

86. Lear, K., et al., *Selectively oxidised vertical cavity surface emitting lasers with 50% power conversion efficiency.* Electronics Letters, 1995. **31**(3): p. 208-209.

87. Froggatt, M., et al. *Distributed strain and temperature discrimination in unaltered polarization maintaining fiber*. in *Optical Fiber Sensors*. 2006. Optical Society of America.

88. Chinn, S., E. Swanson, and J. Fujimoto, *Optical coherence tomography using a frequency-tunable optical source.* Optics letters, 1997. **22**(5): p. 340-342.

89. Potsaid, B., et al. *MEMS tunable VCSEL light source for ultrahigh speed 60kHz-1MHz axial scan rate and long range centimeter class OCT imaging*. in *Optical Coherence Tomography and Coherence Domain Optical Methods in Biomedicine XVI*. 2012. International Society for Optics and Photonics.

90. Fukuda, M., et al., *Temperature and current coefficients of lasing wavelength in tunable diode laser spectroscopy.* Applied Physics B, 2010. **100**(2): p. 377-382.

91. Yamamoto, Y.J.I.J.o.Q.E., *AM and FM quantum noise in semiconductor lasers-Part I: Theoretical analysis.* 1983. **19**(1): p. 34-46.

92. Corrc, P., O. Girad, and I.J.I.j.o.q.e. De Faria, *On the thermal contribution to the FM response of DFB lasers: Theory and experiment.* 1994. **30**(11): p. 2485-2490.

93. Huang, K.-Y. and G.M. Carter, *Coherent optical frequency domain reflectometry (OFDR) using a fiber grating external cavity laser.* IEEE photonics technology letters, 1994. **6**(12): p. 1466-1468.

94. Tsuji, K., et al., *Spatial-resolution improvement in long-range coherent optical frequency domain reflectometry by frequency-sweep linearisation.* Electronics Letters, 1997. **33**(5): p. 408-410.

95. Soller, B.J., et al., *High resolution optical frequency domain reflectometry for characterization of components and assemblies.* Optics express, 2005. **13**(2): p. 666-674.

96. Iiyama, K., M. Yasuda, and S. Takamiya, *Extended-range high-resolution FMCW reflectometry by means of electronically frequency-multiplied sampling signal generated from auxiliary interferometer.* IEICE transactions on electronics, 2006. **89**(6): p. 823-829.

97. Fan, X., Y. Koshikiya, and F. Ito, *Phase-noise-compensated optical frequency domain reflectometry with measurement range beyond laser coherence length realized using concatenative reference method.* Optics letters, 2007. **32**(22): p. 3227-3229.

98. Yüksel, K., M. Wuilpart, and P. Mégret, *Analysis and suppression of nonlinear frequency modulation in an optical frequency-domain reflectometer.* Optics express, 2009. **17**(7): p. 5845-5851.

99. Vergnole, S., D. Lévesque, and G. Lamouche, *Experimental validation of an optimized signal processing method to handle non-linearity in swept-source optical coherence tomography.* Optics express, 2010. **18**(10): p. 10446-10461.

100. Ito, F., X. Fan, and Y. Koshikiya, *Long-range coherent OFDR with light source phase noise compensation.* Journal of Lightwave Technology, 2011. **30**(8): p. 1015-1024.

101. Iiyama, K., L.-T. Wang, and K.-I. Hayashi, *Linearizing optical frequency-sweep of a laser diode for FMCW reflectometry.* Journal of lightwave technology, 1996. **14**(2): p. 173-178.

102. Satyan, N., et al., *Precise control of broadband frequency chirps using optoelectronic feedback.* Optics express, 2009. **17**(18): p. 15991-15999.

103. Valle, C., et al., *Crack characterization using guided circumferential waves.* The Journal of the Acoustical Society of America, 2001. **110**(3): p. 1282-1290.

104. De Marchi, L., et al., *Ultrasonic guided-waves characterization with warped frequency transforms.* IEEE transactions on ultrasonics, ferroelectrics, frequency control, 2009. **56**(10): p. 2232-2240.

105. Niethammer, M., et al., *Time-frequency representations of Lamb waves.* The Journal of the Acoustical Society of America, 2001. **109**(5): p. 1841-1847.

106. Claasen, T. and W. Mecklenbrauker, *The Wigner distribution—A tool for time-frequency signal analysis.* Philips J. Res, 1980. **35**(3): p. 217-250.

107. Auger, F. and P. Flandrin, *Improving the readability of time-frequency and time-scale representations by the reassignment method.* IEEE Transactions on signal processing, 1995. **43**(5): p. 1068-1089.

108. Krawczyk, M. and T. Gerkmann, *STFT phase reconstruction in voiced speech for an improved single-channel speech enhancement.* IEEE/ACM Transactions on Audio, Speech, Language Processing, 2014. **22**(12): p. 1931-1940.

109. Niethammer, M., et al., *Time-frequency representation of Lamb waves using the reassigned spectrogram.* The Journal of the Acoustical Society of America, 2000. **107**(5): p. L19-L24.
110. Mallat, S., *A wavelet tour of signal p rocessing.* Daubechies Ten Lectures on Wavelets, 1998. **628**(1).

111. Derickson, D., *Fiber optic test and measurement*. Vol. 8.

112. Taylor, M.G., *Phase estimation methods for optical coherent detection using digital signal processing.* Journal of Lightwave Technology, 2009. **27**(7): p. 901-914.

113. Dandridge, A., A. Tveten, and T. Giallorenzi, *Homodyne demodulation scheme for fiber optic sensors using phase generated carrier.* IEEE Journal of Quantum Electronics, 1982. **18**(10): p. 1647-1653.

114. Fang, G., et al., *Phase-Sensitive Optical Time Domain Reflectometer Based on Phase-Generated Carrier Algorithm.* Journal of Lightwave Technology, 2015. **33**(13): p. 2811-2816.

115. Kersey, A., M. Marrone, and M. Davis, *Polarisation-insensitive fibre optic Michelson interferometer.* Electronics letters, 1991. **27**(6): p. 518-520.

116. Takushima, Y., H. Choi, and Y.C. Chung, *Measurement of differential phasor diagram of multilevel dpsk signals by using an adjustment-free delay interferometer composed of a 3$\,\times\, $3 optical coupler.* Journal of lightwave technology, 2009. **27**(6): p. 718-730.

117. Butler, T., et al., *Single shot, time-resolved measurement of the coherence properties of OCT swept source lasers.* Optics letters, 2015. **40**(10): p. 2277-2280.

118. Liping, S. and Y. Peida, *General analysis of [3× 3] optical-fiber directional couplers.* Microwave Optical Technology Letters, 1989. **2**(2): p. 52-54.

119. Fei, Y., et al., *120 Phase Difference Interference Technology Based on 3× 3 Coupler and its Application in Laser Noise Measurement.* Optical Interferometry, 2017: p. 233.

120. Zhao, Z., M.S. Demokan, and M. MacAlpine, *Improved demodulation scheme for fiber optic interferometers using an asymmetric 3/spl times/3 coupler.* Journal of lightwave technology, 1997. **15**(11): p. 2059-2068.

121. Koo, K., A. Tveten, and A. Dandridge, *Passive stabilization scheme for fiber interferometers using (3× 3) fiber directional couplers.* Applied Physics Letters, 1982. **41**(7): p. 616-618.

122. Brown, D.A. *A symmetric 3x3 coupler based demodulator for fiber optic interferometric sensors*. in *Fiber Optic and Laser Sensors IX*. 1991. International Society for Optics and Photonics.

123. Peng, F., et al. *128km fully-distributed high-sensitivity fiber-optic intrusion sensor with 15m spatial resolution*. in *Optical Fiber Communication Conference*. 2014. Optical Society of America.

124. Evans, M. and K. Vine. *Permanently installed transducers for guided wave monitoring of pipelines*. in *10th European conference on Non-destructive testing, Moscow, Russia*. 2010.

125. Lowe, M. and P. Cawley, *Long range guided wave inspection usage–current commercial capabilities and research directions.* Department of Mechanical Engineering, Imperial College, London, 2006.

126. Liu, C., J. Dobson, and P. Cawley, *Efficient generation of receiver operating characteristics for the evaluation of damage detection in practical structural health monitoring applications.* Proceedings of the Royal Society A: Mathematical, Physical Engineering Sciences. 2017. **473**(2199): p. 20160736.

127. Cawley, P. *Practical long range guided wave inspection—Managing complexity*. in *AIP Conference Proceedings*. 2003. AIP.

128. Spirin, V., et al., *Fiber Bragg grating sensor for petroleum hydrocarbon leak detection.* Optics Lasers in Engineering 1999. **32**(5): p. 497-503.

129. Buerck, J., et al., *OTDR fiber-optical chemical sensor system for detection and location of hydrocarbon leakage.* Journal of hazardous materials, 2003. **102**(1): p. 13-28.

130. Shi, Y., et al. *Research on wavelet analysis for pipeline pre-warning system based on phase-sensitive optical time domain reflectometry*. in *2014 IEEE/ASME International Conference on Advanced Intelligent Mechatronics*. 2014. IEEE.

131. Wu, H., et al. *A hydrostatic leak test for water pipeline by using distributed optical fiber vibration sensing system*. in *Fifth Asia-Pacific Optical Sensors Conference*. 2015. International Society for Optics and Photonics.

132. Iida, D., K. Toge, and T. Manabe. *High-frequency distributed acoustic sensing faster than repetition limit with frequency-multiplexed phase-OTDR.* in *2016 Optical Fiber Communications Conference and Exhibition (OFC)*. 2016. IEEE.

133. Wu, H., et al. *Real-time activity identification in a smart FBG-based fiber-optic perimeter intrusion detection system*. in *OFS2012 22nd International Conference on Optical Fiber Sensors*. 2012. International Society for Optics and Photonics.

134. Zhang, Y., et al. *Unattended ground sensor based on fiber Bragg grating technology*. in *Unattended Ground Sensor Technologies and Applications VII*. 2005. International Society for Optics and Photonics.

135. Park, J. and H.F. Taylor. *Fiber optic intrusion sensor*. in *Fiber Optic Sensors V*. 1996. International Society for Optics and Photonics.

136. Lan, T., et al. *Perimeter security system based on fiber optic disturbance sensor*. in *Advanced Sensor Systems and Applications III*. 2007. International Society for Optics and Photonics.

137. McAulay, A.D. and J. Wang. *A Sagnac interferometer sensor system for intrusion detection and localization*. in *Enabling Photonic Technologies for Aerospace Applications VI*. 2004. International Society for Optics and Photonics.

138. Blackmon, F. and J. Pollock. *Blue Rose perimeter defense and security system*. in *Sensors, and Command, Control, Communications, and Intelligence (C3I) Technologies for Homeland Security and Homeland Defense V*. 2006. International Society for Optics and Photonics.

139. Vdovenko, V. *Fiber optic intrusion sensing based on coherent optical time domain reflectometry*. in *International Conference on Lasers, Applications, and Technologies 2007: Environmental Monitoring and Ecological Applications; Optical Sensors in Biological, Chemical, and Engineering Technologies; and Femtosecond Laser Pulse Filamentation*. 2007. International Society for Optics and Photonics.

140. Klar, A. and R. Linker. *Feasibility study of the automated detection and localization of underground tunnel excavation using Brillouin optical time domain reflectometer*. in *Fiber Optic Sensors and Applications VI*. 2009. International Society for Optics and Photonics.

141. Ekimov, A. and J.M. Sabatier, *Vibration and sound signatures of human footsteps in buildings.* The Journal of the Acoustical Society of America, 2006. **118**(3): p. 2021-768.